University of New Mexico
UNM Digital Repository

Mechanical Engineering ETDs | Engineering ETDs

Fall 11-22-2019

Additively Manufactured Continuous Carbon Fiber Thermoplastic Composites for High-Performance Applications

Nekoda van de Werken

Follow this and additional works at: https://digitalrepository.unm.edu/me_etds

 Part of the Mechanical Engineering Commons, and the Structural Materials Commons

Recommended Citation

van de Werken, Nekoda. "Additively Manufactured Continuous Carbon Fiber Thermoplastic Composites for High-Performance Applications." (2019). https://digitalrepository.unm.edu/me_etds/178

This Dissertation is brought to you for free and open access by the Engineering ETDs at UNM Digital Repository. It has been accepted for inclusion in Mechanical Engineering ETDs by an authorized administrator of UNM Digital Repository. For more information, please contact amywinter@unm.edu, lsloane@salud.unm.edu, sarahrk@unm.edu.

Nekoda van de Werken

Candidate

Mechanical Engineering

Department

This dissertation is approved, and it is acceptable in quality and form for publication:

Approved by the Dissertation Committee:

Yu-Lin Shen, Ph.D., Chairperson

Mehran Tehrani, Ph.D.

Mahmoud R. Taha, Ph.D.

Andrew Williams, Ph.D.

ADDITIVELY MANUFACTURED CONTINUOUS CARBON FIBER THERMOPLASTIC COMPOSITES FOR HIGH-PERFORMANCE APPLICATIONS

by

NEKODA VAN DE WERKEN

M.S. MECHANICAL ENGINEERING,
UNIVERSITY OF NEW MEXICO
2017

B.S. MECHANICAL ENGINEERING,
UNIVERSITY OF NEW MEXICO
2014

DISSERTATION

Submitted in Partial Fulfillment of the
Requirements for the Degree of

Doctor of Philosophy in Engineering

The University of New Mexico
Albuquerque, New Mexico

December 2019

DEDICATIONS

This dissertation is dedicated to my mother, Stephanie Harrison, and brother, Kahlil van de Werken, whose continuous encouragement and support has made this dissertation possible.

ACKNOWLEDGEMENTS

I would like to acknowledge my graduate advisor, Dr. Mehran Tehrani, who has helped me navigate the challenges of experimental research throughout my educational career. Beginning as an undergraduate in his lab, Dr. Tehrani has offered patient guidance and invaluable lessons to help me grow and progress as a student, researcher, and person. I am grateful to have an ambitious and talented role model through this formative process.

This dissertation was also made possible through the contributions, both intellectual and in time and effort, of my fellow colleagues and university students. In particular, Pouria Khanbolouki has lent his time and expertise for a variety of characterization techniques and in producing exquisite figures, many of which are present within this document. Jafar Ghorbani and Pratik Koirala have generously assisted with the thermal, mechanical, and structural characterizations to the benefit of this study. Additionally, the assistance of Matthew Abel (NSF REU undergraduate student) in performing some of the necessary preliminary research on thermal treatments of printed PA6 composites, and Robert Flores (undergraduate research assistant) in designing and modelling the clamps used for DIC of optimized composites, is greatly appreciated.

I would like to acknowledge the support of the United States Air Force Research Laboratories and Air Force Office of Scientific Research for their interest, guidance, and support in this research. In particular, I would like to express my sincere gratitude to Dr. Andrew Williams and Dr. Derek Doyle for their invaluable assistance and contributions that made this research possible.

Lastly, I would like to express my sincere gratitude to Dr. Shen, Dr. Taha, and Dr. Williams for serving on my dissertation committee. Additionally, thank you to Dr. Shen for serving as my committee chair in place of Dr. Tehrani upon his transfer to UT Austin.

ADDITIVELY MANUFACTURED CONTINUOUS CARBON FIBER THERMOPLASTIC COMPOSITES FOR HIGH-PERFORMANCE APPLICATIONS

By:

Nekoda van de Werken

B.S. Mechanical Engineering, University of New Mexico, 2014

M.S. Mechanical Engineering, University of New Mexico, 2017

Ph.D. Engineering, University of New Mexico, 2019

ABSTRACT

The goal of this dissertation is to provide a foundation for the advancement of additive manufacturing (AM) toward production of high-performance carbon fiber reinforced polymer matrix composites (CFRPs). AM can provide valuable advantages over conventional composite manufacturing techniques, including the control over fiber orientation, capability of manufacturing complex geometries, out-of-autoclave processing, elimination of the need for composite tooling, and the ability to perform lights-out manufacturing. Currently, however, a suite of challenges related to modelling, design, manufacturing defects, and general limitations in the current understanding of the processing-structure-property relationships exist in AM of composites. To this end, this dissertation investigates novel approaches to modelling of continuous fiber AM composites using local anisotropic material properties, utilizing design optimization for AM composites, post-processing high-value composites to remove internal porosity, and determining the processing-structure-property relationships of AM CFRPs across the nano-, micro-, and meso- length scales.

Table of Contents

List of Figures

List of Tables

Chapter 1. Introduction

1.1 Motivation

Fiber reinforced polymer matrix composites (FRPs) have been of great interest to academic and industrial communities for decades due to their unique and exceptional combination of properties. In the case of carbon FRPs (CFRPs), the low density, high strength, and high modulus make for ideal use in high-performance markets where mass is a critical design factor. Additionally, CFRPs commonly exhibit creep, chemical, and corrosion resistance, along with low thermal expansion. As such, they have found significant adoption into aerospace, wind, automotive, and luxury sports markets, as seen in Figure 1.

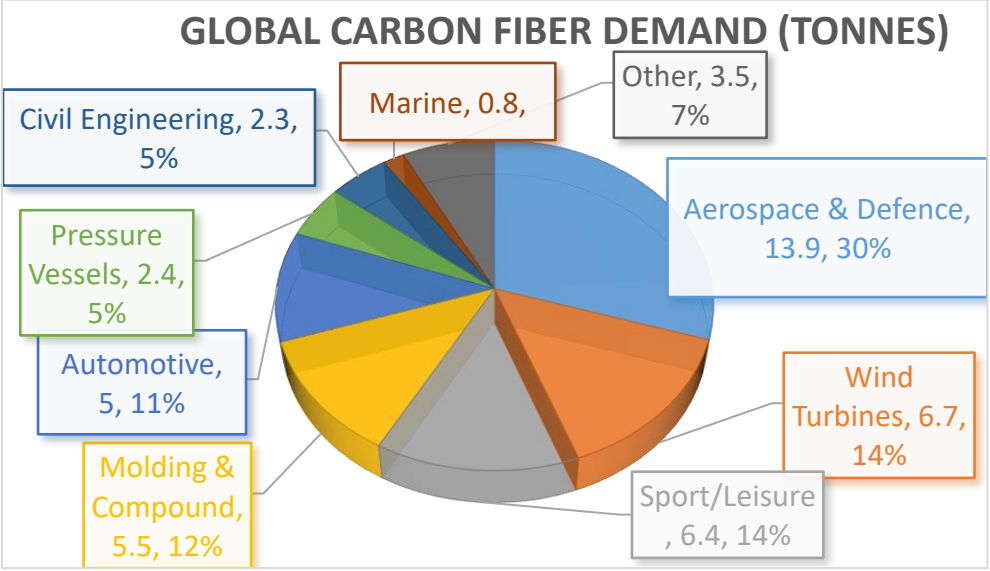

Figure 1. Carbon fiber composite mass consumption by industry in 2016. [1]

CFRPs have conventionally been manufactured through processes such as liquid compression molding, in which fibers in the form of unidirectional tapes or woven mats are impregnated with a polymer resin under elevated temperatures and pressures in a mold. The fiber mats can contain continuous or short fibers and be oriented in one or multiple directions, as illustrated in Figure 2.

The composite thickness is produced by stacking laminas to make each laminate, and the stacking sequence of the laminates is used to vary the laminate properties between anisotropic and quasi-isotropic. Optimization of the stacking sequence for given forces and constraints can

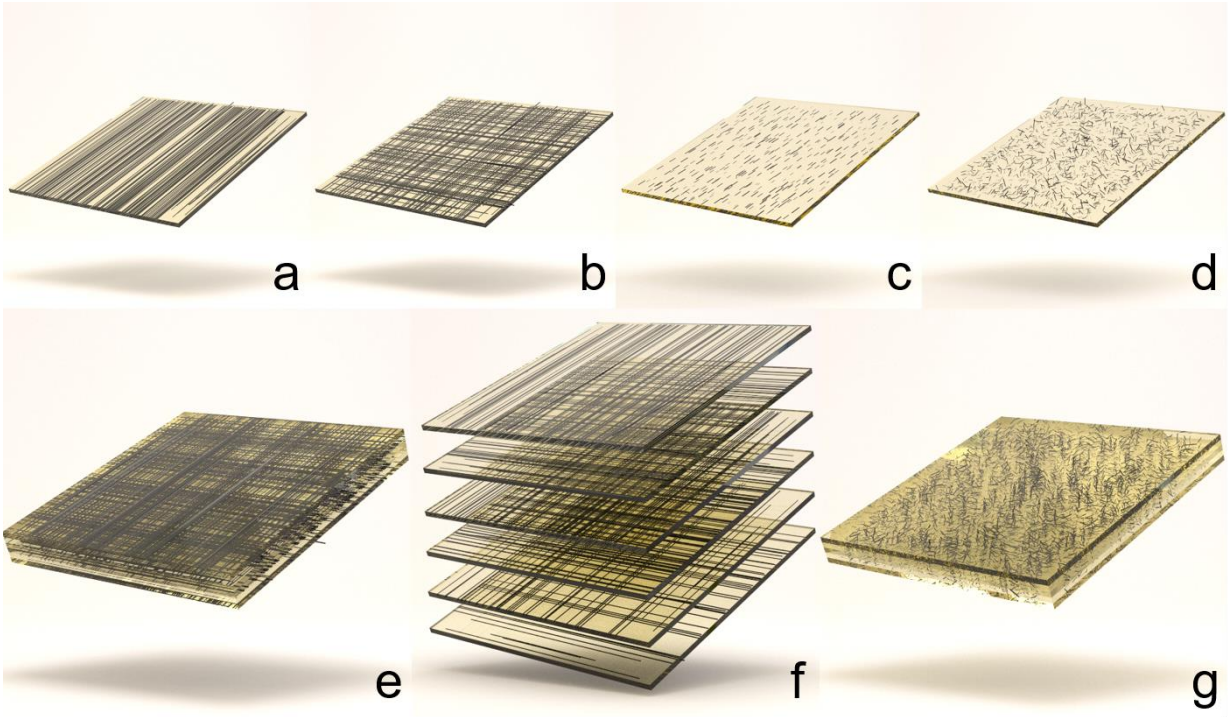

Figure 2. Schematic of conventional manufacturing of FRPs. a) Unidirectional continuous fiber lamina. b) Bidirectional continuous fiber lamina. c) Unidirectional discontinuous fiber lamina. d) Randomly oriented discontinuous fiber lamina. e) Continuous fiber composite laminate. f) Exploded view of continuous fiber composite laminate. g) Discontinuous fiber composite laminate.

allow for a reduction in the number of laminas required for the part, and ultimately reduce the material cost and mass of the composite. Molds are required for traditional composite manufacturing, though they are expensive and require long lead times to manufacture. Additionally, as this material class is inherently orthotropic, with axial tensile properties easily an order of magnitude greater than transverse, CFRPs can suffer from limitations in applications supporting complex states of stress.

The research attention garnered by CFRPs over the years has yielded substantial improvements in properties and understanding of the multifaceted material class. With average fiber diameters

of 5-7μm, and fiber-matrix interphase thicknesses typically on the order of tens to hundreds of nanometers, CFRPs are inherently multi-scale structures. Modelling approaches based in mechanics and finite element analysis have been developed to understand and predict composite strength, stiffness, and failure modes both at the micro- and meso-scale. Interface engineering has been implemented to improve the fiber-matrix interlaminar shear strength (ILSS) and interfacial fracture toughness via polymer sizing, incorporation of nanomaterials, changes to the fiber surface chemistry, or changes to the polymer chemistry. Additionally, advancements in manufacturing methods have yielded reductions in void content and defects at high fiber volume fractions, often with shorter polymer curing cycles and out-of-autoclave processing.

Additive manufacturing (AM) can be used to address some of the key limitations of conventional composite manufacturing. For one, AM can be used to produce composites without the need for tooling, leading to significant reductions in the time and cost required to move from design to finished part. This is particularly relevant for applications requiring low-volume production, which are common in aerospace and defense. AM can also allow for full control over the placement and orientation of carbon fibers within a composite part. With this design freedom, optimization methods can be implemented to minimize part compliance by selectively placing and orientating fibers for a known geometry and loading condition. Lastly, AM is a form of lights-out manufacturing, in which little to no human labor is required, allowing for significant cost savings during manufacturing.

While AM offers a suite of novel benefits to composite manufacturing, the addition of new interfaces, defects, and polymer microstructures also demands further study. Most significantly, AM commonly results in composite parts with a high degree of internal porosity, degrading the material performance. Additionally, the rapid cooling rates in fused filament fabrication (FFF)

result in low polymer crystallinity, which has a significant effect on matrix or interface dominated properties. The inter-layer and inter-filament interfaces in FFF composites can result in additional changes to the failure characteristics of AM composites compared with conventional methods. Post-processing of AM composites targeted at these deficiencies, and the corresponding process-structure-property relationships, are investigated in this study.

Lastly, there currently exists insufficient framework to accurately model and design high-value AM composites. Continuous carbon fiber composites can be manufactured with curved fiber paths, which differs significantly from the traditionally straight paths of conventional composites. This can create unexpected and complex states of stress in the material for a given loading condition, which need to be well understood to aid in design and predict failure. Additionally, optimization methods in design can be used to exploit the capacity of custom fiber placement and orientation to improve composite properties for known loading and constraint conditions. These two deficiencies are also investigated in this study.

1.2 Dissertation Overview

This dissertation will work to address the modelling, optimization, and material science perspectives of additively manufactured continuous carbon fiber composites. First, in Chapter 2, the current state of the art in additively manufactured composites will be presented. This review will cover relevant prior work in both discontinuous and continuous fiber composites in AM and lay the foundation for the motivation of the present study. The development of fiber reinforced AM in both academia and industry will be explored, along with predictions of the application spaces most well suited to benefit from the technology.

Chapter 3 will investigate a modeling framework for predicting mechanical properties and failure modes in continuous fiber AM composites. The continuously varying anisotropic properties of

fiber reinforced composites containing curved internal fiber morphology is not inherently well suited for modelling by existing finite element analysis techniques. As this is necessary for accurately predicting the mechanical response and failure of additively manufactured continuous fiber composites, an FEA technique was developed to assign anisotropic properties to each element corresponding to the orientation of fibers within a printed part. The mechanical properties and composite failure predictions were compared with experimental results, which allowed for the development of a basic set of design guidelines for AM CFRPs.

The use of topology and fiber placement and orientation (morphology) optimization in the design of AM CFRPs is investigated in Chapter 4. Three benchmark geometries and loading profiles were used in this study, being an MBB, cantilever, and L-shape bracket. Fiber paths designed to minimize specific compliance of each part were generated using various optimization techniques and evaluated using FEA. The parts were then manufactured using a custom-built continuous carbon fiber printer. The specific stiffness of each part was evaluated by applying force and constrains consistent with the design of each part and digital image correlation (DIC) to capture full-field strain and displacement. The performance of each part was then compared to the model predictions.

Chapter 5 investigates the potential for AM thermoplastic composites to be utilized in AM CFRPs for high-value applications. Carbon fiber reinforced PEEK composites were printed, and an investigation into post-processing treatments to improve their mechanical properties was conducted. As FFF endows parts with residual thermal stresses, high void content, weak inter-filament interfaces, and low polymer crystallinity, it is often necessary to post-process AM composites to reduce these deficiencies. Hot isostatic pressing (HIP) was performed on printed PEEK CFRPs to study the relationship between structural changes and mechanical properties.

The correlation of flexural, interlaminar, tensile, compressive, and microstructural properties of printed CFRPs on processing temperature and pressure were the focus of this investigation.

The relationship between the polymer matrix, and fiber-matrix interfacial properties, and the bulk mechanical properties as a function of HIP treatment is further investigated in Chapter 6. As polymer crystalline morphology and residual stress can impact the interfacial strength of fiber reinforced composites, and interfacial characteristics are known to impact the bulk mechanical performance of a composite, it is necessary to fully understand the influence of post-process treatments on the fiber-matrix interface of the composite. The interfacial shear strength and crack formation/propagation characteristics of the treated and reference composites were evaluated using single fiber push-out tests, in which nanoindentation is used to apply force on single carbon fibers. Single loading curves can be used to evaluate the maximum force required to debond the fiber, which can be used to find the interfacial shear strength of the system. Cyclic loading/unloading curves can be used in an energy-based approach to find the indentation depth at which cracks form at the interface and propagate through the material. This information is then correlated to the interphase thickness, as investigated through mechanical mapping via atomic force microscopy. Lastly, the polymer and interphase properties are correlated to the HIP treatment conditions and bulk mechanical performance to elucidate the relationship between nano-, micro-, and meso-scale properties continuous fiber AM composites.

Lastly, Chapter 7 discusses conclusions that can be found from each aspect of this dissertation, along with recommendations for future work that can build off the results found here.

Chapter 2. Additively Manufactured Carbon Fiber–Reinforced Composites: State of the Art and Perspective

Nekoda van de Werken[a], Halil Tekinalp[b], Pouria Khanbolouki[a,c], Soydan Ozcan[d], Andrew Williams[e], and Mehran Tehrani[a,c]

[a] Department of Mechanical Engineering, University of New Mexico, Albuquerque, NM

[b] Energy and Transportation Science Division, Oak Ridge National Laboratory, Oak Ridge, TN

[c] Walker Department of Mechanical Engineering, University of Texas, Austin, TX

[d] Chemical Sciences Division, Oak Ridge National Laboratory, Oak Ridge, TN

[e] US Air Force Research Laboratory, Kirtland Air Force Base, Albuquerque, NM

While polymer additive manufacturing (AM) has advanced significantly over the past few decades, the limitations in material properties, speed of manufacture, and part size have relegated this technology to the space of rapid prototyping rather than the legitimate manufacture of end-use parts. Carbon fiber offers a low density, a low coefficient of thermal expansion, and high thermal conductivity and is an ideal material for bringing polymer-based AM from the realm of form and fit to that of form, fit, and function. Use of carbon fiber in AM can improve material properties, reduce the time required to manufacture functional parts compared with traditional subtractive technologies, and reduce warping, thereby enabling a larger possible build envelope. Therefore, the addition of carbon fiber to various AM technologies is of increasing interest in academic and industrial communities; this paper examines the work performed in that area to date. Specifically, the effects of fiber reinforcement on the structure and mechanical properties of 3D printed parts are investigated within the body of literature. Upper bounds for tensile properties of carbon fiber composites are theoretically evaluated and compared with experimentally measured values. Moreover, current and potential applications of additively manufactured carbon fiber composites in the context of desktop 3D printing and big area AM are

discussed. This review is intended to organize and synthesize the present body of work surrounding AM of carbon fiber–reinforced plastics, identify the most promising technologies, and prescribe viable research and development path forward to advance AM from the application space of rapid prototyping to that of functional, load-bearing, end-use parts.

2.1 Introduction

Carbon fiber–reinforced polymer composites (CFRPs) offer significant advantages over metals in that they are lightweight, have high strength and stiffness, and are resistant to corrosion and fatigue [2]. Thermosetting epoxy matrices are used in most CFRPs where a high strength-to-weight ratio and stiffness is necessary, as in aerospace applications. Carbon fiber surface treatments and sizing technologies have been developed for aerospace epoxy thermoset matrices over the years, achieving high interfacial fiber-matrix bond strength and favorable mechanical properties. Thermosetting resins have also seen a precipitous decrease in curing time over the last decade, from tens of hours to less than a minute [3]. While surface treatments for other thermosetting matrices have not been developed to the extent of epoxies, the advances in thermosetting polymers have opened new avenues for their additive manufacturing (AM) [4].

Thermoplastic matrices, on the other hand, do not readily form strong bonds with the carbon fiber surface, have a relatively high melt viscosity, and are comparatively expensive. However, they offer a few notable advantages in CFRP manufacturing. One advantage is their melt processability. This translates to rapid manufacturing of composite parts, significantly lowering the manufacturing costs by eliminating the need for prolonged cure cycles or sophisticated cure chemistries. Thermoplastics can, therefore, be manufactured using widely developed and readily

accessible polymer AM techniques. AM of fiber-reinforced thermoplastics has recently emerged for the manufacturing of strong, stiff, and tough parts without the need for multiple processes and special tools [5].

Research on AM polymer matrix fiber composites can be broadly sectioned into discontinuous (short) and continuous fiber composites. For short-fiber composites, AM fabrication techniques include fused deposition modeling (FDM), stereolithography (SLA), selective laser sintering (SLS), and extrusion of photo-curable or thermally curable filled resins. Each method is explained briefly in Section 2.2. It is common to mix short fibers with a polymer to create a composite part with enhanced properties. Specifically, adding carbon fiber to a polymer feedstock leads to an increase in thermal conductivity, a decrease in thermal expansion, substantially reduced warping in larger prints, a reduction in residual stresses within the part, and an increase in the dimensional accuracy of printed parts. Carbon fiber can also substantially increase the strength and stiffness of AM parts, thereby increasing the potential for end-use parts (beyond prototyping). Finally, AM can be combined with filament winding or automated tape placement to produce hybrid structures that dramatically reduce manufacturing time. To this end, AM can be used for highly complex components of a structure, while automated manufacturing approaches can produce larger, more simple geometries in shorter times and typically with improved material properties. In this light, carbon fiber has the potential to move AM technology from rapid prototyping to end-use rapid manufacturing [6].

Another important development in the field of AM is big area additive manufacturing (BAAM) by which industrial-scale parts can be manufactured using FDM [7]. Typically, this process has involved the extrusion of short carbon fiber-filled thermoplastic pellets through a nozzle. As mentioned earlier, the carbon fiber improves the mechanical properties of the material and

reduces the coefficient of thermal expansion (CTE), thus reducing part warping and cracking [6]. Large nozzle diameters of 7.6 mm and 5.1 mm used for coarse and fine resolutions, respectively, allow for deposition rates of 25-50 kg/hour [7, 8]. This functionality has made it possible to print an impressive array of large-scale objects, including a submarine hull, an excavator cab, a Shelby Cobra replica, an F-22 Raptor replica, and an Orion Spacecraft replica [7]. With print times for the F-22 Raptor and Shelby Cobra replicas of 8 and 12 hours, respectively, the potential for this technology to disrupt traditional manufacturing methods is clear [7].

The specific (per weight) and regular tensile properties of additively manufactured metals, polymers, and fiber-reinforced polymer composites are plotted in Figure 3. Short fibers provide moderate improvements over a base polymer due to the issue of critical fiber length, but continuous fibers radically improve polymer properties by up to two orders of magnitude, thereby surpassing the specific (per density) mechanical properties of additively manufactured metal products. State of the art in AM composites is the continuous carbon fiber reinforcement of commodity, engineering, and high-performance polymers, as well as BAAM. Additive manufacturing of continuous fiber composites is most commonly accomplished using FDM.

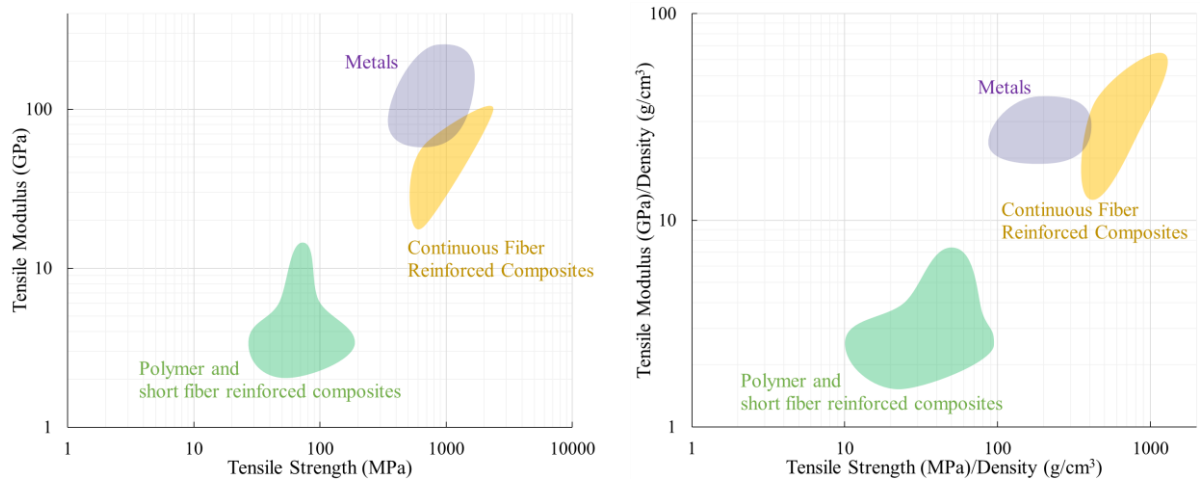

Figure 3. Ashby plot for regular (left) and specific (right) tensile properties of additively manufactured materials to date [9-18]. Reported properties for the continuous fiber reinforced

Although in its infancy, the composites AM is a rapidly developing field in both industry and academia. Several reviews of composite AM technologies have been published in the last three years [19-22]. These are critical to provide a context for the utility of this technology commercially and provide insight into future directions for valuable research. Available reviews of state of the art and perspectives on the technology focus primarily on academic and fundamental research that will enable the growth of AM and its incorporation into larger, more creative design spaces. These reviews, however, do not adequately address the transition of additively manufactured composites from research laboratories to competitive, high-value applications. This review aims to consolidate relevant studies and available literature, and provide insight into the physics, mechanics, and materials science of the AM process and AM composites. In addition, it aims to add to the perspective of appropriate industries and

applications for additively manufactured composites, specifically CFRPs, and suggest enabling technologies to accelerate this transition. Doing so will in turn help to highlight the most valuable areas contributing to the development of AM carbon fiber-reinforced composites for practical applications. We discuss and identify some of the past research in this field, along with the challenges and the material properties obtained. The effects of the fiber-matrix interface, fiber volume fraction, and length/orientation distribution on the effective mechanical properties of AM composites are also discussed in light of theoretical and experimental research.

2.2 Additive Manufacturing of Short Fiber–Reinforced Plastics

Short fibers are perhaps the most common reinforcement used in AM, with good reason. Discontinuous fibers can be implemented in a variety of AM technologies without substantially altering the manufacturing process, and they allow for improvements in the strength, stiffness, creep resistance, thermal expansion, or toughness of the material, depending on the type of fiber used. Their ease of implementation and the improvements they enable in processes and properties make short fibers an attractive option for many AM applications. However, the advantages of short-fiber reinforcement are limited by the lengths of fibers that are often used as reinforcement compared with the critical length of the fiber-matrix system and the increase in volume defects that often occurs in AM of fiber-reinforced parts. An example of the increase in the void content of AM parts over that in compression-molded short-fiber composites can be seen in Figure 4.

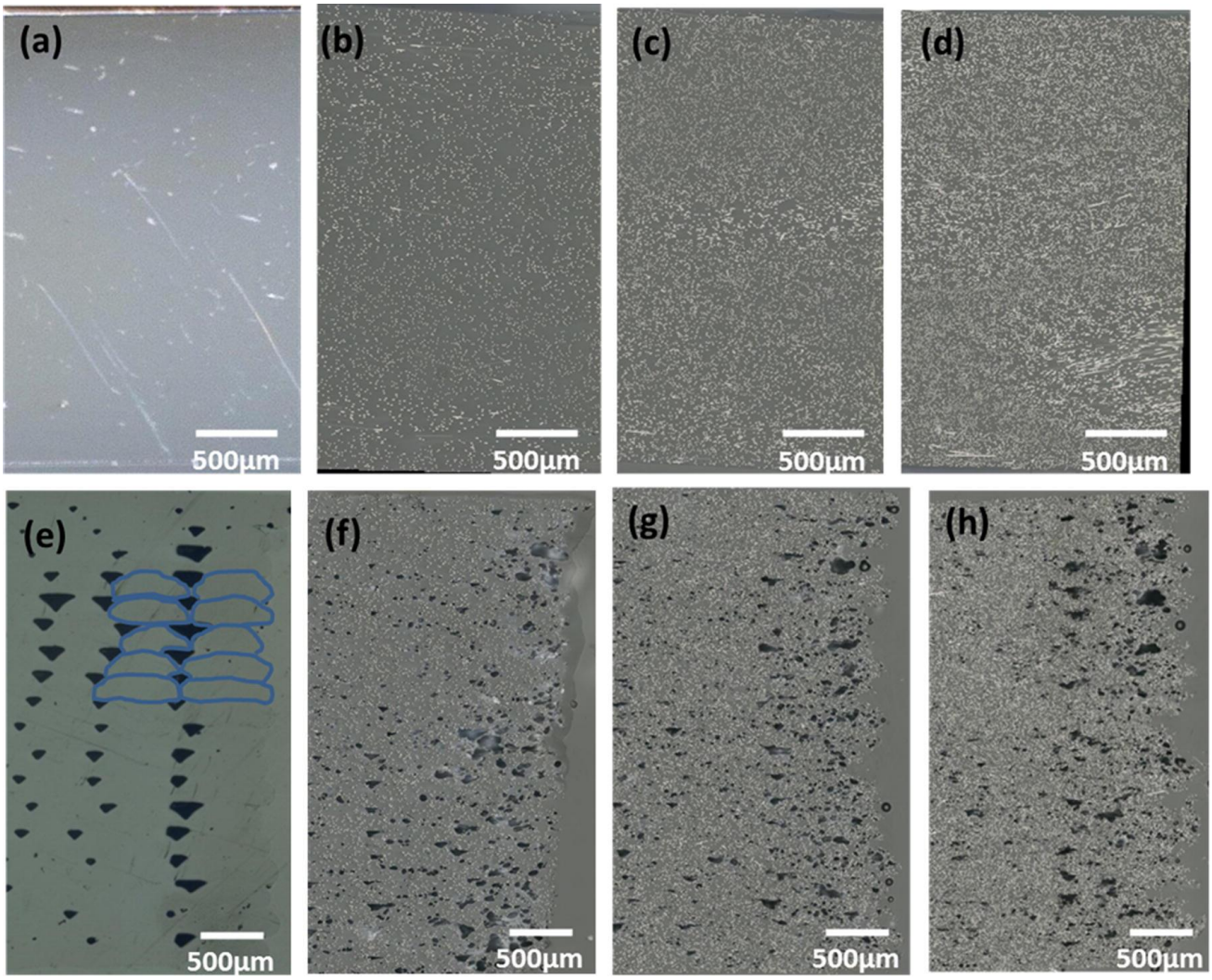

Figure 4. Cross-sectional micrographs of compression-molded short-fiber composites (top) and short fiber composites additively manufactured via FDM (bottom). The fiber volume fraction increases from left to right. [23]

2.2.1 Extrusion-Based Additive Manufacturing

Extrusion-based AM is possibly the most common polymer 3D printing approach. It is based on simple extrusion and deposition of molten polymer material layer-by-layer in a controlled pattern. Depending on the technique, filament or a pellet feedstock can be used. Apart from the feedstock form, the success of the printing process can be affected by many parameters,

including feeding, melting, extruding, and depositing of the material. Furthermore, there is a large temperature gradient among the layers due to the nature of the layer-by-layer deposition process. The temperature difference builds up residual stress among the layers, which may eventually lead to distortion of the part, failing the whole printing process.

2.2.2 Fused Deposition Modeling (FDM)

Fused deposition modeling, also referred to as fused filament fabrication, is one of the most common polymer 3D printing methods. As shown in Figure 5, this technique involves melting a thermoplastic polymer filament inside a print head nozzle and extruding the molten material onto a print bed. In a layer-by-layer process, the print head extrudes all material defined for a single XY plane, moves its Z axis by the thickness of one layer, and repeats the process. Support structures, particularly using soluble materials, can increase the possible geometries and improve the part surface finish. Common FDM materials (thermoplastics) include polylactic acid (PLA), acrylonitrile butadiene styrene (ABS), acrylonitrile styrene acrylate, polycarbonate (PC), polyamide (nylon), glycol-modified polyethylene terephthalate (PETG), and high-impact polystyrene [14]. High-performance thermoplastics such as polyetherimide (brand name ULTEM), Polyphenylene sulfide (PPS), polyphenylsulfone (PPSU), and the polyaryletherketone (PAEK) family also can be printed using FDM; however, they are relatively expensive and much less prevalent in the field [14].

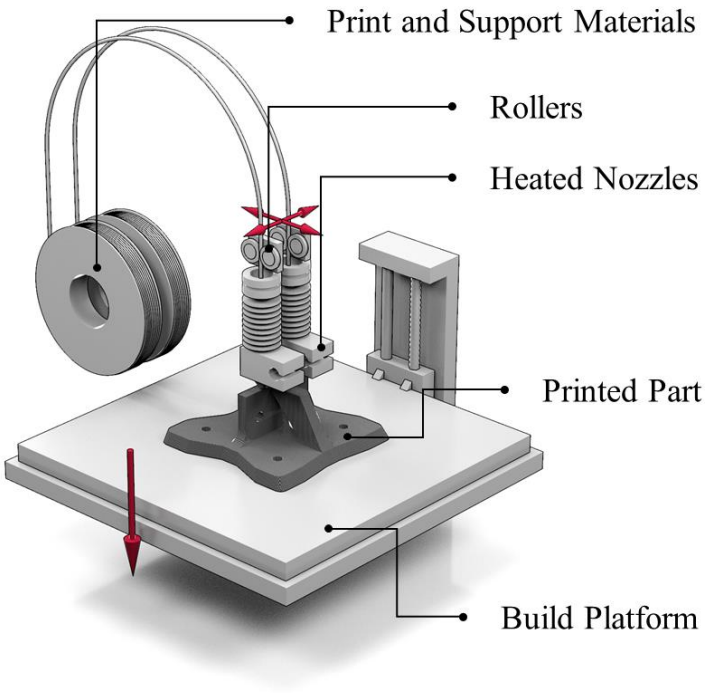

Figure 5. Schematic of fused deposition modeling. Red arrows indicate relative mechanical motion of components.

Duty et al. developed a viscoelastic model that relates the fundamental requirements for the successful printing of a neat and a fiber-reinforced material [24]. The model considers four factors: (1) pressure-driven extrusion flow, (2) bead formation, (3) bead functionality, and (4) component functionality [24]. The paper lists the basic rheological and thermophysical properties needed for a material to be printable. First, it needs to be pushed through the orifice/nozzle at the desired rate at the pressure limits of the system. Satisfying this requirement depends on the viscosity of the material at the printing temperature and the shear rate, both of which can reduce viscosity. Note that adding fibrillar reinforcements increases the viscosity of the material. Second, the extruded bead should form a stable geometry and keep its shape during deposition. Although increasing the extrusion temperature helps to further reduce the viscosity, it may hinder stable bead formation. The stability of the bead shape depends on the surface energy. As the bead

bridges over free-spanning gaps, it must not sag much as a result of infill patterns and overhangs. Furthermore, to ensure successful printing, the deposited bead must serve as a solid substrate for the layers that follow it, creating sufficient resistance to redirect the flow without significant deformation and having sufficient strength to carry the subsequent layers. Finally, the high CTE of polymeric materials can lead to dimensional changes after deposition, as well as residual stress buildup. The final printed component must retain its shape and be dimensionally accurate.

Kishore et al. studied the thermal and rheological properties of polyetherketoneketone (PEKK) and PPS polymers and their carbon fiber composites to determine appropriate processing conditions for extrusion-based printing [25, 26]. Both PEKK and PPS are semi-crystalline high-performance polymers, and their successful use in AM can reduce manufacturing costs and lead times in the aerospace and tooling industries. The viscosities of both short-fiber loaded polymers showed a higher dependence on shear rate than on temperature, and the shear thinning behavior increased with the addition of carbon fibers. At low shear rates, the viscosity of both PPS and PEKK short fiber composites increased at higher processing temperatures, a behavior which was more pronounced at higher fiber loadings. This behavior was possibly due to the high processing temperatures at which chain scission and oxidation/crosslinking reactions are favored. The rheology measurements were used to determine the printing conditions with reference to ABS, a commonly used FDM material, and printing of selected formulations was demonstrated [26]. The viscosity of carbon fiber–reinforced PEKK grades was found to be less stable in air at elevated temperatures than that of neat PEKK grades, suggesting an inert gas should be used for processing [25].

Although rheology measurements provide sound guidance for determining the range of processing/printing conditions for extrusion-based AM, the conditions selected can significantly

impact the mechanical properties of the printed part. An out-of-oven, layer-by-layer manufacturing approach leads to the cooling of a deposited layer below its glass transition temperature before the following layer is deposited, thereby limiting the adhesion between layers. Weak adhesion is one of the main downsides of extrusion-based AM and leads to low build-direction (z-direction) strength. Moreover, triangular or quadrangular voids often formed during FDM act as stress concentration sites, further reducing the z-direction part strength.

As shown in Figure 6, an FDM composite part is a multiscale structure that entails several interfaces. At the smallest length scale, fiber-matrix interfaces control the stress distribution to fibers and strongly control macroscale properties. Defects in the form of voids exist in the filament, which then turn into voids in the printed beads. Beads in each layer (the lamina level) meet one another and form bead-bead interfaces. Each lamina, in turn, meets another lamina at the interlaminar interface, which is often weaker than the bead-bead interface because of the lack of polymer diffusion. Where beads meet one another, voids inevitably form. These voids act as stress concentration sites and reduce AM part performance. The mechanical design of AM composites, therefore, requires a thorough understanding of the structure and mechanics of this new class of materials. Several approaches have been reported to improve interlayer adhesion in AM parts. Infrared heating of a deposited layer to above its glass transition temperature right before the deposition of the new layer was shown to significantly improve the interlayer adhesion on large-scale printed carbon fiber ABS samples [27]. In another approach, leaving and aligning voids in successive layers and backfilling them vertically with a continuously extruded material resulted in improvements in z-direction properties. The “z-pinning” approach led to a 20% increase in z-direction strength while doubling the modulus in the z-direction [28]. More recently, hot isostatic pressing of an AM CFRP close to its glass transition temperature was

shown to reduce the number of voids in specimens and result in more than 30% improvements in flexural strength, flexural stiffness, and interlaminar shear strength over the reference samples [29].

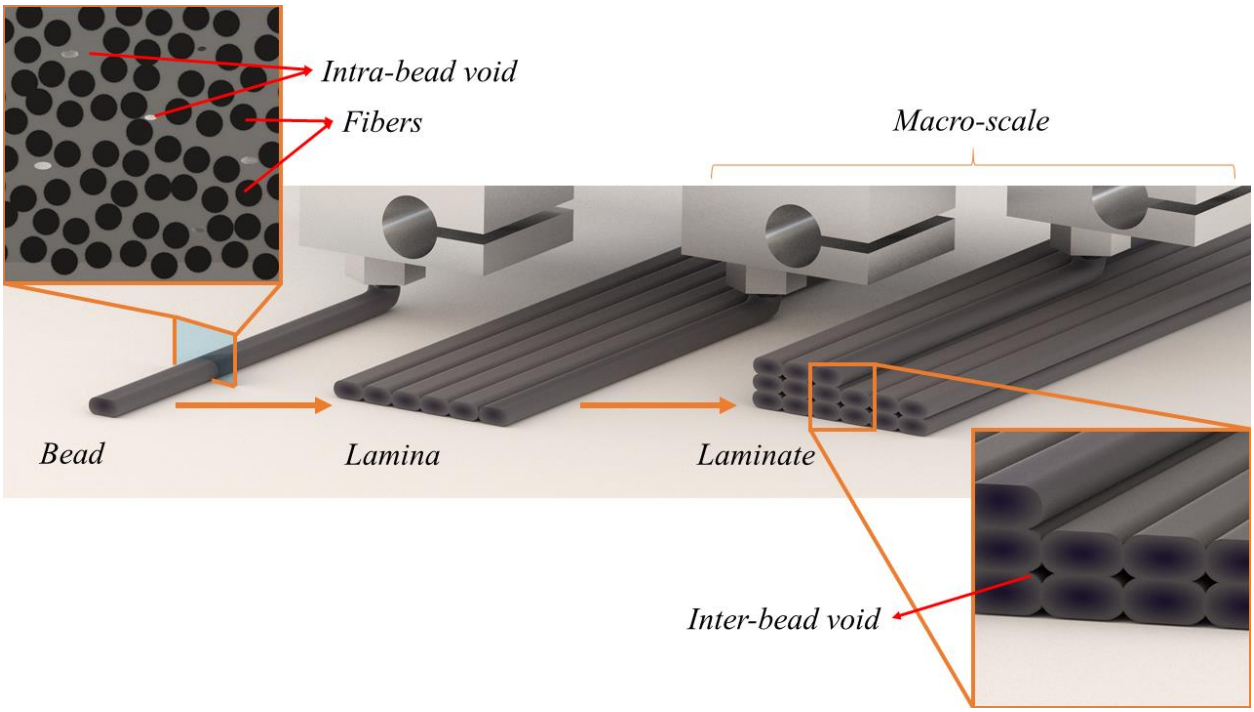

Figure 6. Schematic of the multiscale structure of fiber-reinforced composite parts manufactured via FDM.

Short-fiber reinforced FDM composites are created by incorporating chopped fibers into the polymer filaments before printing. The fibers are typically an order of magnitude shorter than the nozzle diameter to prevent blockage, to which this method of composite manufacturing is prone [5]. The fibers tend to align both during filament manufacturing by extrusion and, because of shear forces, as they exit the nozzle during printing. This alignment leads to anisotropic properties, with the highest mechanical properties along the direction of the printed beads [23]. The polymer melt rheology also changes significantly with the addition of fiber reinforcement;

the rheology changes typically limit the volume fraction to less than 20%, although carbon fibers with volume fractions of up to 40% have been successfully printed and characterized [23].

Glass fiber–reinforced ABS was one of the earliest fiber-reinforced AM composites [30]. The short glass fibers were found to embrittle the ABS, making it nearly impossible to extrude and print. By adding a plasticizer (linear low-density polyethylene, or LLDPE) to improve toughness and a compatibilizer (hydrogenated Buna-N) to improve homogeneity, the composite could be printed, and strength was found to increase by up to 2.4 times over reference samples for 30 vol.% glass fibers [30]. Vapor-grown carbon fibers (VGCF), with diameters and lengths on a scale of 100 nm and 100 μm, respectively, have also been mixed with ABS and printed using FDM [31, 32]. The microstructures of composites with up to 10 wt.% nanofibers were investigated, finding uniform dispersion, highly oriented fibers along the print direction, and limited porosity in the filled filament. Addition of the nanofibers resulted in increases in tensile strength and modulus of up to 39% and 60%, to 37.4 MPa and 0.79 GPa, respectively. Composites containing either 5 wt.% VGCF or single-wall carbon nanotubes (SWCNTs) were also manufactured using FDM and characterized [32]. While adding SWCNTs to ABS increased the strengths and moduli of the composite filaments by 31 and 93%, respectively, the strength of printed parts was not increased, and their moduli were improved by only 26%. Additionally, the addition of SWCNTs resulted in the greatest increase in material viscosity and the largest reduction in material strain to failure.

Effects of carbon fiber content on microstructure and mechanical properties of ABS have been investigated in several studies. For example, carbon fiber reinforced ABS tensile coupons manufactured using both compression molding (CM) and FDM have been investigated [23]. The fiber length distribution, microstructure, and mechanical properties were characterized for each

fiber weight fraction (0, 10, 20, 30, 40 wt.%). The mechanical properties of the CM and FDM composites were found to be similar for low fiber volume fractions, but greater improvement in properties was found in CM composites at higher volume fractions. The strength and modulus of CM parts increased from about 36 MPa and 2 GPa for neat ABS to 68 MPa and 14 GPa for specimens containing 40 wt.% carbon fiber. However, there was only a marginal change in the mechanical properties of FDM parts between the parts with 30 and 40 wt.% fiber content. This was attributed to an increase in the porosity of the FDM parts as the fiber content increased, as shown in Figure 4. In another study, chopped carbon fibers were mixed with ABS in 0, 3, 5, 7.5, 10, and 15% fractions [5]. The highest strength and stiffness were found for 7.5% carbon fiber (~44 MPa strength vs. ~35 MPa for 0% loaded sample). Larger volume fractions resulted in decreases in both strength and ductility, attributed to increases in void content with increasing volume fraction [5]. Average fiber lengths of 150 and 100 μm were used to make AM composite coupons; the coupons with 150 μm fibers displayed an increase in strength and stiffness but a decrease in ductility [5]. Carbon fiber ABS composites were manufactured with FDM, and the mechanical properties were probed as a function of the print parameters [33]. It was found that matrix fracture and fiber-matrix debonding resulting in fiber pullout were the primary failure modes of the specimens. The addition of carbon fibers increased the tensile strength and modulus and in-plane shear strength and modulus compared with neat ABS.

PLA-reinforced filaments have been also examined for AM. PLA specimens containing 15 wt.% carbon fiber, with average length and diameter of 100 and 7.2 μm, respectively, were additively manufactured and characterized [34]. The distribution and orientation of carbon fibers were investigated via computed tomography, showing a high degree of fiber alignment. Scanning electron microscopy (SEM) of the polished and fractured composite cross-sections also revealed

well-aligned fibers, along with significant voids in the polymer matrix. The fractured surfaces showed substantial fiber pull-out with little polymer residue on the fiber surface, indicating low interfacial shear strength. These results are common to almost all thermoplastics reinforced with carbon fibers, as there is usually poor interaction between carbon fiber surfaces and thermoplastics [34, 35].

Apart from the carbon fiber loading and alignment, AM processing parameters play a major role in the microstructure and mechanical performance of AM parts. Ning et al. studied the effect of raster angle, print speed, nozzle temperature, and layer thickness on properties of 5 wt.% carbon fiber reinforced ABS composites [36]. It was found that (0°, 90°) raster-produced composites with higher strength and modulus and a (–45°, 45°) raster resulted in higher strain-to-failure and toughness [36]. Raster angle here corresponds to the printing schedule of beads or rastering in each printing layer, where a 0° angle corresponds to an arbitrary axis, usually along the length of the printed part, and the beads in the 90° layer are perpendicular to the 0° axis. A median nozzle temperature of 220 °C produced the highest strength, modulus, and ductility among the temperatures tested. Lower temperatures produced lower interfacial bonding between printed layers, and higher temperatures produced voids that reduced the mechanical properties [36]. In general, printing with thinner layers resulted in higher strength and stiffness, as thinner layers produce more tightly packed beads and encourage inter-filament bonding, although a layer of 0.25 mm produced samples with the highest toughness [36]. In another study, commercially available carbon fiber-filled filaments were investigated [37]. Specifically, they explored the effects of carbon fibers on the tensile properties of printed composites with differing printed bead directions for a variety of polymer matrices. The polymer matrices used for these filaments included PLA, ABS, PETG, and a copolyester filament brand named Amphora. The tensile

strength along the bead direction was always improved, although the strength perpendicular to this direction often decreased with the addition of carbon fiber. In every bead orientation, adding carbon fiber resulted in a significant decrease in the tensile elongation of the printed composites. SEM images revealed that clean carbon fibers typically pulled out of the matrix on the fracture surface, indicating low interfacial shear strength (weak fiber-polymer bonding). Additionally, the carbon fiber length distribution was found for each composite, with typical average lengths between 50 and 100 μm. Only a slight reduction in fiber length was observed between the filaments and printed components [37].

The mechanical properties and microstructure of PLA and 15 wt.% carbon fiber filled PLA parts printed using FDM were studied in a recent study [38]. The addition of carbon fiber increased E_1, E_2, and G_{12} by 120%, 25%, and 16%, respectively; but it predictably resulted in a reduction in ductility; 1 refers to the direction in which the fibers are aligned, and 2 is perpendicular to it. SEM indicated that fibers were aligned along the print direction, i.e., the 1 direction [38]. Chopped carbon fiber nylon composite filaments (up to 10 wt.% carbon fiber) were fabricated, and the thermal and mechanical properties of their FDM manufactured parts were investigated. The 10 wt.% composites exhibited the highest impact strength, flexural strength and modulus, thermal conductivity, storage modulus, and glass transition temperature of the materials tested [39].

2.2.3 Big Area Additive Manufacturing (BAAM)

BAAM is an extrusion-based AM technique similar to FDM that uses a feedstock in pellet rather than filament form. The build volume and printing rates are orders of magnitude higher than those of regular FDM units. BAAM systems work based on a single screw extruder attached to a

large gantry system, which enables direct feeding of feedstock material in pellet form without the need for converting it into filaments.

The initial BAAM technology was developed by Oak Ridge National Laboratory (ORNL) and Lockheed Martin with the goal of printing larger components at higher rates with a lower-cost feedstock material [40]. To this end, a single screw single extruder was attached to a large gantry system (2.4 × 2.4 × 2.4m) that can achieve up to 50 kg/h throughput (Figure 7). The deposition head had the capacity to move at a speed of 12.7 cm/s in the X-Y plane. Carbon fibers were added to the feedstock materials to minimize distortion of the parts during printing. A lack of carbon fibers results in large residual stresses, inhibiting the printing of large parts except in an oven. Since the system started using pellets directly as a feedstock, the cost of converting a feedstock into filament form has been eliminated, bringing the cost of parts down significantly.

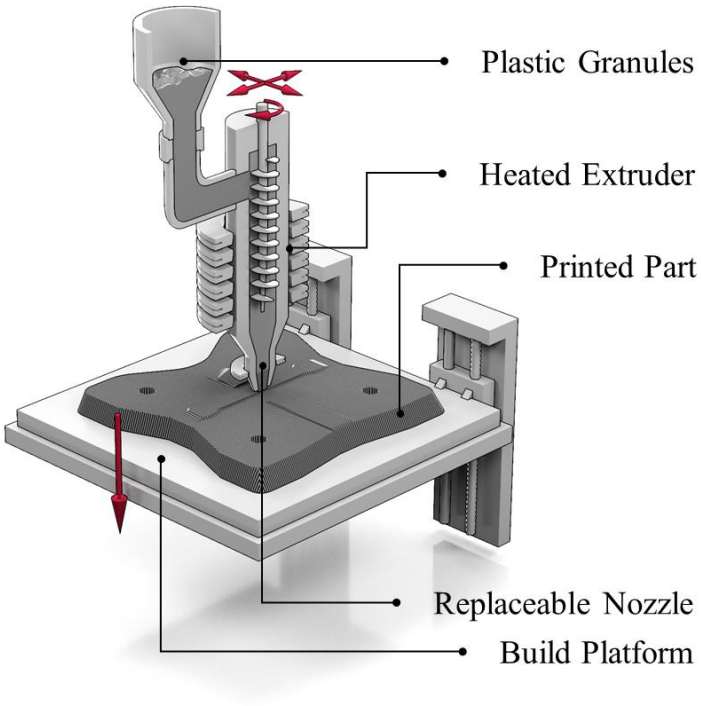

Figure 7. Schematic of the screw-based pellet extruder used in high-throughput BAAM.

While the initial BAAM system development was more of a proof-of-concept (the technology readiness level, or TRL, was 2–3), ORNL later partnered with Cincinnati Inc. to develop a BAAM system at a prototype product stage (TRL 7–8), which is now commercially available. The new system offers a process that is over 200x faster, 10x larger in part size, and 20x cheaper compared with conventional extrusion-based AM systems [41]. A tamping mechanism developed by ORNL has significantly improved the interlayer adhesion, almost doubling the interlaminar strength [41].

BAAM is an out-of-oven process and is prone to high residual stress buildup due to the high CTE of polymeric materials and high-temperature gradients between adjacent layers. The residual stress builds up as more layers are deposited. If the residual stress overcomes the stiffness of the already printed portion of the component, and the adhesion between the component and the build sheet, the component comes off the bed, and the print fails. The use of

carbon fiber as an enabling material is crucial at this point. Adding short carbon fibers to the feedstock not only improves the strength and modulus of the material but also enhances the dimensional stability and the thermal conductivity [40]. Adding 13% carbon fiber to ABS decreased the CTE of the FDM-printed samples (desktop scale) from 87 to 10 μm/mK in the printing direction while increasing the thermal conductivity from 0.177 to 0.397 W/mK in the printing direction [40]. Similarly, the addition of 13% carbon fiber almost tripled the tensile strength in the printing direction while increasing the elastic modulus more than four times. These changes explain the enabling nature of carbon fiber in an out-of-oven printing process.

The changes in the thermal expansion and thermal conductivity of carbon fiber reinforced polymer composites have been modeled as a function of the fiber volume fraction, as illustrated in Figure 8 [42]. If approximately 20 vol.% carbon fiber is added to a matrix, as is common in BAAM or commercially available filaments, the printed beads experience a substantial drop in thermal expansion compared with an unfilled polymer. This results in a significant reduction of residual stress buildup and the propensity for warping, and the evolution of stresses between the build plate and the part, as well as the stress between printed layers that would typically result in cracking as the part thickness increases. The improved thermal conductivity minimizes temperature gradients and helps the polymer achieve melting and cool upon deposition more quickly, improving the maximum print speeds and geometric tolerances. Also, the improved thermal conductivity helps minimize the temperature gradient between layers. Those factors, plus the dramatically improved stiffness, eliminates the distortion/warping of the printed part in an out-of-oven process.

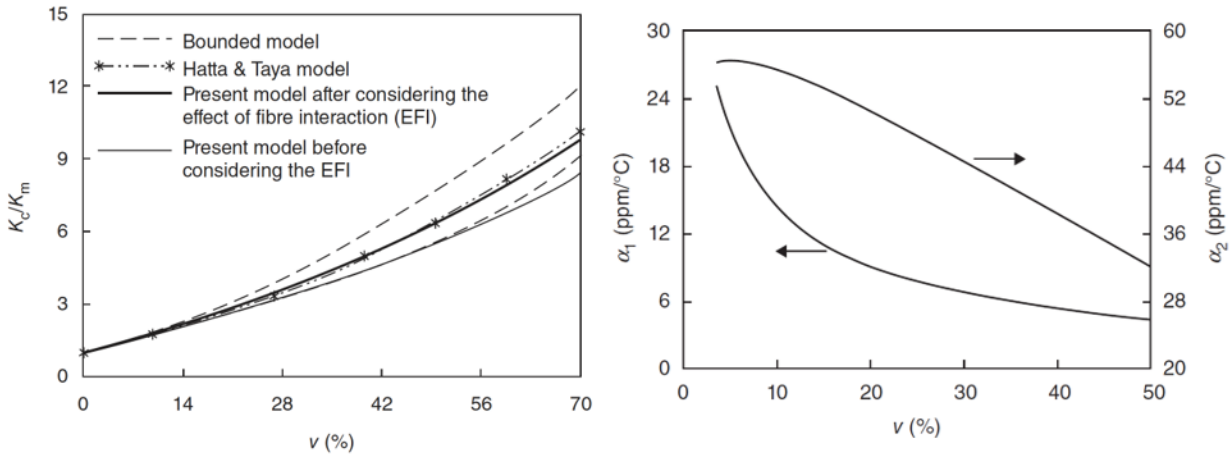

Figure 8. The thermal conductivity (Kc and Km are the thermal conductivities of the composite and polymer matrix, respectively) of a random 3D short fiber reinforced composite (left) and the thermal expansion of an aligned short fiber reinforced composite (right) with respect to fiber volume fraction (v) [42]; α_1 and α_2 are the CTEs parallel and perpendicular, respectively, to the fiber reinforcement.

As large-scale AM technology advances, new materials are being investigated that can offer diverse benefits for different applications. As mentioned previously, the rheological behavior of the feedstock material is crucial to a successful printing process and can be used to determine the optimum printing parameters. Ajinjeru et al. studied the rheological behavior of various thermoplastics from commodity to high-performance polymers and their fiber composites to assess their suitability for the BAAM process and their printing parameters. They studied ABS, polyphenylsulfones (PPSU/F), polyetherimide (PEI), PEKK, and PPS [26, 43, 44] and investigated how the viscoelastic properties of these polymers and their carbon fiber composites—such as viscosity, storage, and loss modulus—change with temperature, shear rate, and fiber content. Whereas ABS acted like an elastic solid, PPSU acted more like a viscous liquid [26, 44, 45]. The addition of carbon fiber (up to 35%) increased the shear thinning

behavior (2–3x) of both ABS and PPSU while increasing their viscosity four- to five-fold. Similar behavior was observed for PEI composites. While the viscosity of the resin decreased by 50% with an increase in temperature from 365 to 400 °C, the addition of 10 wt.% carbon fiber more than doubled the viscosity of the PEI resin [44]. The authors suggested a viscoelastic model to calculate the total pressure drop at the nozzle exit for selected extrusion temperatures based on rheology measurements and nozzle geometry to predict whether a material will extrude/print [26].

Although adding carbon fiber to a polymer feedstock minimizes residual stress accumulation, failure of prints due to warping and delamination is still a pressing concern. Careful selection of the printing parameters can help reduce the risk of failure due to distortion and delamination. Compton et al. studied the thermal profile during the printing of carbon fiber ABS feedstock in a BAAM machine and related the printing conditions to part distortion [8]. The one-dimensional thermal finite difference model they developed predicted layer temperatures for thin-wall printed structures that are in excellent agreement with experimental results. The model and experimental results showed that the temperature of the top layer must be kept above the glass transition temperature to prevent rapid cracking or delamination. It is interesting that the authors found that increasing the thermal conductivity of the feedstock had an adverse impact on the size of the part that can be printed without warping/delamination [8].

Although BAAM enables printing of a variety of short-fiber filled composites, high fiber loadings (up to 50%) and high throughput (up to 50kg/h) may lead to surface distortion of the extruded material during printing. This bead instability referred as “sharkskin,” is usually in the form of roughness and a dull surface finish; and it depends on the viscoelastic behavior of the material and printing conditions, such as temperature, shear rate, throughput, and nozzle

geometry [46]. Sharkskin formation/surface defects not only impact the surface finish and appearance of the printed parts but, more importantly, can significantly decrease the mechanical performance. Preliminary studies performed on carbon fiber–reinforced PEKK composites with a capillary rheometer showed that sharkskin did not form below high fiber loadings (~40%), and it formed at flows that are more elastic than viscous (G'>G'') [46].

As a final note, since a BAAM system uses feedstocks in pellet form, the feedstock material can be switched during printing, allowing printing of the part selectively with different materials. This approach enables the design and manufacture of components with localized mechanical performance based on requirements and allows for cost and weight savings. Sudbury et al. studied the application of functionally graded materials (FGMs) on large-scale AM systems [47]. In the FGM approach, a lower-cost material with suboptimal mechanical performance is used in most of the part, and a higher-cost, higher-performance material is used in selected areas based on requirements. In these studies, transitions among the neat, fiberglass–reinforced, and carbon fiber–reinforced ABS were studied in a BAAM system extruder to understand the behavior of the system, and shape functions were created based on thermogravimetric analyses [47].

2.2.4 Direct Write

In the direct write (DW) approach, a syringe head and a dispenser are used together to additively deposit a liquid or a slurry on a surface (Figure 7). This technology has been used for printing biomaterials, conductive inks, and other materials [48-50]. Usually, a photo-curable polymer is injected and cured in-situ using ultraviolet (UV) light or a laser. The light is attached to the syringe nozzle, allowing instantaneous curing of the DW material. Alternatively, if a polymer

(e.g., a resin) is modified via additives to become sufficiently viscous to hold its shape during printing, it can be printed using DW and subsequently cured. For example, the viscosity of a fiber-reinforced thermosetting resin can be tuned via the addition of high-surface-area nanomaterials. This slurry is then printed and cured in-situ or post-cured via exposure to high temperatures or UV light.

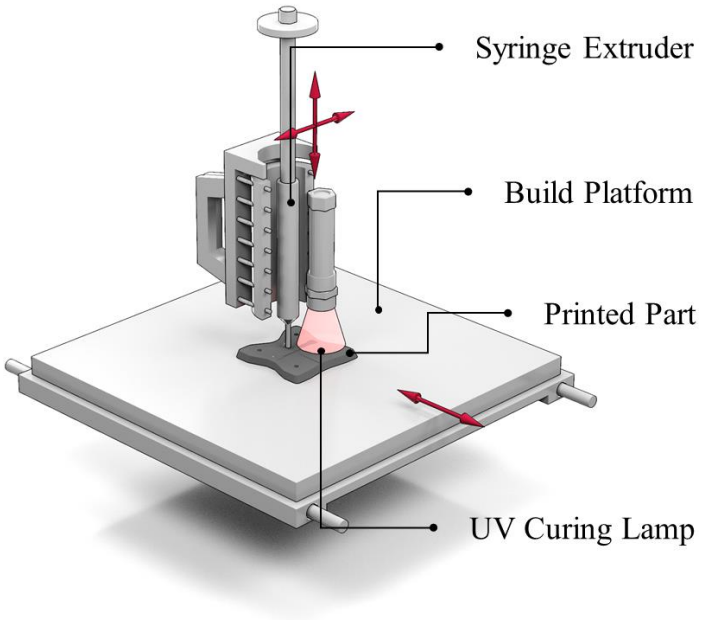

Figure 9. Representative schematic of a direct write 3D printer.

An acrylic-based photocurable resin was combined with a thermally curable epoxy resin to form a polymer matrix [51]. A syringe extruder equipped with a UV torch was used to extrude and cure the polymer. After the ratio of the polymers was tuned, 5 and 30 wt.% carbon fibers were added to create DW printable composites. The addition of carbon fiber increased the storage modulus from 3.0 GPa to 3.8 GPa and 7.7 GPa, respectively, for 5 and 30% fiber loading. The glass transition temperature of the composite changed from 115 °C for unfilled to 139 and 76 °C, respectively, for the 5 and 30% carbon fiber filled samples [51]. Building off this work, fumed silica was added as a thixotropic agent to induce shear thinning in the resin mixture, and 5 wt.%

carbon or glass fibers were added as reinforcement. The thermomechanical properties and microstructures of the printed parts were investigated. The storage modulus increased from 3.15 GPa to 4.30 GPa and 5.18 GPa, respectively, for the glass and carbon fiber fillers. The composite properties were predicted with a Halpin-Tsai model, achieving moduli of 4.65 and 5.58 GPa, respectively, for the glass and carbon fiber fillers. These composites achieved maximum tensile strengths and moduli of 41.7 MPa and 3.5 GPa, respectively, for carbon filler and of 33.8 MPa and 4.4 GPa, respectively, for glass filler. An airfoil and a propeller were printed to demonstrate the print quality [52]. The DW technology with carbon fiber filled resins has the potential to print high performance parts from thermosetting resins for various applications.

2.2.5 Stereolithography

AM using thermosetting resins can also be accomplished using stereolithography (SLA), also referred to as optical fabrication, photo-solidification, or resin printing (Figure 8). In this case, a thermally or UV-curable resin is typically added to a bin. Light, heat, and oxygen can be controlled to cure a layer of the resin to a print surface. The print surface moves to allow new layers to be cured and added to the part. Layer heights of well under 50 μm have been reported under ideal conditions using this technology [53].

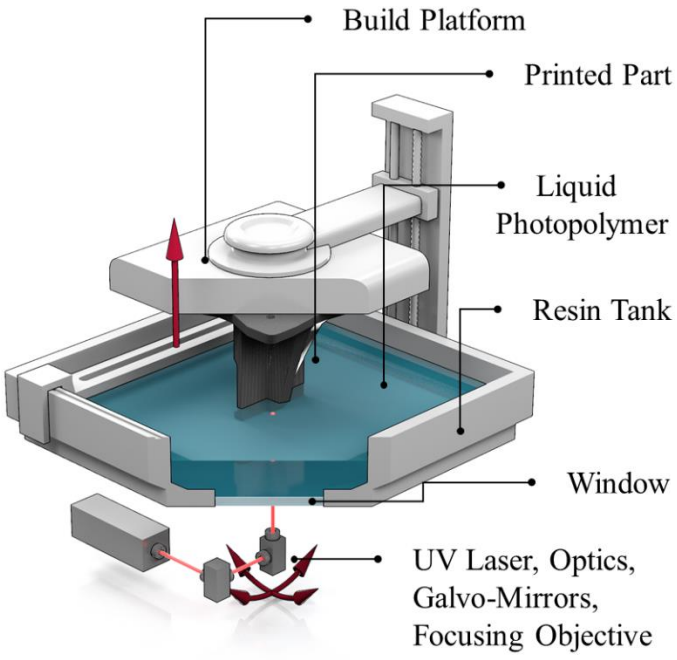

Figure 10. Schematic of a typical stereolithography 3D printer.

Nonwoven mats of E-glass, carbon fiber, and Para Aramid fibers were used to make composite parts using SLA with photocurable resins (acrylic based and epoxy based) [54]. The highest strength and modulus were found for E-glass fiber reinforcement and acrylic-based resin. The addition of glass fibers to this composite increased the strength and stiffness of the material by 48.8% and 32.1%, respectively. At a fiber mat areal density of 17 gsm (grams per m^2), the tensile strength, and modulus of this composite were 55.2 MPa and 2.51 GPa, respectively. Interestingly, the addition of glass fibers led to a decrease in the strength and modulus of the epoxy-based composites, with a larger areal density leading to a larger decrease in mechanical properties [54]. Published research on SLA carbon fiber polymer is limited, mostly because of the difficulty in printing parts out of a fiber-filled bath. Optical properties of the resin bath are affected by the addition of fibers, and improvements in properties from fiber addition might be minimal because only very short fibers can be used with this approach.

2.2.6 Selective Laser Sintering

Selective laser sintering (SLS) typically involves using a laser on a bed of powdered material to selectively fuse powder particles together, creating a consolidated layer (Figure 11). Once one layer is fused, the bed moves down, and a single-layer thickness of powder is added to the top of the part. This layer is selectively sintered in the same manner, and the process continues in a layer-by-layer fashion.

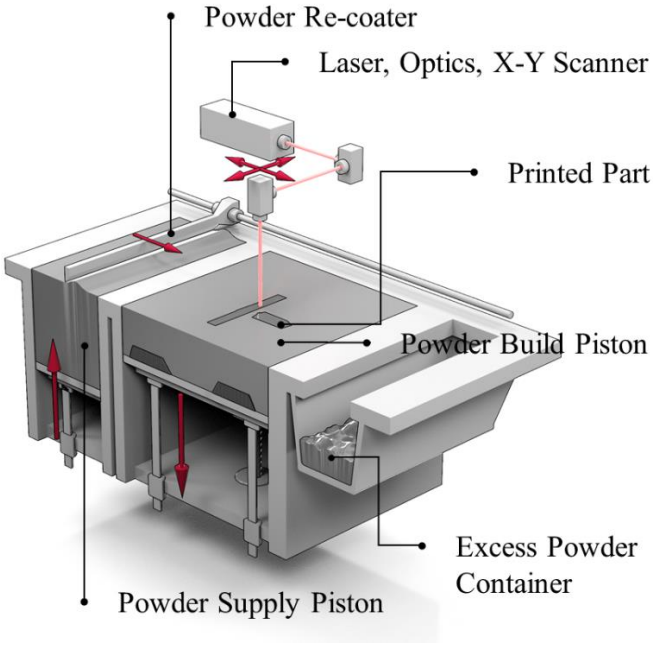

Figure 11. Schematic of typical selective layer sintering 3D printer assembly.

The addition of carbon nanofibers to SLS-printed polyamide-12 (PA12) parts has been investigated [55]. Carbon nanofibers with diameters of 60–150 nm and lengths of 30–100 μm were added to PA12 using melt mixing, and the composite was cryogenically fractured to produce powders with an average diameter of 50 μm. The addition of 3 wt.% nanofibers resulted

in a 22% increase in storage modulus in 3D printed coupons, although the powder preparation method resulted in a rough surface finish. Further work is necessary to produce fiber-reinforced powders more suitable for SLS manufacturing. [55]

Carbon fiber reinforced PA12 composites were manufactured using SLS, and their microstructure and mechanical and thermal properties were investigated [56]. The addition of 30, 40, and 50 wt.% of carbon fiber resulted in increases in flexural strength of 44.5, 83.3 and 114%, respectively, and increases in flexural modulus of 93.5, 129.4, and 243.4%, respectively, compared with unfilled PA12 sintered parts [56]. SEM was used to observe the fracture features for these composite samples. Fibers covered with the nylon matrix were observed, indicating a high interfacial shear strength. Parts were manufactured with walls as thin as 0.6 mm with 30 wt.% carbon fibers [56]. In a similar study, carbon fibers were used to reinforce PA12 powders and coupons were manufactured from this powder via SLS [57]. The tensile properties and structures of parts printed in a variety of orientations were investigated. Significant voids were observed, particularly between layers of the print, which significantly compromise the mechanical properties of the composite. The printed parts had an average internal porosity of 11.8 to 15.9%, depending on the print orientation. The addition of carbon fiber to the PA12 resulted in increases of up to 28 and 73%, respectively, in the strength and modulus of the plastic, although the strain-to-failure was reduced by 80% compared with unfilled PA12. The fiber volume fractions were not reported in this study [57].

Carbon fibers interact weakly with nylon unless their surfaces are specially altered. The surfaces of carbon fibers were modified with nitric acid to increase the interfacial adhesion between the fiber and nylon matrix in SLS powders. Although the treatment increased the surface oxygen concentration and introduced additional roughness to the fiber surface, increasing the mechanical

interlocking, the oxygen functional groups decomposed at the sintering temperature to result in substantial porosity of up to 38%. To mitigate this, the acid-treated fibers were heated to 400 °C in a nitrogen environment before the composite powder was created. This approach resulted in a decrease in the sample porosity and an increase in the tensile strength and modulus of 11 and 5%, respectively [58].

Carbon nanotubes have also been investigated as a filler in PA12 SLS composites. The addition of 0.5 wt.% carbon nanotubes increased the strength and modulus of printed SLS nanocomposites by 10 and 12%, respectively, over unfilled SLS printed PA12 [59]. The addition of 1 wt.% nanotubes was found to increase the electrical conductivity of SLS-manufactured PA12 composites by several orders of magnitude, from the order of 10^{-12} to 10^{-5} S/cm under DC voltage conditions, although only modest improvements in thermal conductivity were observed [60]. It was also observed that the addition of nanotubes could increase the storage and loss moduli of SLS PA12 parts, although an increase in material viscosity was also observed [61]

Although SLS is one of the more mature and fastest-growing AM technologies, it has attracted little attention from the AM composites research community. For SLS composite printing, fibers are introduced into the polymer and then pulverized to create a powder. The process results in fiber lengths on the order of 20 microns, which offer only modest improvements and have a negative influence on the part quality. The addition of carbon fibers, nanofibers, and nanostructures can potentially improve the properties of SLS-printed parts. To this end, a better understanding of the effects of carbon addition on the sintering, microstructures, and mechanical properties of SLS carbon fiber–reinforced composites is required.

2.2.7 Modeling Tensile Properties of Short Fiber–Reinforced AM Composites

Short-fiber composites have developed significant momentum in research, commercial, and industrial settings as a result of the many benefits that they offer. In general, the use of short carbon fibers tends to improve properties without significantly increasing the material cost or altering the manufacturing method. Some AM methods also offer the benefit of selectively aligning the fibers within the composite, which can be used to advantage by part designers and engineers. Carbon fibers also help to reduce the thermal expansion of the material compared with neat polymers, which is useful in reducing warping when part sizes are scaled up in FDM. Short fiber reinforced composites offer the most accessible pathway toward scalable, affordable, and functional AM composites.

As with conventionally manufactured short-fiber composites, however, the maximum mechanical properties achievable with short-fiber composites are severely limited compared with the use of their continuous-fiber counterparts. For example, the critical length of a carbon fiber in an ABS matrix has been calculated as approximately 640 μm, whereas the large majority of fibers used in AM composites fall below 150 μm in length [62]. Additionally, it is commonly observed that adding fiber fillers can increase the AM composite void fraction. These two factors create a low ceiling for the maximum achievable mechanical properties of fiber-reinforced AM composites using current technology. Therefore, it is also necessary to consider the place of continuous fiber reinforced composites in the composites industry in the future.

A theoretical framework for predicting the mechanical properties of CFRPs based on the composite fiber length distribution (FLD) and fiber orientation distribution (FOD) can be realized using the Halpin-Tsai model, which was expanded upon by Fu and Lauke [42, 63]. Such a model can be used prescriptively to understand the primary limiting factors of composite

performance and the most effective methods of improving mechanical properties [64]. The model is based on the modified rule of mixtures, as seen in Eq. (1), where σ_c is the ultimate tensile strength of composite, σ_f is the ultimate fiber strength, σ_M is the matrix stress at composite failure strain, ν_f is the fiber volume fraction, ν_m is the matrix volume fraction, and $\chi_1\chi_2$ is known as the fiber efficiency factor [63].

$$\sigma_c = \chi_1\chi_2\sigma_f\nu_f + \sigma_M\nu_m \tag{1}$$

The fiber efficiency factor is a function of the FOD, $g(\theta)$, and FLD, $f(l)$, of the composite, as seen in Eq. (2). In this equation, l is the fiber length, θ is the fiber orientation, l_{mean} is the average fiber length, l_c is the critical fiber length, μ is the snubbing friction coefficient, A_f is a constant, and $l_{c\theta}$ is the critical length for an obliquely crossed fiber [63].

$$\begin{aligned}\chi_1\chi_2 = &\int_{\theta_{min}}^{\theta_{max}}\int_{l_{min}}^{l_{c\theta}} f(l)g(\theta)(l/l_{mean})(l/2l_c))\exp(\mu\theta)\mathrm{d}/\mathrm{d}\theta \\ &+ \int_{\theta_{min}}^{\theta_{max}}\int_{l_{c\theta}}^{l_{max}} f(l)g(\theta)(l\backslash l_{mean})(1 - A_f\tan(\theta)) \\ &\times (1 - l_c(1 - A_f\tan(\theta))/(2l\exp(\mu\theta)))d/d\theta\end{aligned} \tag{2}$$

The elastic modulus of a short-fiber composite can be calculated using a laminate analogy approach [65]. In this approach, the fiber reinforcement is approximated as multiple laminae of various orientations and lengths. The laminate stiffness matrix, A, is found from the fiber length and orientation distributions, along with the off-axis stress-strain matrix, Q', using Eq. (3). The laminate stiffness matrix is then used to find the composite tensile modulus using Eq. (4).

$$\bar{A}_{ij} = \int_{l_{min}}^{l_{max}}\int_{\theta_{min}}^{\theta_{max}} \frac{Q'_{ij}f(l)g(\theta)d}{d\theta} \tag{3}$$

$$\bar{E}_{11} = \frac{\bar{A}_{11}\bar{A}_{22} - \bar{A}_{12}^2}{\bar{A}_{22}} \tag{4}$$

This model was validated using the experimental results from Tekinalp et al. [23]. In this study, short carbon fiber reinforced ABS composites were manufactured using either CM or FDM printing. Composites with 0, 10, 20, 30, and 40 wt.% carbon fiber were manufactured, and the FLD and FOD for each sample were found. Analytical curves were fit to the experimental length distributions, and the tensile properties were found for the weakly aligned CM samples. The predicted properties and experimental results are shown in Figure 12. There is a good agreement between the experiments and modeling.

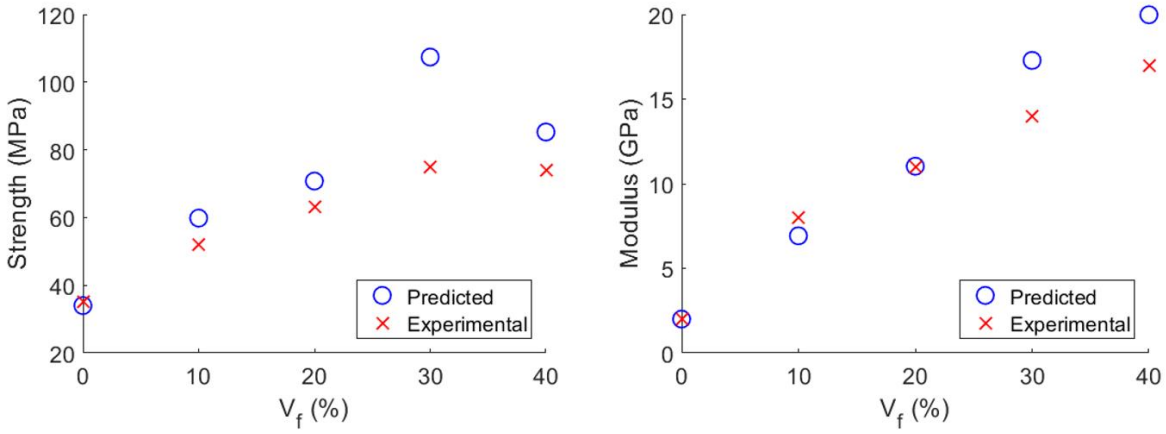

Figure 12. Validation and calibration of the theoretical model against experimental results for short-fiber composite strength (left) and modulus (right).

The validated model was used to predict the tensile properties of AM short-fiber composites. Tensile properties as a function of fiber aspect ratio are shown in Figure 13, which shows that both strength and modulus values were normalized by the predicted properties for composites with perfectly aligned and infinitely long fibers. Fibers were assumed to be mostly aligned, and two critical fiber lengths were used to capture the reinforcement effect in a typical thermosetting

(l_c of 0.3 mm) and thermoplastic (l_c of 3 mm) composite. Note that the critical fiber length does not affect modulus values. The results clearly show that for a greater than 80% translation of properties in AM thermoplastic composite, fibers with aspect ratios of 1000 or longer should be used. For carbon fibers with diameters of 5–7 μm, this translates to a fiber mean length of 5–7 mm. The model used here does not account for fiber end effects and therefore overestimates strength. It can be concluded that fibers that are 1 cm or longer can enable high-performance AM composites. This length is two orders of magnitude longer than what is achievable via the current approaches for short-fiber polymer mixing and AM. AM with continuous fibers offers a viable but more costly solution.

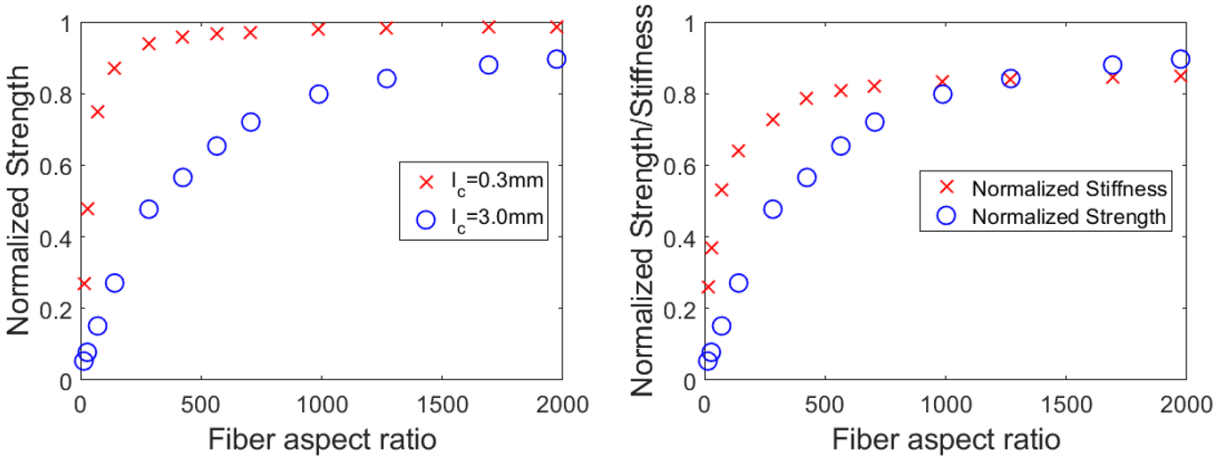

Figure 13. Influence of fiber aspect ratio on AM composite tensile strength for two critical lengths (left) and on tensile strength (l_c =3mm) and Young's modulus (right).

2.3 Additive Manufacturing of Continuous-Fiber Reinforced Plastics

Most continuous-carbon fiber composites are created with FDM technology, although other novel techniques are being investigated. The fibers can either be incorporated through coaxial extrusion to create composite filaments suitable for printing with commercial FDM printers or by injection of the fiber strands and polymer filaments into the printer hot end simultaneously

during the printing process. As with short-fiber composites, additively manufactured continuous-fiber composites tend to have higher void contents than their conventionally manufactured counterparts, as can be seen in Figure 14. The mechanical property limits achievable using continuous fibers are much higher than the properties obtainable in short-fiber composites, as the fiber lengths are much greater than the critical lengths of the fiber-polymer system, and higher volume fractions can be more easily achieved.

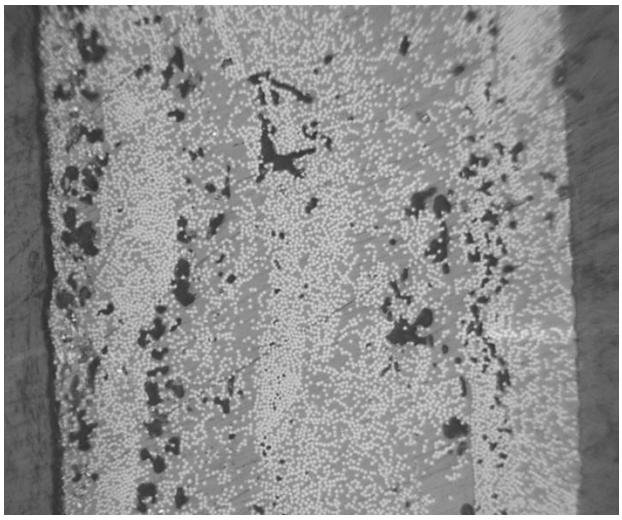

Figure 14. Optical micrograph of AM continuous carbon fiber reinforced PEEK composite cross-section with approximately 43 vol% reinforcement. Light contrast regions are fibers, gray regions are polymer matrix, and dark contrast regions are voids.

Initial attempts at manufacturing continuous ABS glass fiber composites using FDM were made in 2001 by Zhong et al [66]. The maturation of FDM technology over the following decade greatly increased the feasibility of manufacturing continuous-fiber composites with this layer-by-layer process. Specifically, there has been significant progress in this effort since 2014 due to the commercialization of continuous-fiber 3D printers. This field is still in its infancy, and most studies are proof-of-concept or basic investigation of properties and structures. There are only a

few studies revolving around the application and design of AM continuous-fiber composites [67, 68].

Continuous-carbon fiber composites were printed on a Mark One with various carbon fiber contents [69]. The authors investigated potential defects present in sliced parts, volume fractions of the carbon fiber filaments (34.5%), void contents present in printed parts, and part failures. Samples printed with a total of eight nylon layers and two carbon fiber layers were found to have strengths close to that predicted by the rule of mixtures (~140 MPa), whereas samples containing a total of four nylon layers and six carbon fiber layers were further from the rule of mixtures prediction (~460 MPa). This result is thought to be due to an increase in void content with increasing carbon fiber content [69]. An average stiffness (VAS) method was used to model the mechanical properties of glass fiber reinforced nylon composites printed on a Mark One 3D printer [70]. The experimentally determined tensile moduli at fiber volume fractions of 4.04, 8.08, and 10.1% were 1.767, 6.92, and 9.00 GPa, respectively. The model estimated these values to be 4.16, 7.38, and 8.99 GPa (differences of 57.2, 6.2, and 0.1% from the measured values, respectively). The microstructure and failure characteristics of the composites were also investigated in this study [70].

There are several publications around the in-nozzle impregnation of continuous fibers with PLA. PLA-based carbon and jute fiber (natural biodegradable material) continuous-fiber composites were printed using FDM and a method of in-nozzle impregnation [71]. The volume fractions of the carbon and jute fibers in the composites were 6.6 and 6.1%, respectively. The strength and stiffness of the carbon fiber composite were 185.2 MPa and 19.5 GPa, respectively, an increase of 435 and 599%, respectively, compared with the PLA [71]. In another study, continuous carbon fibers were impregnated with PLA in the nozzle of an FDM printer to produce composite

parts [72]. The effects of extruder temperature, layer thickness, feed rate of filament, hatch spacing, and printing speed on print quality were examined. The microstructure and failure characteristics were also investigated. The maximum carbon fiber content achieved was 27%, and the composite displayed an average flexural strength and modulus of 335 MPa and 30 GPa, respectively. The flexural strength of the composite could be controlled by adjusting the printing parameters. Simple geometries, such as a thin-wall cylinder and an airfoil, were printed to demonstrate printer capabilities and part quality. In a follow on study, the composites were also recycled to recover 100% of the carbon fibers and 73% of the PLA matrix [73]. No degradation of the carbon fiber properties was observed, and remanufactured composites displayed a slight increase in mechanical properties over their virgin fiber counterparts.

In a third study, carbon fiber-PLA composites were manufactured using FDM by in-nozzle fiber impregnation of PLA [74]. The effect of surface treatment of the carbon fibers prior to printing was investigated. The microstructure, mechanical, and thermo-elastic properties of the composite were examined. The composites contained roughly 34% carbon fiber. The tensile strengths of PLA, fiber-reinforced PLA, and surface-modified carbon fiber–reinforced PLA were found to be 28, 53, and 80 MPa, respectively, with flexural strengths of 59, 91, and 156 MPa, respectively. The storage modulus was also substantially improved by modifying the fiber surface. Also, the addition of carbon fiber resulted in a modest increase in the glass transition temperature. [74] A fourth study investigated in-nozzle impregnation combining continuous carbon fiber and PLA to print composites with between 42.32 and 51.92% fiber volume fractions using an FDM-based approach [74]. Interestingly, the structures printed were 3-dimensional, out-of-plane lattice truss core structures. The path generation and optimization were discussed, and the microstructures and compressive behavior of the lattice truss-core sandwich samples were studied [75].

Apart from in-nozzle impregnation, continuous-carbon fiber reinforced PLA filaments were manufactured using a coaxial extrusion mold. The filaments were then used to print simple part geometries, and the flexural modulus and strength were measured [67]. A response surface methodology was used to observe the relationship between various processing parameters and the resulting material properties. The maximum flexural strength and modulus achieved were 610.1 MPa and 40.1 GPa, respectively. It was concluded that, in general, low layer thickness and low printing speeds resulted in the highest flexural strength. [67]

Continuous E-glass/polypropylene filaments were manufactured using a pultrusion technique. Comingled glass and polypropylene fibers were pulled through a heated nozzle to create printable filaments v. A Prusa i3 was modified to accommodate the filament, equipped with a fiber cutting mechanism. The microstructure of the filament was examined, and the effect of printing parameters on voids and composite flexural modulus was analyzed. The properties observed were lower than predicted—only 48% of the theoretical maximum; assumed to be due to the voids in the filaments. Although a void content of up to 20% was measured, the composite displayed an increase in flexural modulus of 800% over neat polypropylene samples [76].

A polycaprolactone continuous–carbon fiber composite was created by creating a coaxial-fiber composite used in an FDM printer [77]. Rather than investigating microstructure or properties, this work demonstrates a proof-of-concept of multi-planar printing with continuous–carbon fiber composites. Although only thin specimens were printed, the authors were able to achieve a multi-planar print on a curved substrate with their co-axial filaments [77].

In a recent study, a framework for failure analysis of AM continuous-fiber parts was developed and validated [68]. The difficulty in the modeling and design of such parts lies in capturing the curvatures in fiber-reinforced filaments. To this end, material properties for each element in a

finite element model should be assigned based on the local direction of the printed filaments. A script was developed to automatically achieve a proper model of parts with curved continuous filaments, and good agreement between the experiments and simulations was shown [68]. Suggestions for the design of parts based on continuous fibers were also given in this study.

2.3.1 Alternative and Hybrid Methods

In an attempt to reinforced 3D printed ABS, the bottom half of a tensile coupon was printed, a strand of carbon fibers was placed on the printed ABS, and the second half of the coupon was printed over this assembly [78]. To allow polymer diffusion, the composite was heat treated after printing. This thermal bonding led to a roughly 2x increase in the strength of the composite. To increase the composite strength further, three layers of the composite were also printed, following the same approach, with continuous fiber-filled ABS filament, leading to a further increase in both strength and ductility [78]. In another study, continuous carbon fibers were added to a single layer of FDM-printed ABS tensile coupons using three methods, and the mechanical properties of the resulting composite were investigated [79]. In one method, the fibers were added on the part and were infused by directly printing over them. In a second method, the fibers were injected through a heated hypodermic needle so that they were placed onto a molten portion of the previous ABS layer. As the volume fraction was very low, the addition of carbon fibers did not contribute to an increase in composite strength. The addition of carbon and glass fibers increased the stiffness of the composite by up to 40 and 80% of the rule of mixtures prediction, respectively [79].

A hybrid approach combining 3D printing and conventional manufacturing was used to fabricate a pulley housing, a hook, and a universal joint from a composite reinforced with continuous

carbon fibers [80]. Each part was modeled, constraints were enforced, and the internal stresses were observed. The part geometry was then optimized with respect to the properties of the continuous–carbon fiber reinforcement. This optimized geometry was then used to inform changes to the original computer-aided design of the part, and internal channels were created for carbon fiber placement. The molds were then printed in PLA, ABS, or Nylon 12. Continuous–carbon fiber tows, Kevlar, or Basalt fibers were then laced through the internal channels and held in place with cyanoacrylate glue. A low-viscosity epoxy was then applied to infiltrate the fibers and cured, and the finished parts were tested. The carbon fiber reinforcement displayed the largest improvement in mechanical performance, however, as no tensile coupons were tested, no material properties were explicitly determined. Although substantial improvements were observed, this technique cannot currently be automated and is labor-intensive to perform [80].

Pre-impregnated carbon fiber tows were fabricated and placed on partially printed PLA tensile coupon molds, and the print was completed to embed the prepreg fibers into the PLA parts [81]. Neat PLA -3K, 6K, and 12K tows- was used in this experiment, and the mechanical and electrical properties of the composites were characterized. This experiment aimed to strengthen the composites and provide a tool for structural health monitoring through electrical resistance measurements. The composites were printed with 20% PLA infill and showed an increase in tensile strength from 19.2 MPa to up to 32.6 MPa; however, 100% PLA was found to have a strength of 46.4 MPa. The change in resistance as a function of tensile or flexural strain was also observed. This technique was used to embed carbon fibers into the five fingers of a 3D printed hand to demonstrate a potential application of this technology [81].

A thermosetting matrix was used to fabricate continuous carbon fiber composites using a nozzle-based approach. The fibers were fed through a resin bath and deposited from a 2 mm nozzle onto

the print surface in 1 mm thick layers. The parts were cured in a heated environment after printing. The rotational axes were also controlled, allowing for fibers to be deposited around a cylindrical substrate. The tensile strengths and moduli of the composites were 792.8 MPa and 161.4 GPa, respectively. The flexural strengths and moduli were 202.0 MPa and 143.9 GPa, respectively [82].

2.3.2 Commercial Systems for Continuous-Fiber AM

Short carbon fiber-filled PLA, ABS, nylon, PETG, PC, PEEK, and ULTEM filaments are widely manufactured, accessible, and printable using commercial desktop 3D printers. Markforged and Anisoprint LLC [83] are currently the only manufacturers of a commercially available 3D printer for continuous fiber reinforced materials. A Markforged FDM printer can print with nylon, short carbon fiber–filled nylon, and a continuous fiber-filled nylon. The continuous-fiber reinforcements, approximately 35% volume fraction [68], can be carbon, glass, or Kevlar [69, 84]. The mechanical properties and microstructures of these filaments and printed parts have been investigated by the authors and other groups [85-87]. Their continuous carbon fiber–reinforced parts exhibit tensile strength and stiffness of ~700 MPa and 52 GPa, respectively. Anisoprint LCC reports similar mechanical properties [27]. Such properties are impressive compared with neat polymers; however, they are much inferior to those of conventional carbon fiber composites.

Several startup companies involved in carbon fiber composite 3D printing have formed during the past few years. Each company offers a different value proposition, such as an improved rate of manufacturing, enhanced mechanical performance, or complex object printing. Impossible

Objects have developed a novel composite-based AM technique. This process involves depositing a polymer on individual carbon fiber mats by wetting the mats using thermal inject technology and then applying a polymer powder to bind to the wet surface. The mats are then stacked, compressed, and heat treated to fuse the layers. The excess material is removed with a sandblaster to reveal the part geometry. This technology can produce parts at relatively fast rates and with strengths greater than 130 MPa for use in functional applications. [88]

Other major players in this field are Arevo Inc. [89] and Mantis Composites [90], both with 5-axis robotic arms that can print carbon fiber-reinforced polymers [91, 92]. Whereas Arevo focuses on printing large parts using an approach similar to automated tape placement (ATP), Mantis targets the market for smaller but complex-shape structures. 3D Fortify [93] and Anisoprint are two other startup companies in the area of continuous–carbon fiber composite 3D printing. While all these companies use thermoplastics as a matrix, Continuous Composites [94] and Moi Composites [95] use thermosetting resins and out-of-autoclave curing to fabricate continuous fiber–reinforced parts. There is not much data available from these companies on the mechanical properties of their printed parts. However, Arevo has published results for its 50% carbon fiber-filled PEEK, showing tensile strength and modulus in the fiber direction exceeding 1400 MPa and 110 GPa, respectively [96].

As shown in Figure 4 and discussed earlier, mechanical property improvements for materials using short carbon fibers typically are not substantial. However, carbon fiber additions improve properties dramatically and reduce warping for large objects. AM with continuous fiber–reinforced plastics can potentially open new avenues for designing and manufacturing parts with superior mechanical properties. The potential for producing parts with metal strength and stiffness using continuous-fiber reinforcement could drive the adoption of this technology in

years to come. The integration of design optimization with such a manufacturing technology can facilitate their entry into markets where load-bearing functionality is crucial.

2.4 Applications and Opportunities in Carbon Fiber Additive Manufacturing

We highlight only some of the promising applications for AM carbon fiber composites in this paper. The manufacturing process and the mechanical properties of the AM composites make them attractive to several industries, including aerospace, automotive, and energy. Tools and fixtures made by 3D printed composites can outperform machined parts in terms of both performance and cost. Carbon fibers can improve the mechanical and thermal properties of printed parts and potentially enable their use as molds for polymer-based part manufacturing.

2.4.1 Aerospace and Multi-Material 3D Printing

Many researchers have explored AM concepts for aerospace applications. Most initial efforts focused on single material systems or alloys of aluminum, titanium, or thermoplastics to produce simple, nonstructural components such as brackets, enclosures, and fixturing [97, 98]. Examples include eight 3D printed titanium waveguide brackets on the National Aeronautics and Space Administration (NASA) Juno spacecraft, aluminum brackets on the Telstar 18 Vantage communication satellite, and thermal blanket retention brackets on Boeing 702MP satellites [97-99]. As process quality and confidence improved, additively manufactured components have been used as structural and high-performance parts in jet engines, rocket engines, and spacecraft structures from initial assembly to maintenance and repair [99-101]. Today, AM is being used to produce large portions of high-performance systems including aircraft, unmanned aerial vehicles (UAVs), and launch vehicles [102-104]. For example, NASA has demonstrated an 80% part count reduction using AM to produce rocket engines, and Aerojet Rocketdyne has demonstrated

a fully 3D printed rocket engine that combines dozens of traditionally manufactured parts into three parts using AM [105, 106].

The majority of these examples are based on metal AM processes using alloys of aluminum and titanium. The use of thermoplastics has largely been limited to nonstructural or low-performance aerospace applications because the material properties generally do not meet the demanding requirements for aerospace systems. However, additively manufactured CFRPs have the potential to dramatically improve the structural performance and thus improve the utility of polymer-based AM components.

Many of the advantages of AM CFRPs over AM metal are similar to those for traditional manufacturing processes, i.e., lower mass and higher strength-to-weight and stiffness-to-weight ratios. However, AM CFRPs have two additional advantages over AM metals. The first is lower cost, which enables future concepts of drone swarms and disposable UAVs in addition to traditional life-cycle cost savings [107-109]. The second is lower processing temperatures compatible with a wider array of AM processes, which enables multi-material AM for multi-functional components [110, 111]. Multi-functional AM has the potential to be a game-changer for aerospace systems. Structures with integrated electronics, sensors, or antennas will provide mass savings, life-cycle cost savings, and performance improvements for aircraft, UAVs, and space systems that cannot be achieved with traditional manufacturing approaches.

Finally, additively manufactured CFRPs have the potential to dramatically change how we use the space environment. NASA and Made In Space have demonstrated the ability to 3D print thermoplastic parts in a microgravity environment on the International Space Station [112, 113]. While this has many potential applications for manned space exploration, it is the tip of the iceberg for potential applications in on-orbit manufacturing. The drawback of the Made In Space

system is the use of single-material, thermoplastic parts that have the same poor mechanical properties as terrestrial AM thermoplastics. This limits the application of on-orbit AM because most on-orbit structural requirements are driven by strength and stiffness to minimize structural dynamics that affect the precision of the structure. The improved performance of AM CFRPs has the potential to enable on-orbit manufacturing of large space structures, including antennas, reflectors, solar arrays, and space stations, for a wide range of applications. NASA is actively pursuing on-orbit manufacturing concepts through its in-space assembly tipping point technologies effort [114].

2.4.2 Big Area Additive Manufacturing

ORNL and Cincinnati Inc. have demonstrated the potential for industrial-scale, functional, additively manufactured polymer matrix composites with BAAM technology. Many challenges must be overcome in scaling FDM from desktop to commercial or industrial applications. Specifically, temperature gradients can result in internal thermal stresses, which may result in part warping or inter-layer cracking. These effects become increasingly problematic as the length of the part increases, and it becomes essential to understand the underlying mechanisms thoroughly and develop reliable methods to mitigate warping and cracking. Compton et al. performed a thermal study of carbon fiber composite ABS parts printed with a 7.6 mm nozzle using BAAM [8]. It was found that for relatively thin-wall structures, printing onto a layer well above the glass transition temperature of the material would result in a part with minimal warping. As the layer just below the printing layer approached or dropped below the T_g of the polymer, substantial warping and cracking were observed in the parts. Therefore, for a given set of printing parameters, the largest feasible part can be found by determining the cooling rate of

the top layer. This part size can be increased effectively by increasing the ambient temperature of the print environment.

Although both the systems and the feedstock materials for large-scale AM continue to improve, its use in many industrial applications has already been demonstrated. While some of these demonstrations were to show what a system is capable of, others were targeting direct use in industry. Because AM is a freeform fabrication method operating directly from CAD, it does not require any molding or tooling and does not have the material waste typical for conventional subtractive manufacturing methods. For simple parts that need to be produced in industrially large quantities, conventional techniques can be faster and cheaper options; but large-scale polymer AM will be disruptively advantageous over other manufacturing techniques for the custom components and the complex geometries that require lengthy post-processing that is costly and time-consuming.

ORNL partnered with Local Motors and Cincinnati Inc. to demonstrate the utilization of BAAM for the rapid manufacture of customized electric vehicles and the world's first 3D printed car. The whole process involved the manufacture of a single automobile body/frame via a BAAM system and the integration of a handful of conventional components (battery, electric motor, steering column, wheels, and brakes) on the printed platform [115]. The AM of the car—a Strati weighing over 450 kg—in 44 h was demonstrated at the International Manufacturing Technology Show in Chicago in September 2014. The printed body was machined in less than 12 h and fully assembled in less than 24 h [115]. ORNL worked with AlphaStar Corporation to develop a numerical simulation methodology based on finite element method analysis, multiscale damage mechanics, and fracture mechanics. The methodology was developed to simulate the BAAM process to determine product quality in terms of distortions, material damage, and interface

fracture due to manufacturing. It was demonstrated on the production of the Strati [116]. In subsequent case studies, ORNL showed the bridging of the powertrain-in-the-loop development process with vehicle systems implementation using BAAM, and then printed a replica of a Shelby Cobra and a range-extended electric vehicle. [44, 45]

Molding and tooling is another area in which AM can offer dramatic benefits over traditional approaches. The manufacturing of tooling for large, contoured surfaces for fiber-layup applications is a costly process with long lead time. It requires understanding the geometry and the subtractive manufacture of the tool. The traditional approach to manufacturing tooling for the auto industry uses hand-sculpted clay; and in the marine pleasure craft industry, the exterior of a model is formed from either a hand-cut or machined foam layup to achieve smooth lines [117]. For the demonstration of the tooling application, ORNL and Magnum Venus Products additively manufactured a mold tool for a legacy whitewater adventure craft. A craft was first scanned to generate a CAD model for the mold, and then the mold was printed via a BAAM system and machined to achieve smooth and accurate dimensions. Hassen et al. demonstrated the manufacture of a vacuum-assisted resin transfer molding (VARTM) tool with dimensions of 0.965 × 0.559 × 0.152 m, using a carbon–reinforced ABS feedstock via a BAAM system [118]. The printed tool was spray coated and finished with a traditional tooling gel. The use of the mold was demonstrated to fabricate carbon fiber–reinforced Elium thermoplastic composites; and after the fabrication of ten parts in an out-of-oven VARTM process, the distortion in the mold was negligible [H14]. The coating used was developed by TruDesign. In another study, ORNL worked with TruDesign to develop low- and high-temperature autoclave tool coatings and demonstrated the use of 3D printed molds in an autoclave process for the first time [H16]. While mainly the manufacture of molds that can fit into BAAM systems was demonstrated, in a recent

study by ORNL with TPI Composites, a mold for a wind turbine blade mold was printed via BAAM. The mold was printed in 16 sections and was 13 m long. It also had heating channels integrated into the design and was mounted into a steel frame after fabrication [H28-29]. In another study, Sudbury et al. demonstrated the use of AM to produce molds for hand layup composite fabrication [H23]. Their study confirmed that the use of 3D printed molds for hand layup composites could be an effective method for low-volume production runs (4-5).

Although most of the demonstrations were for structural applications, with new enhancements in the technology, there is also an interest in functional materials. To illustrate, AM offers a low-cost alternative as a fabrication method for near-net-shape magnets, with no quantity restrictions because of its minimal material waste, and no tooling requirement. The use of BAAM, DW, and binder jet methods for fabricating Nd-Fe-B bonded magnets also has been demonstrated [50, 119, 120]. Although the technology is still immature, the capability of manufacturing bonded magnets with geometrical flexibility will open up opportunities for motor designers and sensor technology [119].

2.4.3 Design Optimization of Additively Manufactured Carbon Fiber Composites

AM can create composite structures with fiber reinforcement along preferred curved paths. This ability opens a new paradigm for designing/manufacturing parts with improved mechanical performance. The highly anisotropic properties of carbon fiber composites, in particular, will allow for placing fibers in locations and orientations that most efficiently increase the strength, stiffness, or toughness of a part under a specific loading. There is still no published work in this area.

Chapter 3. Design Considerations and Modeling of Fiber Reinforced 3D Printed Parts

Nekoda van de Werken[a], Joel Hurley[b], Pouria Khanbolouki[a], Ali N. Sarvestani[a], Ali Y. Tamijani[b] and Mehran Tehrani[a]

[a] Department of Mechanical Engineering, University of New Mexico, Albuquerque, New Mexico

[b] Embry-Riddle Aeronautical University, Daytona Beach, Florida

3D printing of high strength, lightweight, and relatively inexpensive parts can save engineers time and resources not possible otherwise. Continuous fiber reinforced polymer 3D printing has recently emerged to address this need. In contrast to conventional composites that consist of unidirectional or woven laminates, continuous fibers in 3D printed composites can be used to only partially reinforce each layer and/or be printed in curved patterns (infill patterns) to enhance mechanical performance. Understanding the mechanics of this new class of 3D printed (additively manufactured) composites is required for their optimal design and utilization in various applications. In this work, the thermo-mechanical response and failure mechanics of 3D printed composites are evaluated and correlated to their structure. We show that the strength of the 3D printed specimens depends strongly on the infill patterns and part geometry. Specifically, fiber curvatures and interfaces between reinforced and non-reinforced regions result in stress concentrations, multi-axial stress states, and pre-mature failure in parts. To better understand the failure in 3D printed composite structures, finite element analysis (FEA) was used. To this end, anisotropic properties were assigned to each element of the generated mesh based on the local fiber direction. FEA was able to capture experimental failure stresses and shed light on the

failure mechanisms in tested specimens. Finally, we present rudimentary design rules that can be useful for designing 3D printed fiber reinforced parts.

Keywords: Fiber Reinforced Filament; Finite Element Analysis (FEA); 3D printing; Mechanical Properties

3.1 Introduction

Carbon fiber reinforced polymer composites (CFRP) offer significant advantages over metallic materials in that they are lightweight, possess a high strength and stiffness, and are resistant to corrosion and fatigue [2]. In most CFRPs, thermosetting matrices are used due to their low viscosity, high interfacial strength, and favorable mechanical properties. Thermoplastics, on the other hand, do not readily form strong bonds to the carbon fiber surface, however, retain a few notable advantages. One such advantage is the ability of thermoplastics to be additively manufactured using the widely developed and readily accessible polymer extrusion techniques (fused filament fabrication, FFF, or fused deposition modeling, FDM)[5, 20]; FDM involves melting filaments of material and depositing the melt on a substrate layer by layer. Recently, 3D printing of fiber reinforced polymers has emerged towards manufacturing strong/stiff parts without the need for multiple processes and special tools [5]. To reinforce 3D printed plastics both discontinuous (short) and continuous carbon fibers can be used.

Different types of reinforcement materials such as polymer fibrils [121], carbon nanotubes [122], glass fibers [30] and carbon black [123] have been used with polymer FDM. In particular, continuous [71] and short [6, 23] carbon fiber reinforced filaments are a promising development in FDM materials. An advantage of these filaments is that they are compatible with most commercial desktop 3D printers in the market with a heated bed and steel nozzle. Tekinalp et al. observed that, for less than 30% carbon fiber loading, while short carbon fiber polymer

composites prepared by FDM 3D printing show higher porosity than samples fabricated by conventional compression molding, both showed similar tensile modulus [23]. For fiber loadings in excess of 40%, however, compression molded carbon fiber reinforced polymer composite showed higher tensile modulus [23]. Love et al. 3D printed acrylonitrile butadiene styrene (ABS) reinforced with carbon fiber (13% volume fraction) and reported increase of strength by approximately 200% and modulus by 400% [6].

Even if the short fiber reinforcements are aligned in the filament, strength and stiffness of 3D printed specimens culminate at ~ 250 MPa and 25 GPa, respectively [5, 23, 38]. Although these properties are interesting when compared with non-reinforced plastics, they are much lower than what can be achieved with continuous carbon fiber reinforced filaments; tensile strength and stiffness values of >700 MPa and >50 GPa, respectively. Continuous fiber reinforced 3D printing enables manufacturing of parts with metal-like properties in short time, for reasonable costs, and with less waste production.

Strength, Young's modulus and density of most commonly 3D printed materials using FDM, stereolithography (SLA), selective laser sintering (SLS), and selective laser melting (SLM) are shown in Figure 15. Continuous fiber reinforced plastics fill a gap between metals and polymers, and even compete with 3D printed metals when normalized by density. It should be noted that most 3D printing technologies result in anisotropic properties in the three major axes of the build structure. For continuous fiber reinforced parts, this anisotropy is significant, and properties are up to an order of magnitude different in directions parallel and perpendicular to the fiber direction. Because of this anisotropy, fibers can be placed in desired patterns in each layer to enhance mechanical performance [124, 125]. Moreover, parts can be partially reinforced with fibers to save material. For example, to achieve a high bending stiffness in a part, only the top

and bottom layers need to be reinforced with fibers. Similarly, for a high torsional stiffness only the outer perimeter of a part needs to be fiber reinforced. In order to benefit from these novel concepts, understanding of structure, mechanical performance and failure mechanics in 3D printed composite parts with partial reinforcement and curved fiber reinforcements, respectively, are required.

In this work, the microstructure and thermo-mechanical properties of continuous carbon fiber reinforced 3D printed specimens are investigated. Cross-sectional microscopy was performed to understand the structure at the fiber and filaments level. Finite element analysis (FEA) was utilized to understand and subsequently predict the failure load and mode, respectively, in 3D printed parts. To account for the orientation of the curved fiber reinforcements, each FEA element was given its own independent material property commensurate to the local fiber orientation at the element position. The variable orientation continuous fiber design requires the construction of hundreds to thousands of elements with various material properties that is only practical when an automated modeling process is applied. Thus, a framework was developed to model continuous fiber reinforcements. This framework interfaces MSC.NASTRAN to perform the FEA.

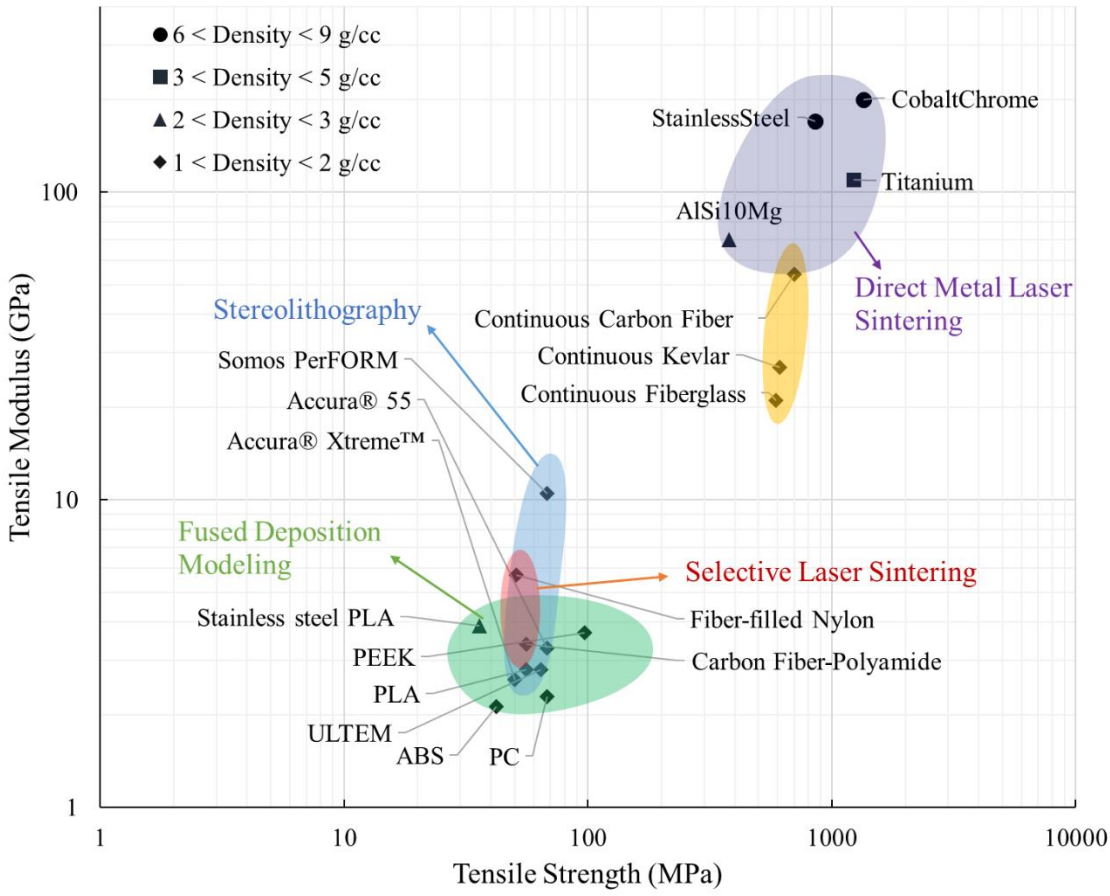

Figure 15. Strength versus stiffness for commercially available 3D printed materials [14-23]. PC: polycarbonate, ABS: acrylonitrile butadiene styrene, ULTEM: a family of polyetherimide, PLA: polylactic acid, and PEEK: polyetheretherketone.

3.2 Material and Methods

Carbon fiber reinforced specimens were 3D printed using a Markforged commercial printer. Each carbon fiber reinforced filament has a diameter of 0.4 mm and when printed forms features that are ~1 mm wide and ~0.12 mm tall. The printed filaments can follow curved paths to partially or fully reinforce each layer, as shown in Figure 16. The non-reinforced areas are filled with nylon. The infill pattern affects the strength and failure mode in 3D printed parts.

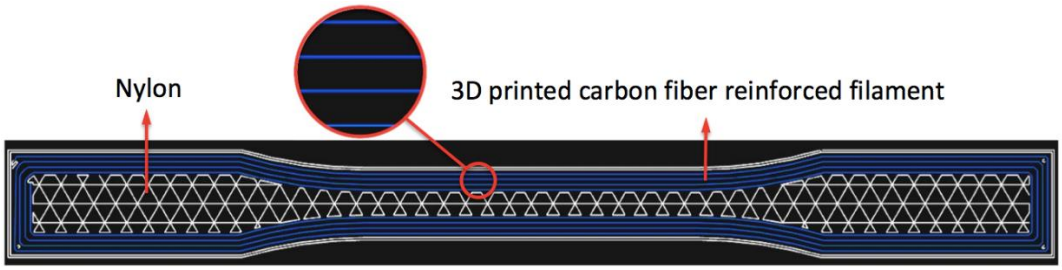

Figure 16. The 2D internal layer structure of a partially reinforced 3D printed sample. The blue lines represent the printed carbon fiber reinforced paths and the rest of the layer is printed with nylon.

Cross-sectional samples with carbon fibers perpendicular to the cut direction were prepared for microscopy. Standard sample preparation practices were carried out to prepare a smooth surface; grinding with 120, 400, 600, and 1000 grit size papers followed by 6 and 1 micron diamond polishing. A metallurgical optical microscope and an FEI Q3D scanning electron microscope (SEM) were utilized for microstructure characterization. Samples were gold coated for SEM studies.

Tensile tests were performed on 3D printed samples using an Instron machine. An extensometer with a 25.4 mm gauge length was used to measure strain.

The density and volume fraction of the composites were measured in accordance with the ASTM D792 and ASTM D3171, respectively. The volume of the sample was found by measuring the buoyancy force acting on the sample while submerged in water and using the density of water to calculate the displaced volume. The matrix digestion was performed using 70% w/w nitric acid at 60 °C with magnetic stirring for 4 hours. After matrix digestion, the sample was rinsed with DI water three times and a final wash was done with acetone. The sample was then dried in an oven at 100 °C for one hour, after which the mass of the fibers was measured. The density of the carbon fiber and nylon matrix were assumed to be 1.76 (assumed for T300 Toray fibers) and

1.15 g/cm^3, respectively. The volumes of the carbon fibers and composite part were then used to calculate the volume fraction.

Dynamic mechanical analysis (DMA) was performed in accordance with the ASTM standard D7028-07 using a TA instruments Q800 DMA. For this test, a heating rate of 3 °C/min from ambient temperature up to 140 °C and a strain amplitude of 0.1% at 1 Hz was used. Five samples with fiber reinforced filaments printed in the longitudinal direction were cut from a bulk 3D printed cube using an IsoMet 4000 precision saw. A 3-point bending clamp with a span of 2 cm was used.

3.2.1 Modeling and Simulations

The FEA model was based off the geometry and infill layout provided by the .stl files. Curvilinear printed filaments can be difficult to model because the fiber angle varies from one element to another, causing the material properties to vary as a function of position in the structure. Additionally, properties for the non-reinforced regions need to be defined. Generating individual material properties for each element in the mesh would be laborious. This led to the development of an automated modeling system that creates elements based on the orientation of the fiber, obtained from image processing of the printing pattern (Figure 17a). By overlaying the element centroids over the digitized fiber data, the local material orientations for each element were determined from interpolation and local fiber orientations were mapped onto the centroid of each element. Figure 17b shows the finite element mesh (4-node composite shell elements) used to describe the geometry of the model. The strain energy was used as a convergence criterion in the finite element analysis. It was found from previous design iterations that variable stiffness composites are extremely sensitive to mesh smoothness. Therefore, the bands of curved fibers along the part's perimeter are meshed with their own smooth bands of elements. Two different

material properties are introduced. The first one describes the carbon fiber reinforced material used throughout the majority of the structure. The second material is an isotropic material that describes the small pockets of nylon, which are used by the 3D printer to fill in the areas where the carbon fiber reinforced filaments are not placed. Figure 17c depicts the carbon fiber reinforcement regions in blue and nylon regions in red. The elements of the model that are located in the regions of the nylon filler material were assigned separate material properties. The material properties used are presented in Table 1, as provided by the filament manufacturer or measured using ASTM standards. In this table, E is the elastic modulus, G is the shear modulus, ν is Poisson's ratio, σ is the strength at failure, and τ is the shear strength. Additionally, 1 refers to the direction parallel to the fiber axis, 2 refers to the direction perpendicular to the fiber axis, and 12 refers to in-plane shear. The superscripts ^{T} and ^{C} correspond to tensile and compressive properties, respectively. The printed specimens were tested in tension with grips attached to the wide flanges at ends. Rigid Body Elements (RBE2) were applied to simulate this load scenario by "clamping" the tabs at each end.

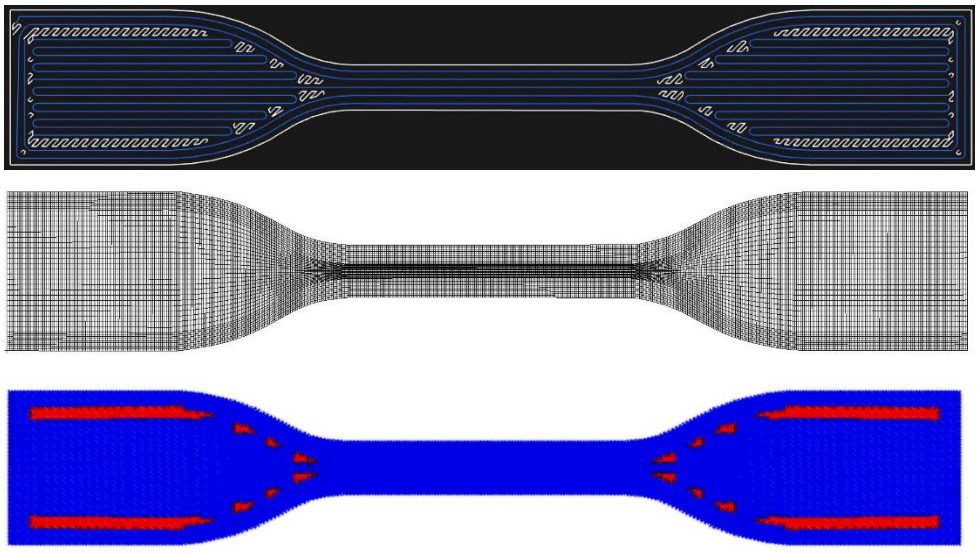

Figure 17. a) Geometry and fiber infill pattern for a sample. Blue lines represent the fiber-reinforced filaments and white regions are filled with nylon only. b) Finite element mesh using shell elements. c) Regions depicted in red specify areas of the part with nylon filler material.

Table 1. Material properties for the carbon fiber reinforced plastic and nylon.[84]

	Carbon fiber reinforced composite	Nylon
E_1	52.0 GPa	0.94 GPa
E_2	4.0 GPa	0.94 GPa
G_{12}	2.0 GPa	0.34 GPa
ν_{12}	0.33	0.4
σ_1^T	700.0 MPa	53.8 MPa
σ_1^C	-320.0 MPa	-53.8 MPa
σ_2^T	48.0 MPa	53.8 MPa
σ_2^C	-100.0 MPa	-53.8 MPa
τ_{12}	73.0 MPa	68.9 MPa

3.3 Results and Discussion

Polymer rich regions and voids can degrade the overall performance of the composite by acting as crack initiation and failure sites. Conventional unidirectional composites are fabricated under highly controlled pressure/temperature conditions and have a fiber volume fraction of ~50-65% and usually a low void content (<1%). Fig. 4. shows the cross-section of the carbon fiber reinforced filament and the 3D printed specimens. It is evident that the fibers are not evenly distributed in the matrix phase leading to inhomogeneous properties. Voids were observed in the cross-sectional images of the filaments. SEM cross-sectional images of printed samples show that more voids and cracks had formed during the 3D printing. Cracks are likely due to the poor bonding between the carbon fibers and the nylon, which is common to thermoplastic matrices. The fact that voids form linear patterns confirms that layer-by-layer printing plays an important role in the formation of voids. Extrusion of molten material onto the solidified material from previous layers seems to be the major cause for void production, which can in turn result in stress

concentration and premature failure in 3D printed parts. Similarly, polymer-rich regions are observed in the 3D Printed samples and can degrade properties by acting as failure initiation points. Fiber volume fraction was measured to be 34% and void content is estimated to be higher than 5% from cross-sectional microscopy images.

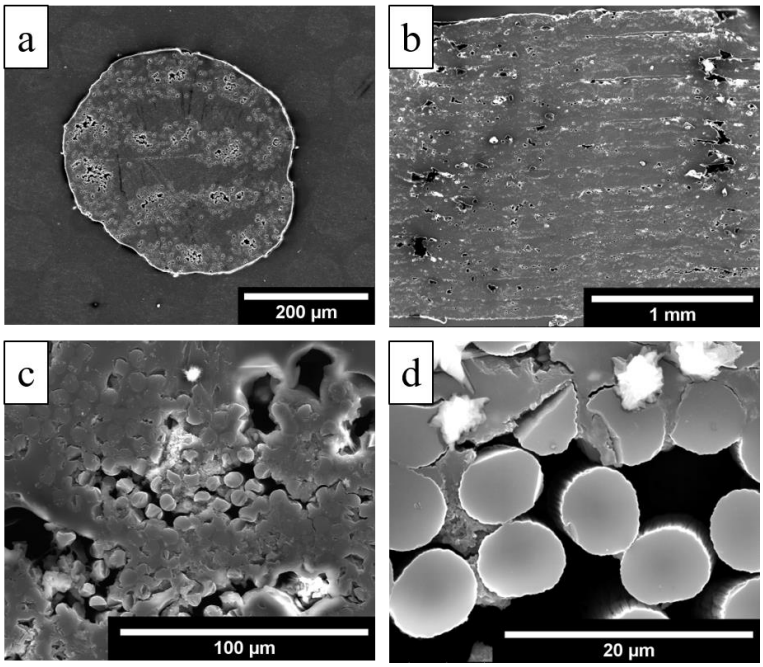

Figure 18. Scanning electron micrographs of carbon fiber reinforced filament and parts. a) Carbon fiber reinforced filament. b) Printed sample cross-section. c) Voids present in the printed composite parts. d) Carbon fiber surfaces within the printed composite parts.

Strength and modulus of the 3D printed samples were measured as 667 MPa and 53.3 GPa, respectively. The rule of mixtures (ROM) can be applied to estimate the upper limits for the strength and stiffness of the 3D printing composites. Considering a fiber volume fraction of 34% and properties for standard modulus T300 Toray carbon fibers (modulus of 230 GPa and strength of 3530 MPa), upper limits for the strength and stiffness can be calculated as 1200 MPa and 78 GPa, respectively. It should be noted that even in conventional composites, the ROM predictions tend to be around 20% higher than experimental values for strength, due to manufacturing

defects, fiber strength distribution, and fractured fiber end effects [126]. An upper strength limit of an~1000 MPa can therefore be considered. The relatively high void content, low interfacial shear strength between fiber and matrix, and the polymer rich regions are contributing to the relatively poor performance of 3D printed composites. The tensile strength of a composite can decrease due to the presence of voids [127], and low interfacial shear strength can significantly decrease strength of carbon fiber reinforced polymer composites [126, 128]. As shown in the post-fracture micrograph in Figure 19, most fiber surfaces are clean, confirming the weak interfacial strength between fiber and matrix. As mentioned earlier, carbon fibers do not readily form strong bonds to thermoplastic polymers including the polymer matrix used in this study.

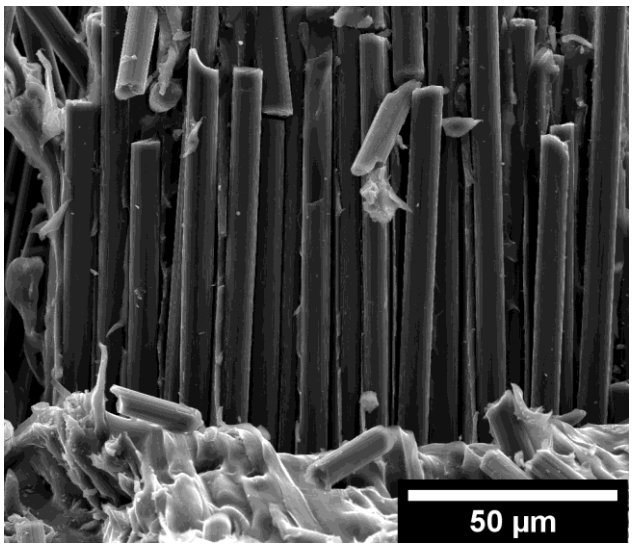

Figure 19. Post fracture micrograph showing clean carbon fiber surfaces.

DMA tests were carried out on 3D printed specimens that were fully reinforced with carbon fiber filaments. All the 3D Printed filaments were oriented along the length of the samples. Storage and tensile modulus values for thin composite samples are usually similar along identical directions [129, 130]. The measured room temperature storage modulus was approximately 52

GPa, which is close to the measured tensile modulus for the samples. Figure 20 illustrates the DMA test results averaged for 5 samples, showing a glass transition temperature (from Tanδ peak, solid red curve) of 135.4 °C and a shoulder around 120 °C. Storage modulus (dashed black curve) is nearly constant below 70 °C and drops only by 7% at 90 °C. Above 90°C, the modulus decreases significantly.

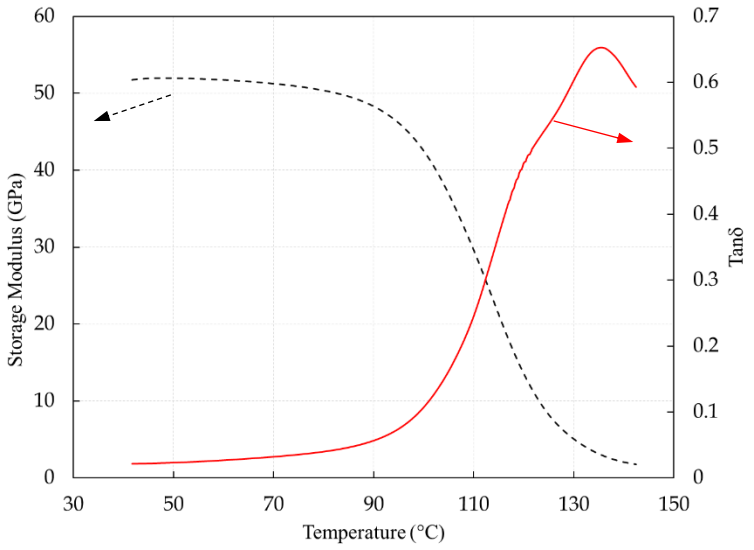

Figure 20. Storage modulus (dashed black curve) and Tan□ (solid red curve) of the 3D printed samples.

ASTM D3039 specimens are commonly used for tensile testing of fiber-reinforced plastics. These samples have a rectangular shape with beveled tabs at their ends, where the tabs are added after the composite is fabricated. In this study, however, tabs were 3D printed together with the bulk of the sample. As mentioned earlier, tensile specimens with printed filaments in the longitudinal direction exhibited an average tensile strength and modulus of 667 MPa and 53.3 GPa, respectively. These values are within 5% of properties reported by the manufacturer.

In order to investigate the effects of partial and curvilinear reinforcement, respectively, samples with different geometry and fiber infill patterns were printed and tested in tension. To this end,

two different sample types, Type I (Figure 16) and Type II (Figure 17a), were considered. These sample geometries were intentionally chosen to result in a multi-axial stress state close to the grip region. Post fracture observations showed that samples failed due to fiber failure and inter-filament cracking. The latter failure mode, which resembles interlaminar failure in conventional composites, is a result of manufacturing defects. As such, the solidification of molten filaments adjacent to solid materials results in poor interfaces. Moreover, air gets trapped between the filaments resulting in voids. Both Type I and II samples failed outside the gauge section, due to an interactive multi-axial stress state, at loads far less than their predicted gauge strength. For example, the Type II sample failed at a gauge stress of 223±9 MPa, almost one third of the predicted sample's gauge strength. Type II specimens exhibited a modulus of 54±2 GPa. As shown in Figure 21, failure mode in Type II samples was inter-filament failure where cracks initiated in regions that contained nylon (nylon pockets between carbon fiber reinforced regions close to the tabs Figure 22a) and extended longitudinally throughout the sample.

Figure 21. Fractured sample (Type II) exhibiting inter-filament failure. Box contains the longitudinal matrix crack and arrows point out the crack initiation points.

The normal stresses in the fiber direction for this sample, at the failure load, are shown in Figure 22b. It can be seen that the maximum normal stress occurs in the single band of filament (Figure 22a) that runs through the center of the part. Because the nylon is experiencing little stress at the neck, we can conclude that the load is being transferred solely through the fibers and bypassing

the nylon filled regions altogether. Figure 22c shows the fiber direction shear stresses. The maximum shear stresses occur in the neck section along the boundary between the nylon and composite regions.

Maximum stress, maximum strain, and Tsai-Wu are the three most widely used failure criteria used for composites analysis. If these criteria do not work, more complicated ones can be used. The failure was therefore predicted using the Tsai-Wu failure theory. Figure 24d shows the Tsai-Wu indices at failure for the Type II sample. The failure location is predicted in the neck region along the seam between the composite and nylon regions. Table 2 shows the corresponding stresses at the failure location. By comparing these stresses to strength values from Table 1, we conclude that failure occurs due to a combination of high stresses perpendicular to the filament direction and high shear stresses. This agrees with the tensile test results from Figure 21, which shows failure in the same location. We can also conclude from the FEA that the σ_y stresses in the failure location led to de-bonding of the composite from the nylon filler triggering a longitudinal crack along the length of the part. At this failure load, the FEA average normal stress at the gauge is 226 MPa and is 1.3% higher than the experimental stress. It should be noted that similar to the analysis of conventional composites, x and y refer to the global coordinate system while 1 and 2 represent the local fiber coordinate system.

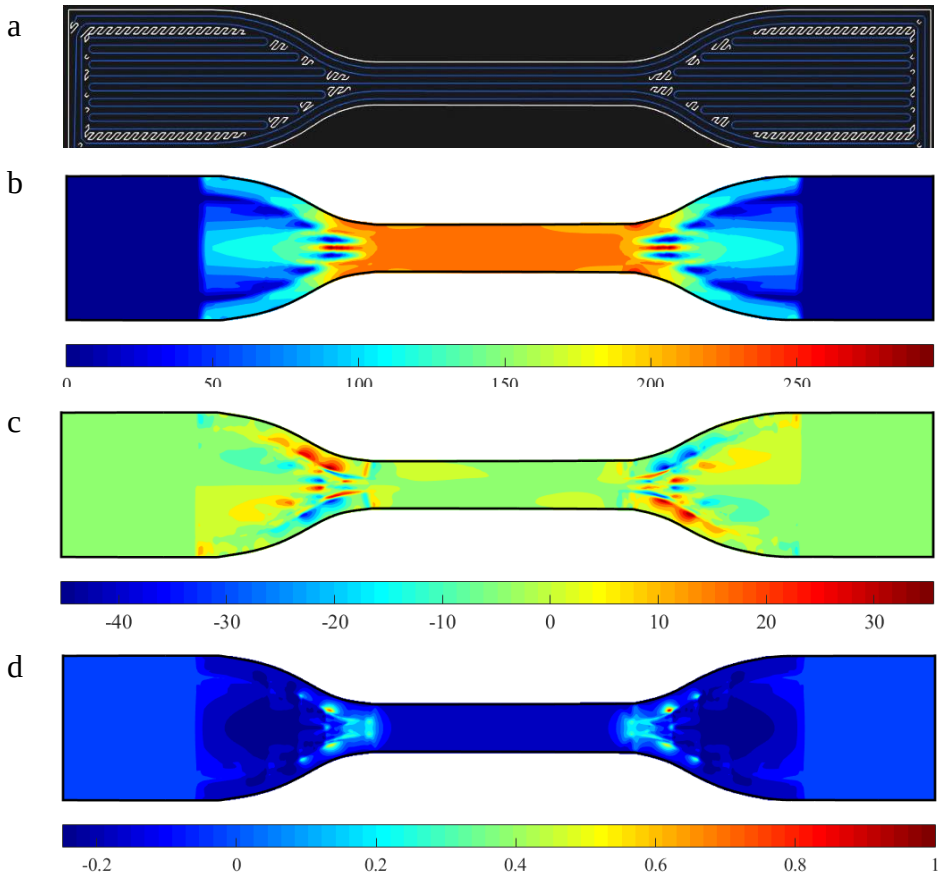

Figure 22. a) Type II sample geometry and infill pattern, b) σ_1 normal stress [MPa] at failure load, c) τ_12 shear stress [MPa] at failure load, and d) Tsai-Wu failure indices at failure load. "1" and "2" subscripts refer to the local fiber coordinate system, with 1 being the direction parallel to the fiber axis and 3 being the direction perpendicular to the fiber axis in the printing plane.

Table 2. FEA failure stresses for the Type II model

Gauge normal stress [MPa]		Failure location FEA stresses [MPa]		
FEA	Experimental	σ_1	σ_2	τ_{12}
226	223±9	222	34.6	-37.8

For the partially reinforced samples, the relationship between the carbon fiber reinforcement fractions to the mechanical properties of the printed parts was investigated. Type I samples with different number of reinforced printed filaments were manufactured and tested in tension. Each sample had a total of 24 printed layers, and each layer was reinforced with 2, 3, 4, 5, or 6 concentric filament rings, respectively, as shown in Figure 23. For example, the specimen shown schematically in Figure 23 is reinforced with 4 concentric rings; i.e., 8 printed filaments pass through the gauge section and ~60% of the gauge section is reinforced. Tensile modulus and gauge stress at failure for these samples as a function of the percentage of the carbon fiber reinforced filament at gauge (referred to as ν_{CF} hereafter) is plotted in Figure 23. It should be noted that the carbon fiber volume fraction in the printed filament is 34%, and is different than the ν_{CF}. Specifically, ν_{CF} is defined as the ratio of carbon fiber reinforced cross-sectional area to the overall area at the gauge section consisting of both carbon fiber reinforced plastic and neat nylon. For example, the ν_{CF} in the four concentric ring specimen is ~60%.

As expected, elastic modulus varies linearly with respect to ν_{CF}. Tensile strength is approximately linear up to 60% ν_{CF}, and drops for higher values of ν_{CF}. The failure mode for low ν_{CF} samples was primarily fiber failure while samples with high ν_{CF} (>60%) exhibited a mixed delamination and fiber failure. All tested samples failed along the curved region near the grips. The gauge strength for each sample can be estimated by multiplying ν_{CF} by the strength of the filaments, i.e., ~700 MPa; the strength of nylon can be neglected as it is an order of magnitude lower than the fiber reinforced filaments. Experimentally measured gauge strengths are 30-50% lower than the estimated gauge strengths based on the above mentioned calculations, with larger differences for higher ν_{CF} samples. This strength reduction is a result of a complex multi-axial stress state due to the sample geomtry and the presence of curved fiber path, causing failure in

the tab region. To understand the effects of fiber infill geometry on the strength and failure in these samples, FEA simulations were conducted.

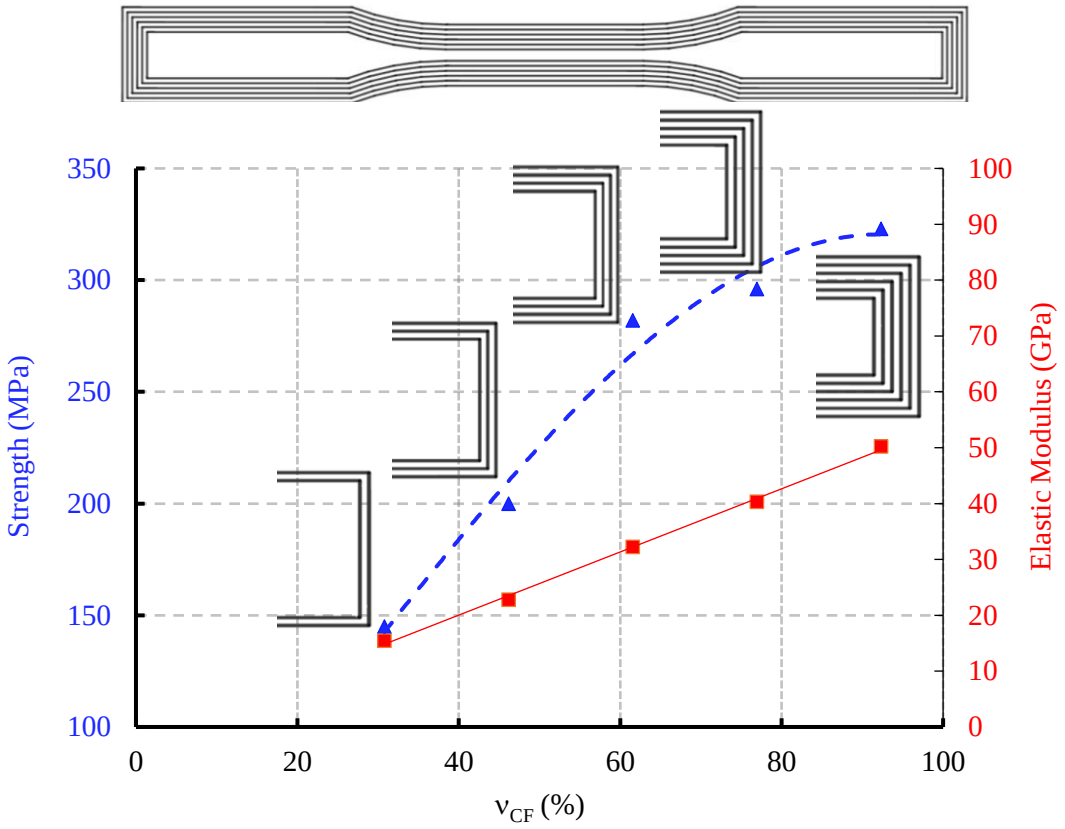

Figure 23. Failure stress and Young's modulus at the gauge section as a function of ν_{CF} (% of the gauge cross-section reinforced with printed carbon fiber filaments) for the Type I sample geometry. Printing pattern for each sample is schematically shown in inset figures, where a representative section of sample end displaying carbon fiber printed filaments is shown.

Models of the Type I specimens (Figure 16), with varying numbers of concentric rings, were generated and analyzed (Figure 24). There is close agreement between the FEA and experimental results, particularly for higher volume fractions of carbon fiber filament, as seen in Fig. 10. The FEA model typically approximates the experimental results within 10% of the normalized stress at failure. For all specimens, gauge stress at failure is 30-50% lower than that predicted by the rule of mixtures (ROM) (i.e., ν_{CF} x 700 MPa). As mentioned earlier, the difference between the

measured and ROM estimated values of gauge strength increases with ν_{CF}. To understand this, the failure mechanics from FEA was studied.

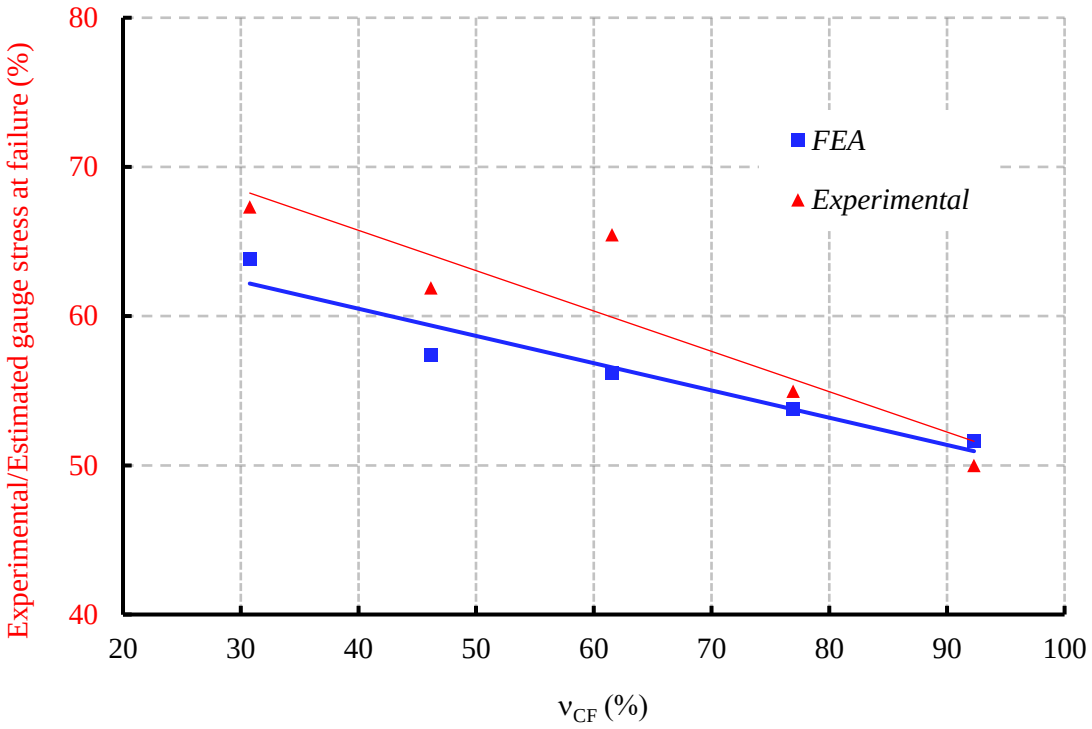

Figure 24. Experimental and FEA results for the failure stress over the rule of mixtures (ROM) predicted strength as a function of □CF (fraction of reinforced gauge section) for the Type I sample geometry.

The fiber direction normal stresses and shear stresses at failure load for the Type I model with 6 concentric reinforced filament rings are shown in Figure 25a and Figure 25b, respectively. The largest normal stresses occur in the interior of the part at the transition between the neck and flange as shown in Fig. 11a. The largest shear stresses occur in the same region, except slightly further inwards from the boundary between nylon and composite, as shown in Fig. 11b. The resulting Tsai-Wu failure indices are shown in Figure 25c. Inspection of the failure indices indicates that failure occurs within the composite at the location of peak shear stress.

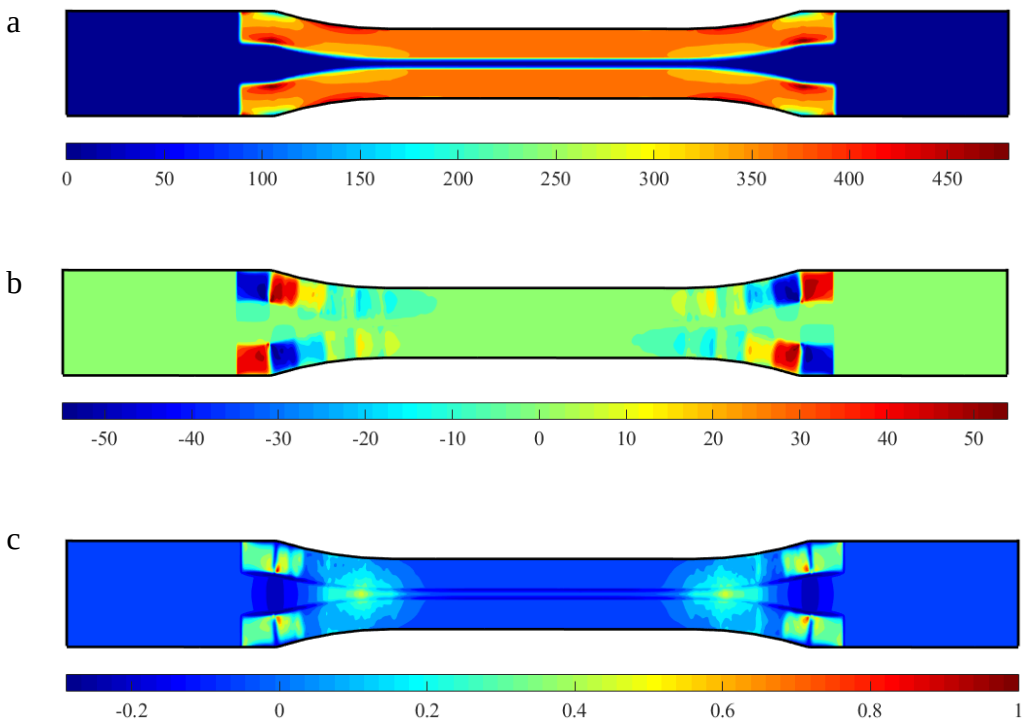

Figure 25. FEA tensile analysis of Type I samples with 6 concentric rings (ν_{CF} ~ 0.9): a) σ_1 normal stress [MPa] at failure load b) τ_{12} shear stress [MPa] at failure load, and c) Tsai-Wu failure indices at failure load. "1" and "2" subscripts refer to the local fiber coordinate system.

Individual analyses were performed for each set of concentric rings, which varied from two to six. The strength improved linearly as the amount of fiber increases. However, the normal and shear stresses varied. As the ν_{CF} increases, the maximum shear stresses increase and the maximum normal stresses decreases, as illustrated in Figure 26. Models with 5 and 6 rings, corresponding to ν_{CF} ~ 0.75 and 0.9, respectively, have a much larger component of shear stress at the failure location (contributing to an interactive failure) than specimens with fewer rings, which have a larger component of normal stress at the same location. It should be noted that while the FEA strength values of Figure 24 are close to the experimentally measured values,

slight discrepancies are observed. We speculate that void content increases with carbon fiber fraction, and thus has a greater contribution toward failure for samples with higher ν_{CF}.

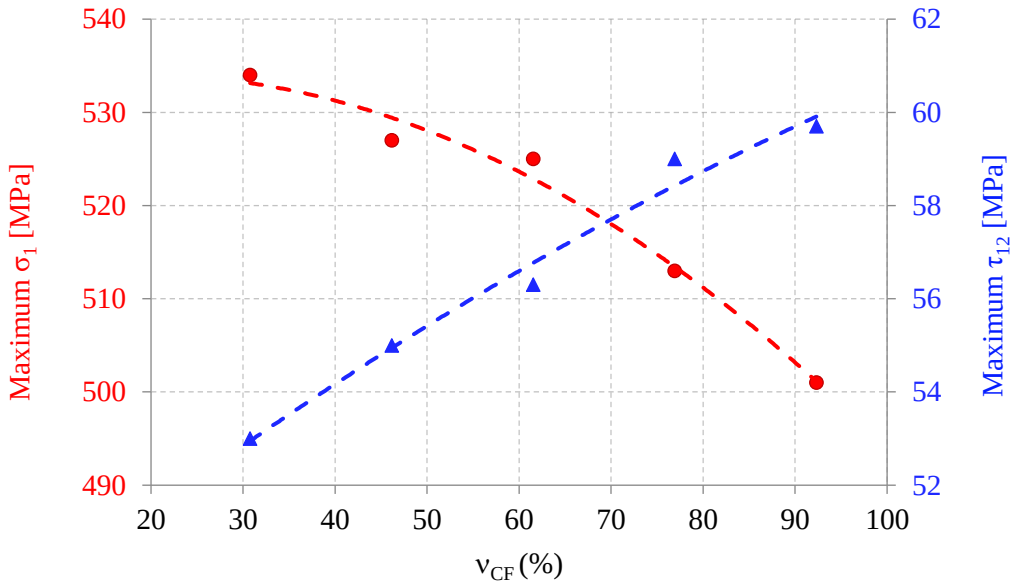

Figure 26. The relationship between the maximum normal and shear stresses at failure versus v_{CF}(% of the gauge section reinforced with printed carbon fiber filaments) for the Type I sample geometry.

Regardless of the number of concentric filament rings, the failure location for all the Type I models occurred in the transition between the neck and flange, near the boundary between the nylon filler and the composite. This contrasts with the Type II model (Figure 22) in three notable ways. First, the failure occurs far from the gauge and closer to the point of load application at the grips, where the part has a larger cross-sectional area. Secondly, the failure is occurring approximately 0.75mm inwards from the boundary between the composite and nylon, which suggests fiber failure. The Type II model failed directly along the seam between the two materials, which resulted from matrix failure. Third, for the Type I model, the σ_2 stress is

relatively small and contained inside the nylon filler regions. Therefore the failure is dictated solely by the σ_1 and τ_{12} stresses interactions in the composite. This contrasts with the Type II model, which saw large multi-axial stresses at the failure location.

A comparison of stress distributions for the Type I specimens with 3 and 6 concentric rings, for the σ_1 normal stress and the τ_{12} shear stress, is presented in Figure 27. Comparison of failure stresses at different vCF, a) σ_x [MPa] for vCF ~ 0.9, b) σ_1 [MPa] for vCF ~ 0.45, c) τ_12 [MPa] for v_{CF} ~ 0.9, d) τ_12 [MPa] for vCF ~ 0.45. "1" and "2" subscripts refer to the fiber local coordinate system.

During tensile testing, it was observed that all parts exhibited fiber failure, with the 5 and 6 ring parts showing a combination of fiber/matrix failure. The FEA partially confirms this result.

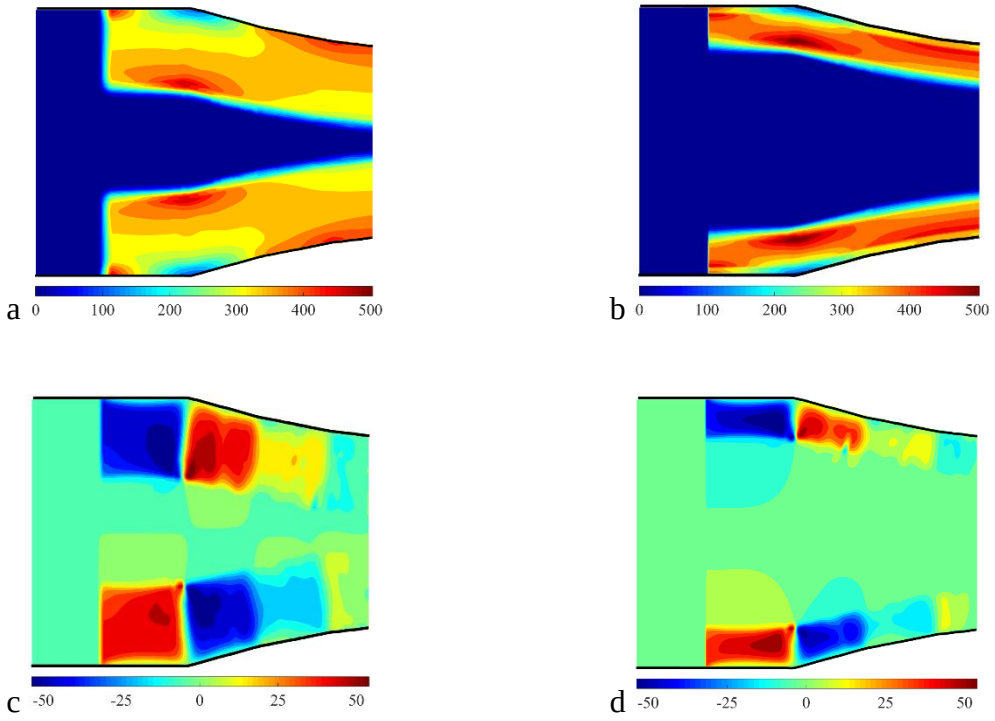

Figure 27. Comparison of failure stresses at different v_{CF}, a) σ_x [MPa] for v_{CF} ~ 0.9, b) σ_1 [MPa] for v_{CF} ~ 0.45, c) τ_12 [MPa] for v_{CF} ~ 0.9, d) τ_12 [MPa] for v_{CF} ~ 0.45. "1" and "2" subscripts refer to the fiber local coordinate system.

The FEA of the Type I and Type II models demonstrate how fiber volume fraction, infill patterns, and geometric features influence the distribution of stresses within additively manufactured continuous fiber composites. With conventional composites, or isotropic materials, the geometric features of the structure solely govern the location of the failure, which usually occurs at the outer edge of a feature. It is shown from FEA that implementing variable stiffness composites, with the same geometry, can lead to counter intuitive failure locations, including failures from within the part that propagate outward. This demonstrates the importance of including FEA in the design of 3D printed composite structures.

3.4 Conclusions

In this work, the mechanical properties of 3D printed composites samples reinforced with continuous carbon fibers were characterized. Surface microscopy indicated that a relatively large number of voids is present in the 3D printed parts that lead to failure stresses that are lower that theoretical predictions. This significant void content is inherent to the layer-by-layer 3D printing process and contributes to particular failure modes during tensile tests. Similar to conventional composites, different failure modes such as inter-filament failure, delamination and fiber failure were observed. It was also concluded from observations of fiber pullout that the interfacial strength between the fiber and matrix is relatively low.

To gain insight into the failure modes, numerical simulations were also performed. The predictions of numerical simulations for failure modes were close to the experimentally measured values. It was confirmed that the geometry, infill pattern and infill percentage significantly influence the failure strength and modes. It is also concluded that only FEA simulations can predict the mechanical performance of 3D printed parts for complex failure

scenarios. As rudimentary design protocol, one may avoid infill patterns where small regions between carbon fiber printed material is filled with nylon and that stress concentrations due to infill pattern become more significant at higher curved carbon fiber infill amounts.

Chapter 4. Stiffness-Based Design Optimization of Additively Manufactured Continuous Fiber Composites

Nekoda van de Werken[a], Rossana Fernandes[b], Pratik Koirala[c], Ali Tamijani[b], and Mehran Tehrani[a,c]

[a] Department of Mechanical Engineering, University of New Mexico, Albuquerque, NM, 87131

[b] Aerospace Engineering Department, Embry-Riddle Aeronautical University, Daytona Beach, FL, 32114

[c] Walker Department of Mechanical Engineering, University of Texas at Austin, Austin, TX, 78712

Additively manufactured (AM) fiber-reinforced composites have recently begun to demonstrate the capability of AM techniques to produce polymer-based parts for functional end-use applications. This technology can distinguish itself from conventional composite manufacturing methods by enabling a variety of complex geometries, eliminating the need for molds/tooling, out-of-autoclave processing, and a reduction of material waste. Accompanying these improvements is the ability to tailor the placement and orientation of fiber reinforcement within each composite lamina to improve part performance for a given state of stress. AM technology is inherently well-suited for integration with optimization schemes, as the geometrically complex models produced through optimization can be sent directly to a 3D printer. This study investigates the improvement in part stiffness normalized by weight for three benchmark geometries, which result from topology (shape) and fiber placement (morphology) optimization in AM continuous carbon fiber reinforced polymer matrix composites. Specifically, compliance minimization through topology and fiber morphology optimization was performed on a three-point loaded beam, a cantilever plate, and an L-shape design. The optimized designs were manufactured on a custom-built continuous fiber fused filament fabrication (FFF) printer and loaded in a load frame while part displacements were recorded using digital image correlation

(DIC). The specific stiffness found through experimentation agreed with finite element analysis (FEA) predictions and displayed up to two-fold improvement in specific stiffness over non-optimized geometries. This study demonstrates that the merging the continuous fibers with AM enables significant weight reduction that would otherwise not be possible.

4.1 Introduction

The exceptional strength- and stiffness-to-weight ratios of carbon fiber composites make them highly desirable for weight critical applications. Recently, this material class has transitioned into the domain of additive manufacturing (AM), which offers unique advantages over conventional composite manufacturing methods. Specifically, the capability of manufacturing complex geometries, short production lead times, and control over the internal placement and orientation of fiber reinforcement open interesting possibilities for the technology in industry and academic research [131, 132].

Topology optimization has been used as a powerful tool for AM design [133]. Topology optimization of both structural parts, such as cellular structures and metamaterials [134-138], and support structures is an active research field [139-141]. The design freedom of AM and the highly anisotropic composite properties can be synergistically utilized to fabricate parts with adaptive fiber paths that are optimized for specific loading conditions. In sharp contrast to isotropic materials, the axial tensile strength and stiffness of unidirectional carbon fiber composites can be up to two orders of magnitude larger than their transverse counterparts [142]. Traditional composite design or optimization methods focus on engineering the stacking sequence, or orientation of each lamina within a laminate, to improve the part performance and reduce mass. AM, however, allows for individual carbon fiber filaments to be placed and

oriented at will within a composite, aligning the fibers in the most efficient orientations to further reduce part mass and improve specific properties.

The use of carbon fiber as a reinforcement in polymer-based additive manufacturing has been extensively investigated and reviewed in the literature, though the full potential of continuous fiber reinforced AM has yet to be achieved [19-22, 131]. One route toward improvement of AM continuous fiber composites, which have currently not been explored in literature, is to assist in the design process with topology optimization techniques. The interest in the topology and morphology (fiber orientation) optimization of continuous fiber 3D printed composites is motivated by four factors: a) the incorporation of fibers in 3D printed materials reduces the natural warping and distortion tendency observed in 3D printed polymers; b) continuous carbon fibers have shown to improve 3D printed polymer mechanical properties (strength and stiffness) by 1 – 2 order of magnitude for an additional 25-50% weight [132]; c) continuous fiber 3D printing technology is more economical than metal 3D printing; and d) continuous fiber paths can be optimized to produce a more effectual load distribution maximizing the strength and stiffness of the model.

This study focuses on demonstrating the power of continuous fiber composite AM for structural light-weighting. To this end, we present a systematic study on elastic response of three benchmark structures (Figure 28), subjected to certain plane-stress loading conditions. A stiffens-based design optimization framework, developed for continuous composites, was used to find optimized topology and morphology designs for the studied structures. Two topology-optimization schemes have been used: Solid Orthotropic Material with Penalization (SOMP) and

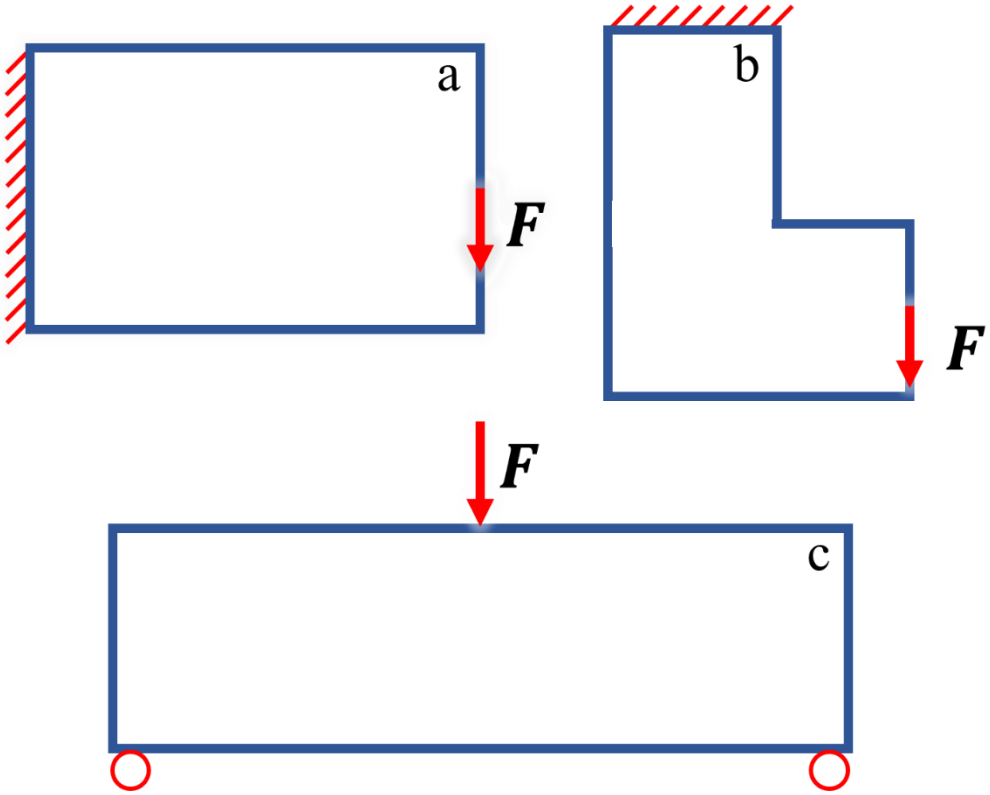

Figure 28. Schematics of the three geometries, constraints, and loading profiles under investigation. a) Cantilever b) L-shape c) MBB beam.

level set. The fibers were then placed according to the Equally Spaced (EQS) and offset methods introduced in earlier by the authors [143]. The optimized models were slightly modified to ensure manufacturability. Finite element analysis (FEA) was utilized to analyze the response of optimized models. The designed computer models were converted to G-codes and printed on a custom-built printer. The structures were subsequently loaded under identical conditions to those used for the design optimization and FEA. Finally, FEA results were compared to the digital image correlation (DIC) data from the experiments.

4.2 Materials and Methods

4.2.1 Experimental materials and methods

The composite parts were manufactured on a modified cartesian 3D printer, as seen in Figure 29. The printer used the commercially available continuous carbon fiber reinforced polyamide 6 (PA6) filaments (0.4 mm diameter) from Markforged. The flexural strength and modulus of the parts manufactured with continuous carbon fiber reinforced filament exceeds those of unfilled nylon by a factor of 10.2 and 36.4, respectively, with only a 9% difference in density [144]. Therefore, while the printer was equipped with two independent extruders, allowing both filled and unfilled nylon to be printed in the same part, only the reinforced filament was used to manufacture the parts for this study. A cutting mechanism was added to the printer for carbon

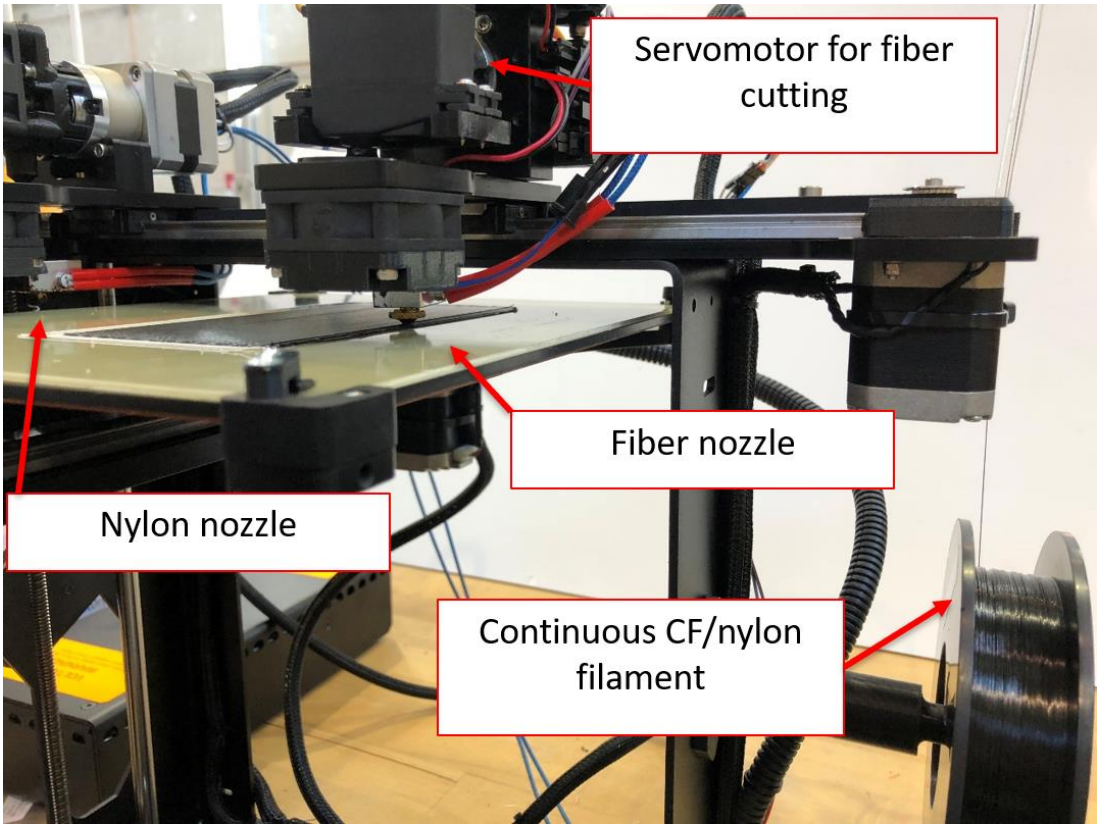

Figure 29. Cartesian 3D printer modified to print continuous carbon fiber reinforced PA6 filament.

fiber scission, allowing for discrete paths to be printed. A nozzle temperature of 260°C, bed temperature of 85°C, print speed of 500 mm/min, and layer height of 0.125 mm were chosen as the print parameters.

The quality of parts printed on the modified continuous fiber printer were verified by comparing the properties of flexural samples printed on the modified printer to those printed on a commercially available printer specifically designed to use the filaments (i.e., Mark Two by Markforged). The specimens were prepared and tested in accordance with ASTM D7264 using an MTS bionix 793 frame equipped with a 25 kN load cell. Samples were manufactured to a size of 1x13x51mm and tested at a span of 25.4 mm, with a constant crosshead displacement rate of 1mm/min. All cylinder diameters for the support and applied force had a diameter of 10mm.

The planar coordinates of each fiber path were generated using the optimization software. These coordinates were converted into G-code to run the printer using a MATLAB script, provided in Appendix I. This script translated the planar coordinates of the fiber paths into an appropriate location on the print bed, calculated the appropriate extrusion length for each path, and inserted a cutting command at a specified length before the end of each path. This distance corresponded to the length between the cutting mechanism and the tip of the nozzle. Considerations of the width of each fiber path and the minimum radius of curvature that could be reliably printed were enforced during path optimization.

Three geometries and loading conditions were chosen for this study, which are commonly used as a benchmark for topology optimization studies [145]. Topology and fiber morphology optimization was implemented to minimize compliance on an MBB beam, a 5:8 (length to width) plate, and an L-shape design, as shown in Figure 28. The non-optimized case of the 5:8 cantilever, a unidirectional plate with all fibers oriented along the length of the beam, was also

manufactured as a reference. Each part was printed to a thickness between 2-5.5 mm, depending on the tendency of the part for non-planar deformation during the experiment. The performance of each design was evaluated based on its specific stiffness, being the slope of a force/mass-displacement curve.

As the studied parts contained non-standard geometries for characterization, custom clamps were manufactured to fix the parts to the MTS Bionix 793 testing frame. A displacement rate of 0.5 mm/s was applied during testing, and the force was captured as a function of time by a 25kN load cell. Full-field displacement and strain was calculated using single camera digital image correlation (DIC) [146, 147]. As this study focuses on measuring the stiffness of each part, only the linear-elastic response of the material was needed for characterization, allowing for the assumption of strictly in-plane deformation. If out-of-plane deformation was observed during a test, the part thickness was increased to reduce the propensity for out-of-plane deformations at small displacements. By applying only small deformations, the propensity of the part to slip on the cylinders was also limited.

Figure 30. MBB bean loaded in three-point bending fixture and imaged with stationary camera. Speckle pattern can be observed on the surface of the bridge.

A speckle pattern was created by painting the surface of each part white with a thin layer of aerosol paint, then running a quick pass of black aerosol paint over the dried white surface to create an incomplete layer. This allowed for a uniform and random array of black dots on the white background across the surface of each part, making an easily identifiable pattern for the DIC software. Images were captured on a Nikon D7000 camera with a sampling rate of 0.1 Hz using a 105mm Sigma EX macro lens. An example of the speckle pattern and sample setup can be seen in the MBB bridge specimen shown in Figure 30. The camera is fixed where the viewing plane is parallel to the surface of the part and centered so that the part surface takes up the majority of the frame. The region of interest is defined as the maximum visible area of the part.

The open source 2D DIC software Ncorr v1.2.2 was used to produce the full-field displacement and strain measurements for this study [148]. Ncorr is operated entirely from Matlab and is applicable to a wide variety of experimental conditions. While vertical (v) and horizontal (u) displacements, along with ϵ_{xx}, ϵ_{yy}, and ϵ_{xy} strains were all captured for each time step of the test, only the v-displacements were used to evaluate the part performance. For each frame, the mean v-displacement was found, and plotted against the force at that time step divided by the mass of the part. The slope of the line produced by this normalized force-displacement curve was taken as the part specific stiffness in this study.

4.2.2 Optimization

The present paper uses the framework proposed by the authors [143] to perform a two-level optimization of three benchmark designs. The optimum material distribution was obtained using Solid Orthotropic Material with Penalization (SOMP) or Level-set topology optimization methods. Kuhn-Tucker optimality criteria was used with SOMP, which is an energy-based optimization method translated by the following formulation:

$$\left.\begin{array}{l} \textit{minimize: } J(x,\theta) = \sum_{i\epsilon N_e}\left[E_{min} + x_e^p(E_0 - E_{min})\right]u_e^T k_\theta^e u_e \\ \\ \textit{subjected to: } \begin{cases} KU = F \\ \dfrac{V(x)}{V} = f \\ x\,\epsilon\,[0,1], \qquad \theta\,\epsilon\left[-\frac{\pi}{2},\frac{\pi}{2}\right] \end{cases} \end{array}\right\} \quad (5)$$

where the density (x) and fiber angle (θ_e) of each element of the mesh are the design variables and compliance ($J(\Omega)$) is the objective function. The volume is constrained and the penalization p is imposed to lead the density of elements to either 0 or 1, i.e., void or solid. u_e and k_θ^e are the element displacement and stiffness matrices, respectively. E_0, K, U, F, $V(x)$, V and f are the material matrix, global stiffness matrix, global displacement, force vector, volume of solid region, domain volume and volume fraction, respectively. E_{min} is a small value ($\sim 10^{-9}$) to avoid singularity in the void regions. N_e is a set of elements. The variation of the fiber orientation is accounted for in the element stiffness matrix k_θ^e, which is defined as:

$$\left.\begin{array}{l} k_\theta^e = \iint tB^T T^{-1} C T^{-T} d\Omega \\ \\ C = \begin{bmatrix} \dfrac{\mathrm{E}_1}{1-\nu_{12}\,\nu_{21}} & \dfrac{\nu_{12}\,\mathrm{E}_2}{1-\nu_{12}\,\nu_{21}} & 0 \\ \dfrac{\nu_{21}\,\mathrm{E}_1}{1-\nu_{12}\,\nu_{21}} & \dfrac{\mathrm{E}_2}{1-\nu_{12}\,\nu_{21}} & 0 \\ 0 & 0 & \mathrm{G}_{12} \end{bmatrix} \qquad T = \begin{bmatrix} \cos^2\theta & \sin^2\theta & 2\cos\theta\sin\theta \\ \sin^2\theta & \cos^2\theta & -2\cos\theta\sin\theta \\ -\cos\theta\sin\theta & \cos\theta\sin\theta & \cos^2\theta - \sin^2\theta \end{bmatrix} \end{array}\right\} \quad (6)$$

Where E_1 and E_2 are the Young's moduli of the material in the fiber and transverse directions, respectively; G_{12} is the shear modulus; and ν_{21} and ν_{12} are the Poisson's ratios.

At the end of the optimization, the fibers are generated according to the offset method or the equally spaced (EQS) method. In the offset method, the fibers are placed parallel to the boundaries of the model and at an equal set distance from each other. A positive value is assigned to the elements with non-zero density and a negative value to the remaining densities. The code generates a line parallel to the boundaries of the structure and at a predefined distance. Subsequent lines are individually generated in a similar fashion at a constant distance from adjacent lines until the structure is completely filled with non-intersecting lines. The trajectory at each point of the line determines the orientation vector which is interpolated to align the fiber orientation.

The EQS method creates equally spaced fibers parallel to the boundaries of the model starting at the constraints and spanning along the length of the model. Sections along the transverse direction of the structure and at a varying distance from each other are created. Those sections along the cross-section are divided into points which when connected along the longitudinal direction of the part form the fiber lines. The fiber path is defined by the interpolation of the angles at each element. The EQS method usually generates smoother fibers than the offset method but it is less robust than the offset approach, and therefore is appropriate for less complex topologies only.

On the other hand, the level-set method starts with an initial mesh and shape and evolves the boundaries using shape derivatives to minimize the objective function, i.e., the compliance in this study. At the end of each iteration of the level-set optimization, fibers are created according to the offset method.

Three major manufacturing constraints have been considered in the post-optimization stage: a) the printed filament paths used have a width of 0.9 mm; b) fibers should not be less than 45 mm

for the nozzle to properly extrude properly without resulting in a jam; and c) the closed optimized fiber paths need to be modified into continuous loops of several fibers making the printing process more faster, easier and reliable. In addition to these manufacturing limitations, variations between the experimental and model constraints as well as force applications are present. In the optimization, the constraints and loads are applied to the edge of each part, which is not practical in the experimental testing. This difference is most significant for the cantilever and L-shape bracket parts, which require additional holes and fasteners to be mounted to the testing apparatus.

4.2.3 Finite element analysis (FEA)

A framework was developed to perform the FEA of continuous fiber composites[68]. A triangular mesh using TRIA3 shell elements for a given geometry with the specified material properties, forces and constraints was created. Modeling these continuous fiber composite structures in a finite element software using the software graphical user interface is unfeasible and cumbersome since the fibers are not unidirectional and their orientation, and thus, the composite stiffness, changes from one element to another. Therefore, each element is individually modeled in the developed framework as a composite with the material orientation parallel to that of the fiber closest to the center of the element. Unless otherwise stated, all models are made entirely based on the material properties presented in Table 3; i.e., 34% carbon fiber in a nylon matrix.

Table 3 Material properties of carbon fiber composite

E_1	50.0 GPa
E_2	4.0 GPa
G_{12}	2.0 GPa
ν_{12}	0.33
${\sigma_1}^T$	700.0 MPa
${\sigma_1}^C$	- 320.0 MPa
${\sigma_2}^T$	48.0 MPa
${\sigma_2}^C$	- 100.0 MPa
τ_{12}	73.0 MPa

4.3 Results and Discussion

In order to produce parts of sufficient quality for this experiment, a commercially available continuous carbon fiber printer (MarkTwo) was used as a benchmark for the modified printer. Flexural properties of parts printed on the retrofitted continuous fiber printer were measured and compared with those of parts printed on the MarkTwo. Identical filaments were used to manufacture both sets of parts. The characteristic stress-strain curves for the two sets of parts are illustrated in Figure 31.

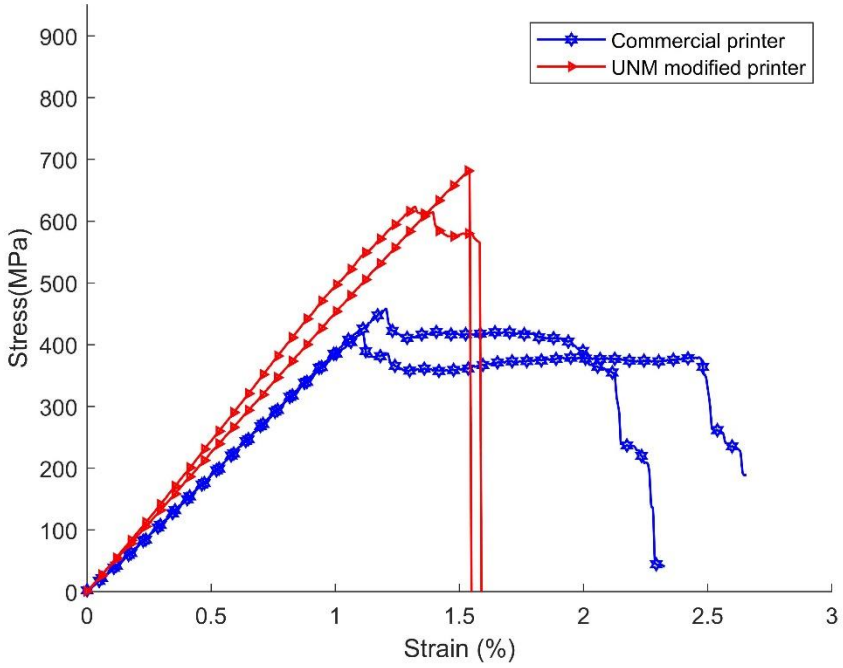

Figure 31. Flexural stress-strain curve of parts printed on the UNM modified continuous fiber printer and a commercially available continuous fiber printer.

It was found that the modified printer produced parts with an improvement in flexural strength and modulus of 55% and 19%, respectively, and also displaying an increase in the strain at onset of failure from approximately 1% to 1.5%. The parts printed on the commercial printer maintain their load-carrying capacity at higher strain values, as delamination between printed layers acts as stress relief. The interlaminar shear strength appears to be improved for the parts printed on the modified printer, which changes the failure mode from interlaminar to abrupt, as all layers fail together. As the maximum stress and strain at the onset of failure is most commonly used as design criteria, the part properties have indeed been improved by this manufacturing platform. Therefore, the optimized parts manufactured on the modified printer can be expected to have inter-filament bonding, interlayer bonding, and void content comparable with the current state of the art.

The cantilever beam studied by [143] was selected as the first case for the present study. The beam is subjected to a 10 KN point load at the middle of its free edge. SOMP was used to optimize the 200x100 element-rectangular domain shown in Figure 32, for a filtering radius of r_{min} = 6.0 and volume constraint of 55%. The filtering radius is the length scale control used to eliminate small members and checkerboard problem [143]. As shown in Figure 33, three configurations of the problem were considered: the non-optimized rectangular beam with unidirectional fibers along the horizontal direction, the optimized beam with EQS fibers and the optimized beam with offset fibers. The beams with EQS and unidirectional fibers have a 100% infill density, and the beam with offset fiber infill is only 83%.

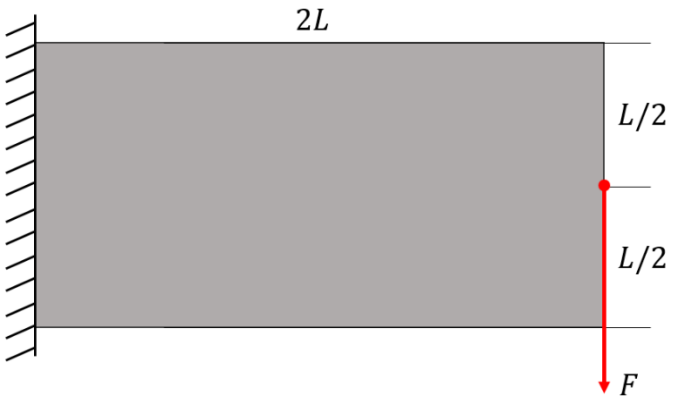

Figure 32. Original cantilever domain used for optimization.

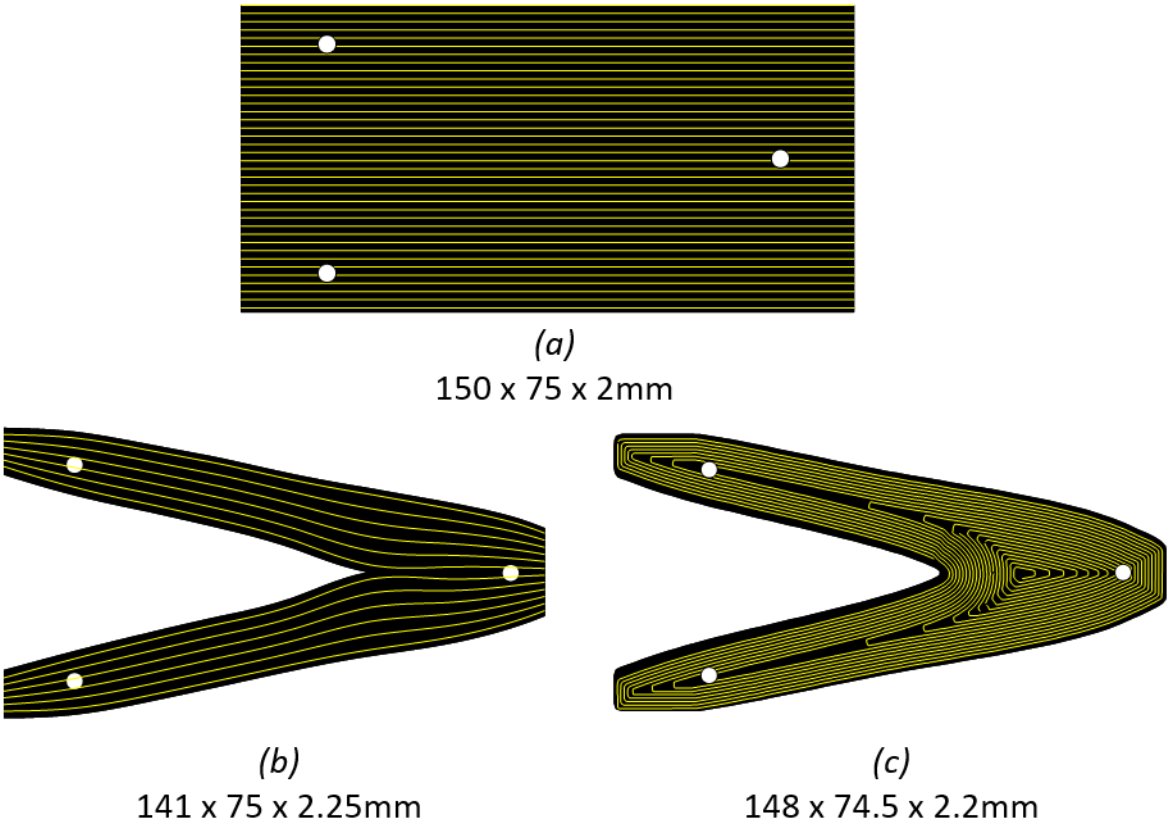

Figure 33. Fiber paths generated for non-optimized and optimized topologies: a) non-optimized beam with 0° unidirectional fibers; b) optimized beam with EQS fiber infill; and c) optimized beam with offset fiber infill.

Tamijani et al. has recently developed a method to identify load paths [149] and later implemented the concept in topology optimization [150]. Knowing how the load is transferred from point load application to the constraints of structure reveal the efficient use of material to increase the structural functionality. The optimization load paths in x and y directions, ψ_x and ψ_y, represented by the red lines in Figure 34 was analyzed to understand the obtained optimized

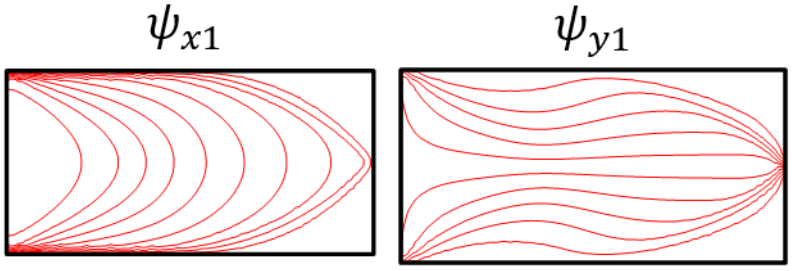

Figure 34. Initial load path before optimization of isotropic cantilever beam [1].

topology using SOMP. Although the presented load paths are for isotropic materials, it can be observed upon comparison of Figure 33 and Figure 34 that the regions with no load transferring, such as the far right top and bottom corner corners of the beam and the middle of the built-in edge, are removed during optimization, since they do not contribute to the load bearing capacity and only add weight to the structure.

The manufactured parts can be seen in Figure 35, along with the full-field vertical displacement as found through DIC. Table 4 shows the experimental and computation stiffness for the cantilever. A good agreement is observed between the experimental and computational results for the stiffness per mass or specific stiffness of the structure. The small difference between

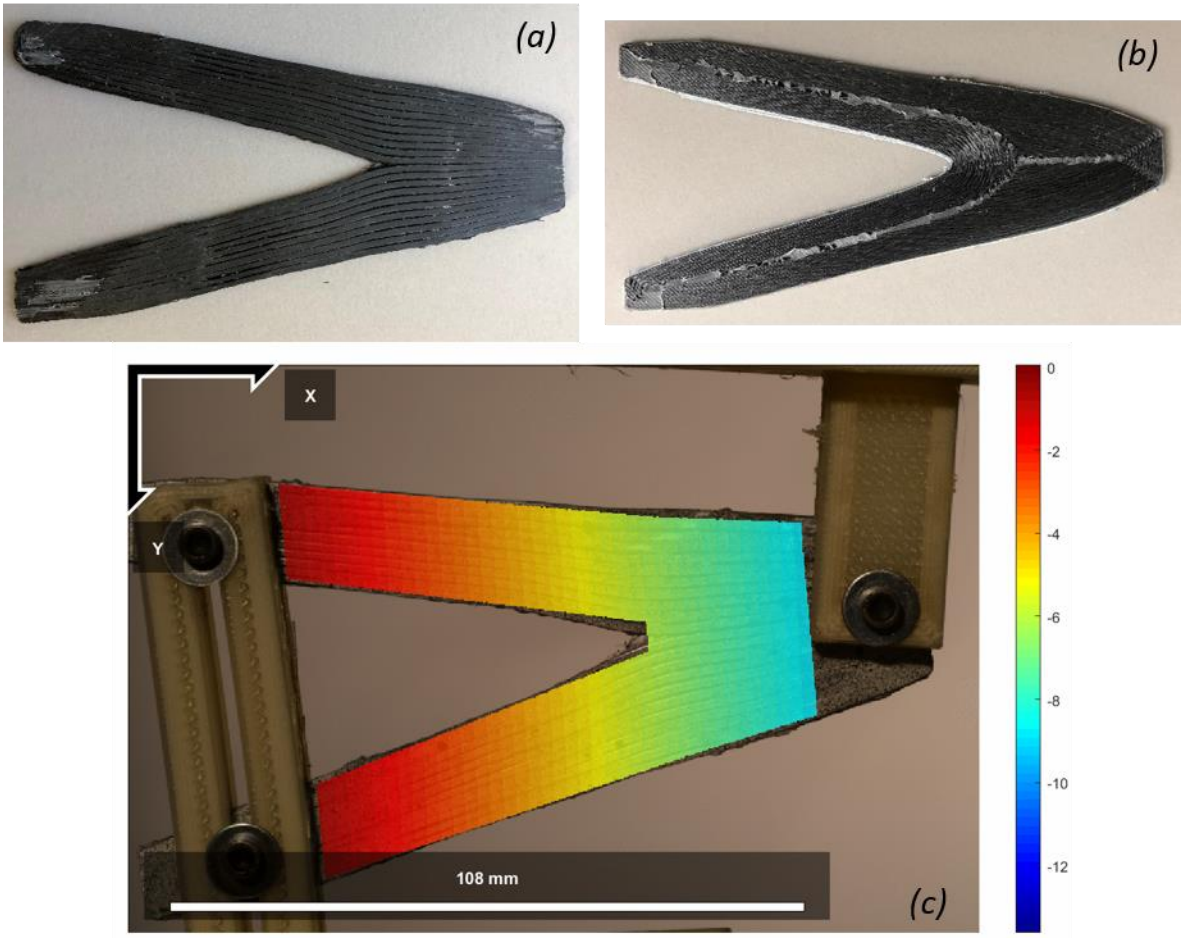

Figure 35. Manufactured EQS (a) and offset (b) continuous carbon fiber composite parts. The full-field vertical displacement DIC results are shown over the EQS composite during testing. Units are in mm.

results might be caused by the fact that the fixtures used to fix the beam were not rigid enough allowing a small rotation at a certain point of the experiment. This was a result of the glass fiber composite clamps that were used to fix the part to the load frame. All cantilever beam tests will be repeated with more rigid steel clamps to note any differences in the analysis, results for which are intended to be released at a later date. The optimized structure was found to be 53% stiffer than the non-optimized one. The orientation of the EQS fibers at the fixed connection allows the fibers to transfer the load from the point of its application to the constraints more efficiently than the offset fibers, which are perpendicular to fixed connection. Since fibers are designed to carry loads in the longitudinal direction, along its highest strength, EQS fiber reinforced model is 42% stiffer than the offset fiber reinforced part.

Table 4 Specific stiffness for the three cantilever beams in study. Model numbers are based on Figure 33.

Model	**Experimental Specific Stiffness ($N/g \cdot mm$)**	**Computational Specific Stiffness ($N/g \cdot mm$)**	**% Difference**
(a)	1.545	1.510	2.32
(b)	3.379	3.561	5.25
(c)	2.372	2.342	1.26

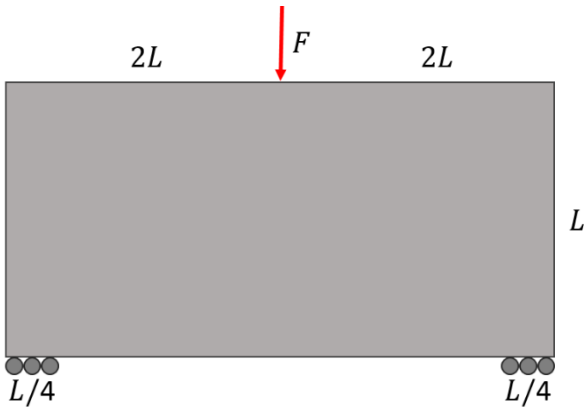

Figure 36. Original optimization domain for the bridge case.

The second benchmark design, the bridge, was obtained by the level-set optimization of the domain shown in Figure 36. The 5.13 mm-thick beam with roller supports was subjected to a point load in the middle of the top edge. The level-set optimization was performed for 400x100 elements with a 10 KN load applied and the optimized model in Figure 37a was obtained after 151 iterations, resulting in a 43% infill density. Level set/offset yields a MBB beam with the highest stiffness when compared to other methods such as EQS [143] due to the fact that level

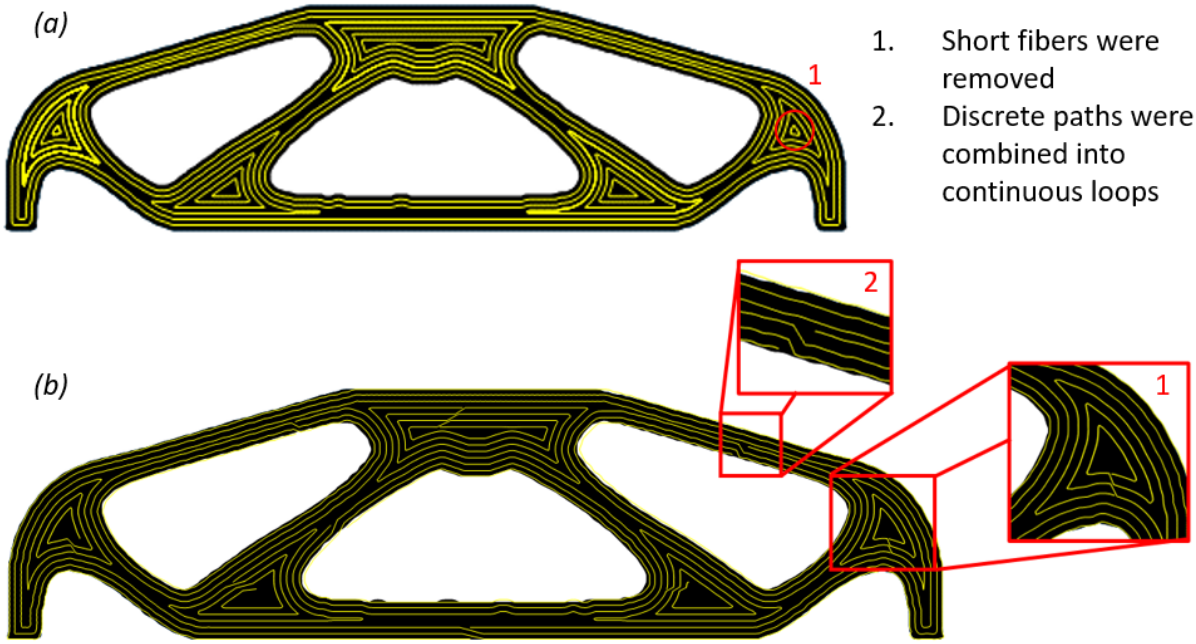

Figure 37. Optimized bridge model: (a) without and (b) with manufacturing constraints.

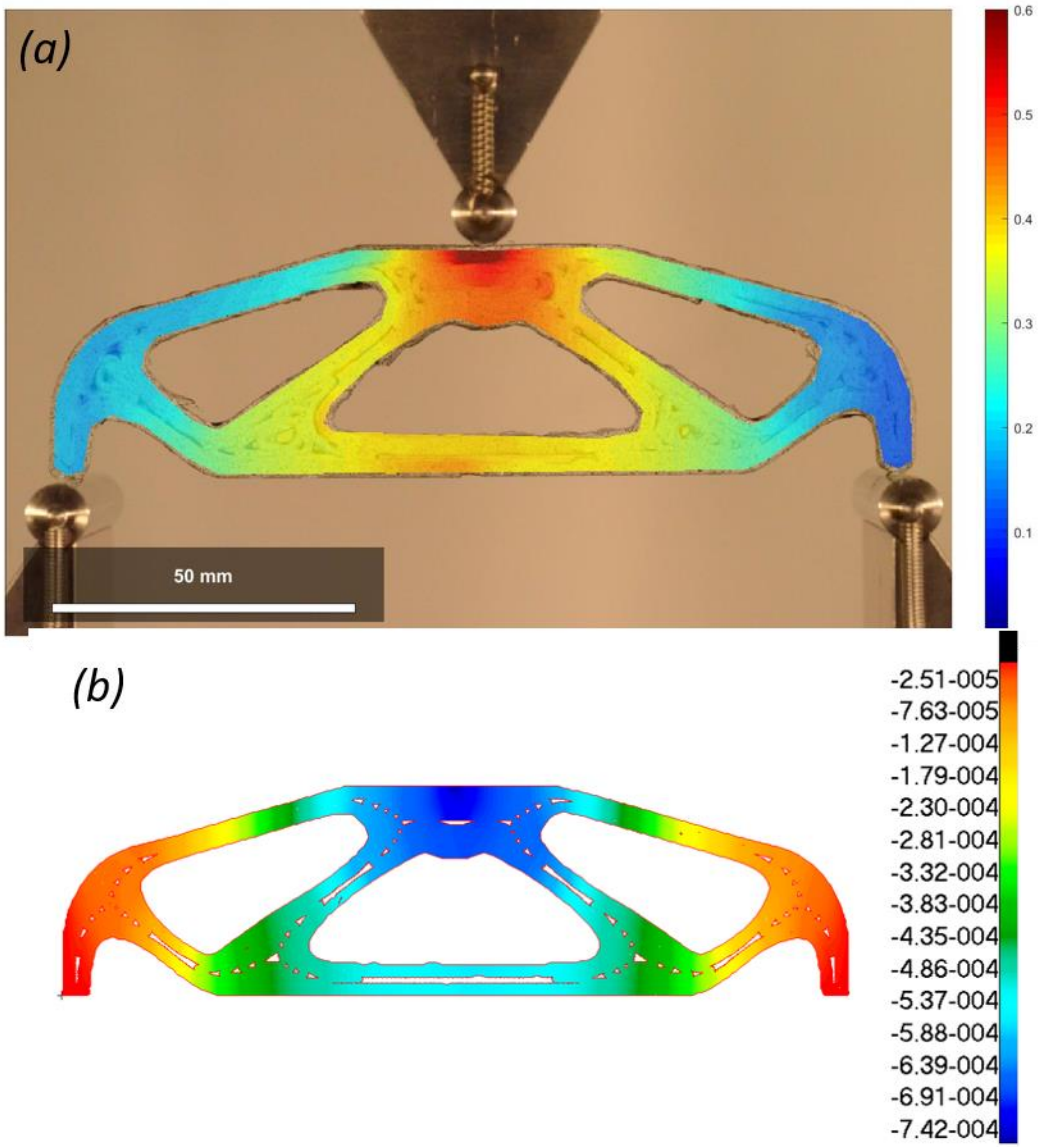

Figure 38. Vertical component of displacement: a) obtained from DIC (mm) and b) from FEA (m).

set/offset fills out 100% of the optimized part with fibers placed around the inner and outer edges and reinforcing the boundaries.

The structure was subjected to a 3-point bending test. The experimental and computational results are shown in Figure 38a and b and compared with each other in Figure 39. The results are

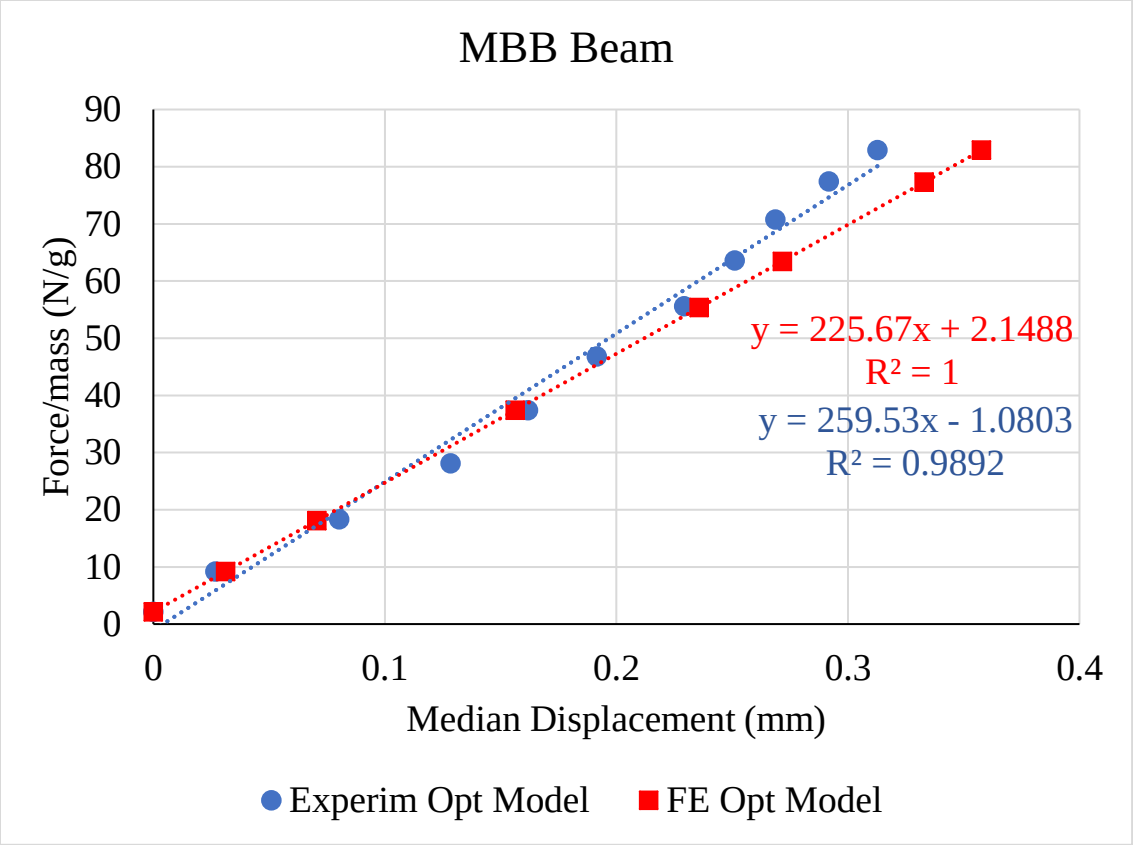

Figure 39. Specific force vs. median vertical displacement for bridge experimental model and finite element model.

in agreement, with the printed model being slightly stiffer than predicted. The 14% difference might be caused by discrepancies between the designed model and the actual printed model. To elaborate, comparing Figure 37a and b, it is visible that the sharp corners in the computational model are printed slightly rounded due to the capabilities of the printer nozzle which cannot handle such abrupt change in the fiber path.

Although the fibers are at 0.9 mm distance from each other, the fiber infill in Figure 37a is still not printable. The model in Figure 37b is obtained upon implementation of the manufacturing constraints. Short fibers which would require the nozzle to perform very tight turns were removed. The remaining ones were grouped together with adjacent fibers in which each group of fibers is made a single continuous fiber path. The optimized model was found to improve the

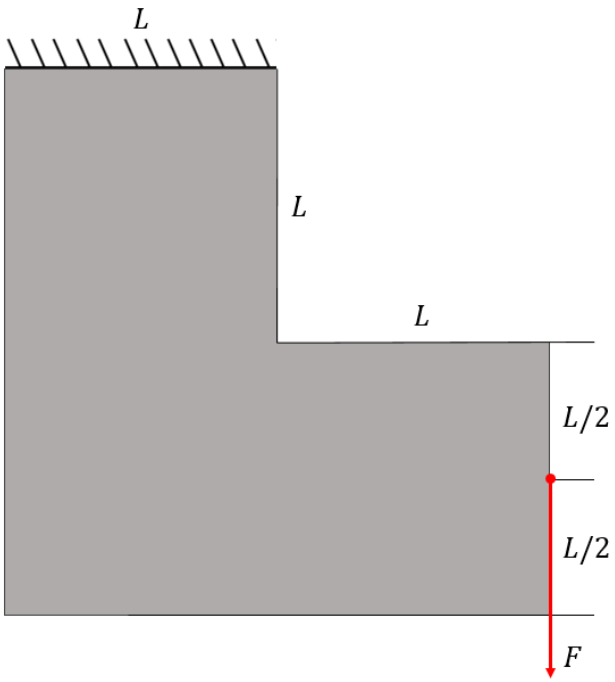

Figure 40. Original optimization domain for the L-bracket.

specific stiffness over the non-optimized unidirectional model (horizontally unidirectional fibers) by 37%, based on the simulated non-optimized results.

The L-bracket was selected as the last case study. The level-set optimization of the domain in Figure 40 for 200x200 elements, 5.09 mm thickness and 11KN vertical load resulted in the model shown in Figure 41. Level-set and offset methods were selected for this case study since they originate one of the stiffest layouts for this problem when compared to SOMP combined with EQS and other methods discussed by Papapetrou, Patel [143]. In fact, when compared to other methods for the L-bracket, level-set/offset is the only method capable of filling out 100% of the domain with continuous fibers reinforcing the inner and outer boundaries without generating voids [143].

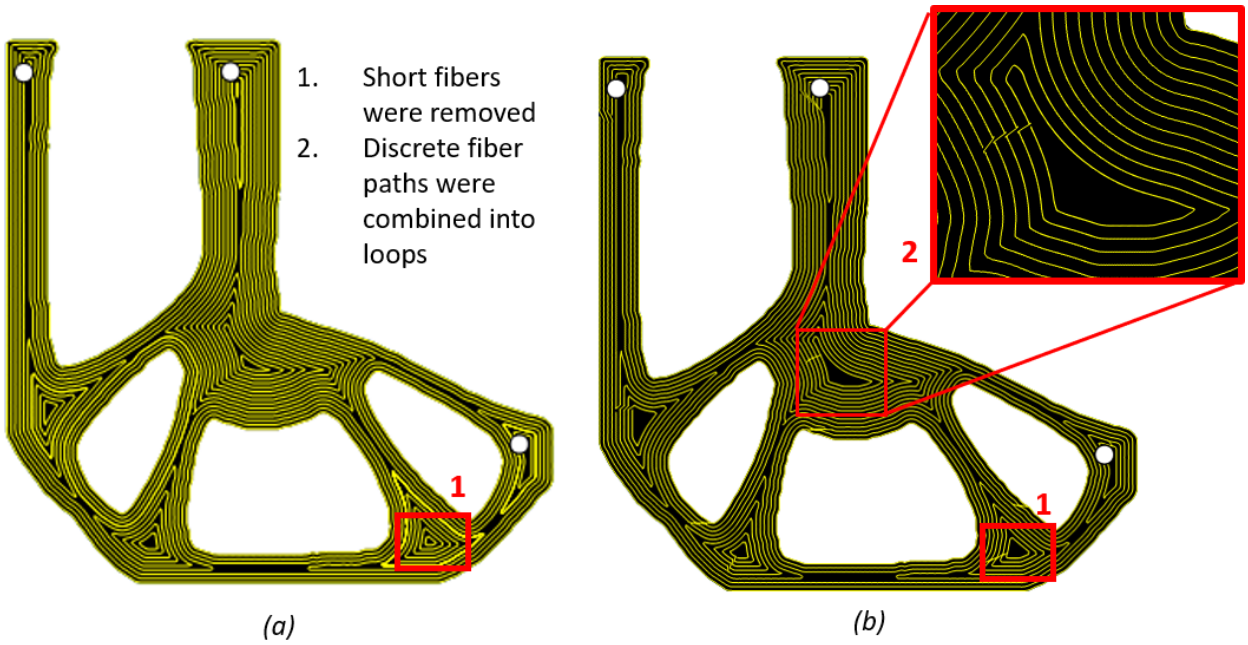

Figure 41. L-bracket optimized using Level-set and with offset fibers: (a) without and (b) with manufacturing constraints.

After 251 total number of iterations for a 37% infill of the initial domain, the optimized model was obtained. The optimized load paths in Figure 42 verify the general shape of the optimized model seen in Figure 42 using level set/offset.

The L-bracket was printed and tested, as seen in Figure 43. The results for both computational and experimental analyses are compared in Figure 44, which shows a good agreement with only 3.34% difference in specific stiffness. Similar to the bridge, the printer rounds some of the sharp edges defined in the model. In this experiment, the force-displacement curve showed the largest amount of noise, giving the lowest R^2 value fitting the data with a linear curve. This could be due to microcracking at filament interfaces, though further investigation will be required to fully understand this behavior. The non-optimized part was considered to be a stacked composite layup, with fibers oriented in a symmetric [+45,-45] stacking sequence. The optimized geometry was found to improve the specific stiffness by 245% over the simulated properties of the reference geometry.

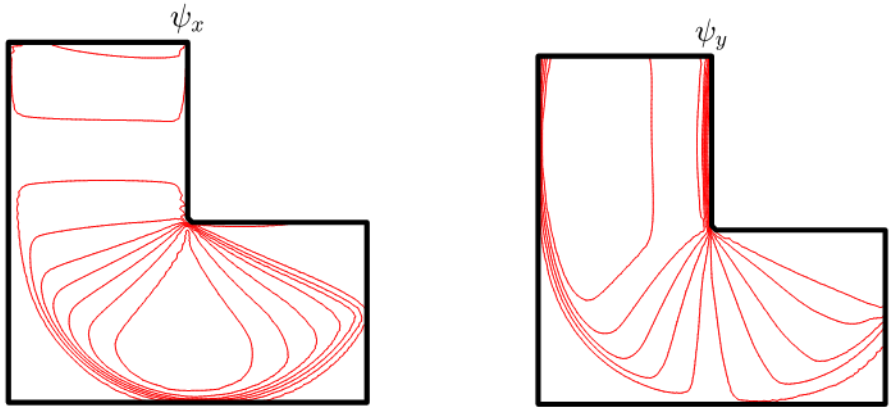

Figure 42. Initial Load paths before optimization for L-bracket [1]

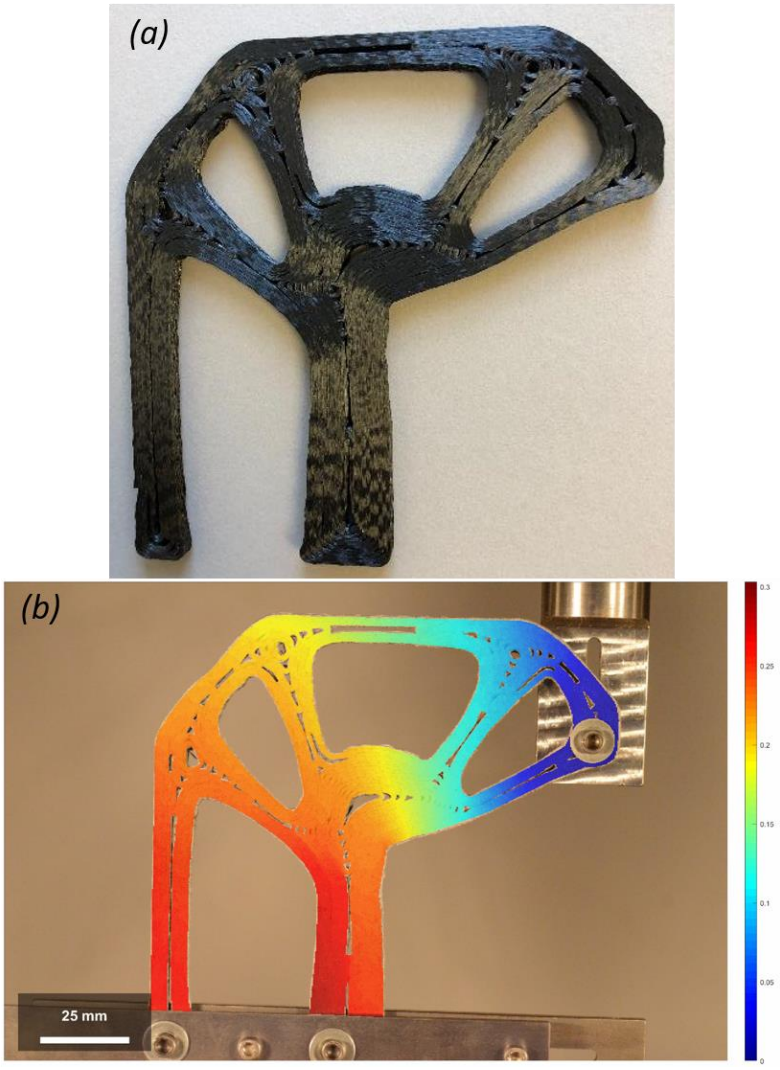

Figure 43. Printed L-shape bracket (a) and DIC results of vertical displacement of L-shape bracket under loading (b).

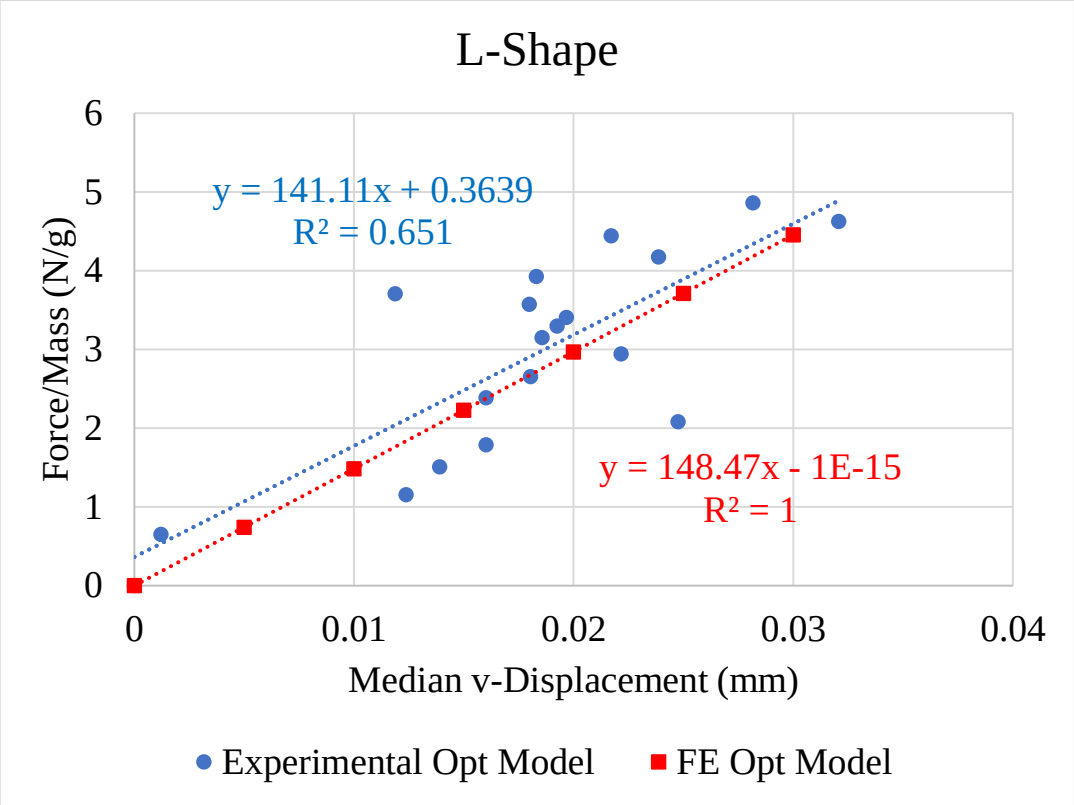

Figure 44. Specific force vs. y-displacement for L-bracket experimental model and finite element model with manufacturing constraints.

A summary of the experimental and computational results is shown in Table 5. In general, the computational specific stiffness is in relatively close agreement with the experimental specific stiffness. The largest difference between experimental and computation values was observed for the MBB beam, with a difference of 15.01%. This could be due to the flawed interfaces between the printed filaments, resulting in incomplete load transfer between the fibers. The non-optimized cantilever was found to have the closest agreement between the computational and experimental results, with a difference in specific stiffness of only 4.77%. Each optimized design produced a significant improvement in specific stiffness, with an improvement of up to 245% in the case of the L-bracket. A minimum improvement of 37% was found for the optimized MBB beam. The optimized specific stiffness was compared with experimental non-optimized stiffness in the

cantilever case, and against simulated non-optimized specific stiffness in the MBB beam and L-bracket cases.

Table 5. Experimental and computational specific stiffness of the tested benchmark specimens.

Description	Experimental Specific Stiffness	Computational Specific Stiffness	% Difference	% Improvement Over Non-optimized Model
Cantilever beam with 0° unidirectional fibers	1.582	1.510	4.77	0
Offset optimized cantilever beam	2.380	2.728	-12.75	79
EQS optimized cantilever beam	3.836	3.561	7.72	142
MBB beam	259.53	225.65	15.01	37
L-shape	141.11	145.83	3.34	245

4.4 Conclusions

Topology optimization was applied to three benchmark geometries to improve the specific stiffness of parts manufactured using continuous carbon fiber FFF. The fiber paths generated for an optimized cantilever, L-shape bracket, and MBB beam were manufactured using a modified commercial FFF printer. The composites were characterized using digital image correlation, and the computational specific stiffness was compared with the experimental results. The suitability of the optimization methods depends on the problem; however, the offset method often lead to better results since it assumes fibers parallel to the boundary of the layout and often along the principal stress direction. In general, the computation results agreed closely with the experimental results, with a maximum difference occurring for the MBB beam at 15%. The optimized specific stiffnesses were then compared with non-optimized geometries and fiber orientations. The non-optimized specific stiffness was tested experimentally for the cantilever and simulated for the MBB beam and L-bracket. The cantilever, MBB beam, and L-shape

bracket were found to improve by up to 142%, 37%, and 245% when optimized compared with the respective reference geometries.

Chapter 5. Investigating the Hot Isostatic Pressing of an Additively Manufactured Continuous Carbon Fiber Reinforced PEEK Composite

Nekoda van de Werken [a], Pratik Koirala[b], Jafar Ghorbani[a], Derek Doyle[c], and Mehran Tehrani[a,b]

[a] Department of Mechanical Engineering, University of New Mexico, Albuquerque, NM, United States

[b] Walker Department of Mechanical Engineering, University of Texas, Austin, TX, United States

[c] Department of Electrical Engineering, University of New Mexico, Albuquerque, NM, United States

Fused filament fabrication (FFF) has recently begun to explore its role in the composites industry, utilizing the capability of complex fiber placement and part geometry to further reduce the weight of composite structures. Additively manufactured (AM) continuous fiber composites, however, suffer weak interlayer bonding and high void contents. This study investigates the use of hot isostatic pressing (HIP) to post-process AM continuous carbon fiber reinforced polyetheretherketone (PEEK) composites to improve their flexural, interlaminar shear, tensile, and compressive properties. Isostatic pressure and elevated temperatures were used in combination to compress internal voids, promote PEEK crystallization, and cause inter-filament polymer diffusion. The post-processing was able to significantly improve all tested properties, with tensile strength and stiffness of 1312 MPa and 92 GPa, respectively; highest reported for AM composites to date. The accompanying changes in void content and polymer structure for various HIP processing parameters were investigated to account for the changes in measured mechanical properties. Specifically, it is shown that role of PEEK crystallinity on interlaminar properties of AM composites was escalated due to the presence of voids. HIP demonstrates a fast

and robust method to post-process FFF AM parts, resulting in a significant improvement in mechanical performance.

Keywords: Additive manufacturing; fused filament fabrication; continuous carbon fiber; PEEK; mechanical properties; hot isostatic pressing

5.1 Introduction

Carbon fiber composites have become integral to high-performance markets where mass savings are critical. Some examples include the aerospace, energy, and automotive industry. While the investigation into additively manufactured (AM) continuous carbon fiber reinforced polymer composites (CCFRP) has only begun recently, they offer a few notable advantages over conventional composite processing methods [21, 131]. Additive manufacturing can eliminate the need for molds, produce parts with higher geometric complexity, and provide optimized fiber placement and orientation for improved specific (per weight) properties. These advantages are essential for implementation of AM composites in high value applications, which require very high specific strength and stiffness. Before AM CCFRPs are found suitable for high value applications, a few limiting factors need to be addressed.

Currently, the most common method for AM of composites is fused filament fabrication (FFF), which can be used to manufacture either short or continuous fiber composites with a thermoplastic matrix [131]. In FFF, a polymer filament is fed through a heated nozzle to extrude a molten polymer bead, which deposits the material in plane and builds the part layer-by-layer. Short fiber composites are most commonly produced by mixing chopped fibers and polymer pellets or powder in a hopper before filament extrusion, and extruding the short fiber composite filament to a spool [5]. This material is then fed into a standard 3D printer to manufacture a composite part in the same way as an unfilled polymer part, however, resulting in only slight

improvements over the polymer matrix. The performance of these composites is severely limited by the short length of the fibers, which are typically only a few hundred microns long and limited by the nozzle diameter of the printer to prevent jams [5]. The maximum fiber volume fraction possible in short fiber composites is also reduced, as increasing the fiber filler fraction above 20% offers significantly diminished returns due to elevated void content and a reduction in average fiber length [23].

The use of continuous carbon fiber reinforcement has been found to produce AM composites with significantly improved properties over those of short fiber composites [21]. In a recent review of AM composites, it was found that the maximum tensile strength and stiffness reported for short fiber composites loaded in the fiber direction was 125.3 MPa and 26.4 GPa, respectively, while the maximum tensile strength and stiffness of continuous fiber AM composites loaded in the fiber direction was 464 MPa and 35.7 GPa, respectively [21]. Continuous fibers are most commonly incorporated through the use of thermoplastic composite filaments [69, 70, 85] or in-nozzle, impregnation [71, 74, 151, 152]. Composite filaments are manufactured by infusing the fiber tow with a thermoplastic matrix prior to manufacturing and feeding the filament into a 3D printer. In-nozzle impregnation involves feeding the fiber tow directly into the printer hot-end, where it is infused with the tow and extruded. In both cases a mechanism is required to cut the fibers at desired locations.

Continuous fiber composites in the form of tapes can also be additively manufactured through processes such as automated tape laying (ATL) or automated fiber placement (AFP), which shares many similarities with FFF [153, 154]. In-situ tape consolidation in AFP or ATL is ensured through the use of a roller to apply pressure while heat is delivered through a source, ensuring the formation of strong interlayer bonding and low void contents. These manufacturing

methods, similar to FFF, seek an automated and out-of-autoclave solution to composite manufacturing, and allow for processing of high-performance thermoplastic matrix composites. ATL and AFP, in contrast to AM, do require molds and typically build parts of uniform thickness rather than building up complex 3D geometries. Moreover, fiber steering in AFP is not as trivial as it is for FFF, thereby limiting the design freedom in these techniques.

Implementation of continuous fiber composites has largely been achieved using thermoplastics such as polylactic acid (PLA), acrylonitrile butadiene styrene (ABS), and nylon [21]. While these materials are common in FFF due to their price and ease of printing, high performance polymers are required for high value applications where higher service temperatures, chemical resistance, radiation resistance, or mechanical properties are required. Polyether ether ketone (PEEK), polyether ketone ketone (PEKK), polyphenylene sulfide (PPS), and polyetherimide (PEI) have all been identified as suitable polymers for high performance applications.

Many of the thermal, transverse, interlaminar, and shear properties are dominated by the polymer matrix and fiber-matrix interface. Additionally, the response of a polymer to various elements of its environment, such as humidity, radiation, voltage, or exposure to chemical solvents, will define the appropriate operating conditions for the composite. For aerospace and defense applications, only high-performance polymers are suitable. As such, polyether ether ketone (PEEK) has been identified as a space-rated thermoplastic, and therefore is the focus of a material science investigation in the scope of this dissertation [155]. The repeat unit for PEEK is shown in Figure 45.

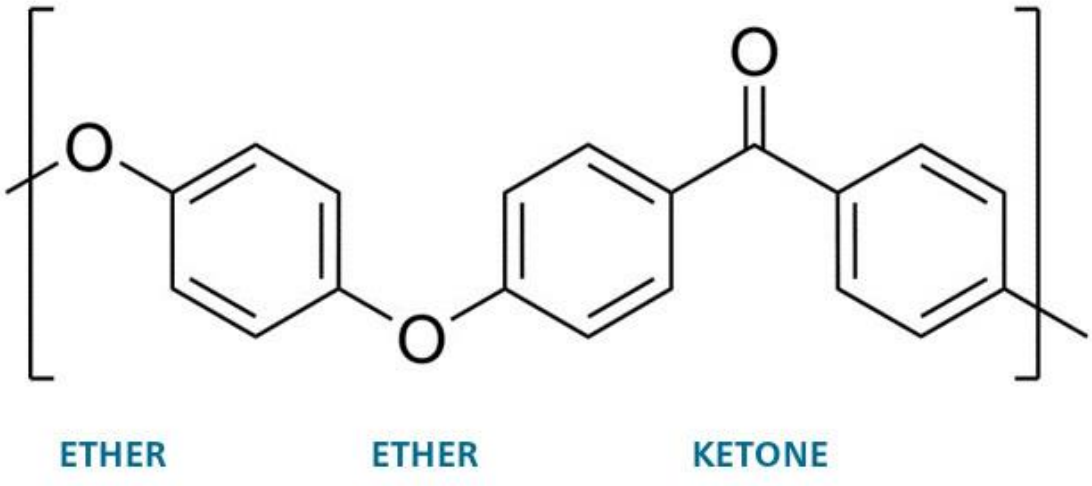

Figure 45. Repeat unit of polyether ether ketone (PEEK) [4]

As a semi-crystalline thermoplastic, the microstructure of PEEK is largely dependent on the thermal and mechanical history of the material. The time spent in melt, cooling rate from melt, annealing conditions, and plastic deformation are the largest contributing factors to the crystalline structure of the polymer [156-166]. The type of reinforcement in PEEK matrix composites also influence the degree and morphology of crystallinity, as the foreign surfaces can act as heterogeneous nucleation sites to encourage transcrystallinity [167]. While many traditional composite manufacturing methods, such as compression molding, allow for control over the thermal history through the use of heated molds and injection rates, the control over thermal conditions in additive manufacturing is much more limited. Control over the time in melt is possible by tuning the print speed to achieve a desired time of the polymer in the printer hot-end, though this parameter is directly related to the manufacturing time and therefore cannot be defined without compromise. The cooling rate is also tied to geometric tolerances, bed and chamber temperatures, and air quenching is typically needed to solidify the polymer in place form melt to prevent sagging or drooping during a print. The relatively short time in melt and

high cooling rates can result in low polymer crystallinity, which can influence the mechanical performance of the composite.

AM composite manufacturing based on FFF commonly exhibits high void content, based on the packing of liquid polymer beads together [23, 168]. This typically results in higher void content at the inter-filament and inter-layer interfaces in a composite [169]. Adding a reinforcement material can lead to voids in the filament and further increase the composite void volume fraction [23, 170]. The influence of voids on CFRP properties has been studied extensively, which is particularly relevant to AM CFRPs as the void content is inherently high. The mechanical properties most deteriorated by void content in composites are inter-laminar shear, compression, transverse tensile strength, and fatigue life, which can decrease by up to 10% for 1% additional void content [171]. In the case of flexural loading in CFRPs, the flexural modulus was also found to decrease by 5-10% per 1% increase in void volume fraction [171]. The void morphology and connectivity also have a significant impact on composite properties [169, 171]. Hart et al. found that annealing of additively manufactured acrylonitrile butadiene styrene (ABS) resulted in the restructuring and coalescence of voids, effectively blunting them and altering the efficiency for crack propagation through the material, leading to an increase in fracture toughness [169].

This study aims to investigate the use of hot isostatic pressing (HIP) to address three areas of ultra-high performance additively manufactured continuous carbon fiber reinforced PEEK composites: void content, degree and morphology of crystallinity, and inter-filament polymer diffusion. HIP is a treatment process which utilizes elevated temperature and isostatic pressure inside a vessel to enforce internal restructuring of a material. HIP is widely used to reduce porosity in metals and ceramics. In the case of AM continuous fiber composites, elevating the

temperature above the polymer glass transition temperature (T_g) can be used to increase polymer chain mobility and soften the matrix, a requirement for polymer diffusion at the interfaces. The use of external pressure is intended to compress the internal voids and possibly promote diffusion of polymer chains across void boundaries for a permanent restructuring and consolidation of the void content. Additionally, treating the part at temperatures above the cold crystallization temperature of the polymer can lead to changes in the degree of crystallinity and crystalline structure of the polymer, which can be chosen to tailor the overall mechanical performance of the composite; usually a high crystallinity is required for higher fiber-polymer adhesion and chemical resistance, while lower crystallinity improves interlaminar fracture toughness [157, 172]. Lastly, the rapid deposition and air quenching of a polymer bead during manufacturing is not expected to allow for diffusion and entanglement of polymer chains across the filament interfaces. Specifically, the temperature of the top layer drops quickly below the T_g of the polymer (bed and chamber heating can be used to alleviate this), thus inhibiting polymer diffusion. Where the layer temperature is even above the T_g, usually the pressures and consolidation durations in AM are not high enough to achieve a perfect bonding. Post-processing the composite using HIP to allow for diffusion across the filament boundaries may improve the strength and stiffness of the interfaces, which commonly define the failure mode under complex states of stress. The changes in composite void content, crystallinity, and mechanical properties with respect to various HIP treatment conditions are investigated in this study.

5.2 Materials and methods

5.2.1 Materials

The AM CCFRP PEEK composites were manufactured by Mantis Composites, who provided details of the polymer, composite filament, and print conditions. The composite filament contained approximately 41-43 vol% AS4C carbon fiber, and the PEEK matrix was not modified for the manufacturing process. The composite filament cross-section, as observed with optical microscopy, can be seen in Figure 46. The filament diameter ranged from approximately 0.77 to 0.8mm, with a density varying from approximately 1.51 to 1.52g/cc. A nozzle setpoint of 415°C, bed setpoint of 200°C, and print speed of 80mm/min were used to manufacture the composite parts.

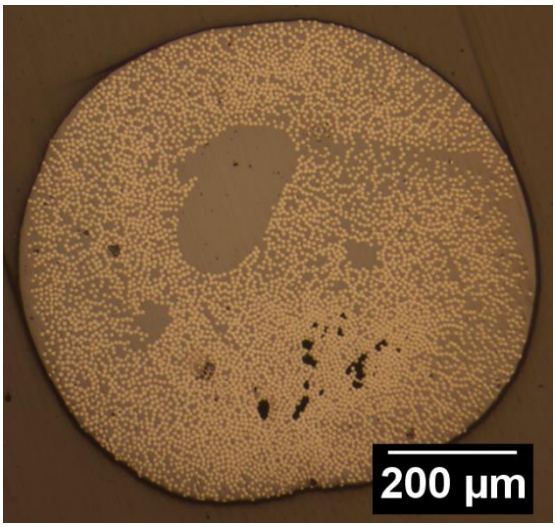

Figure 46. Cross-sectional optical micrograph of continuous carbon fiber reinforced PEEK filament. The fiber distribution, matrix rich regions, and voids can be observed.

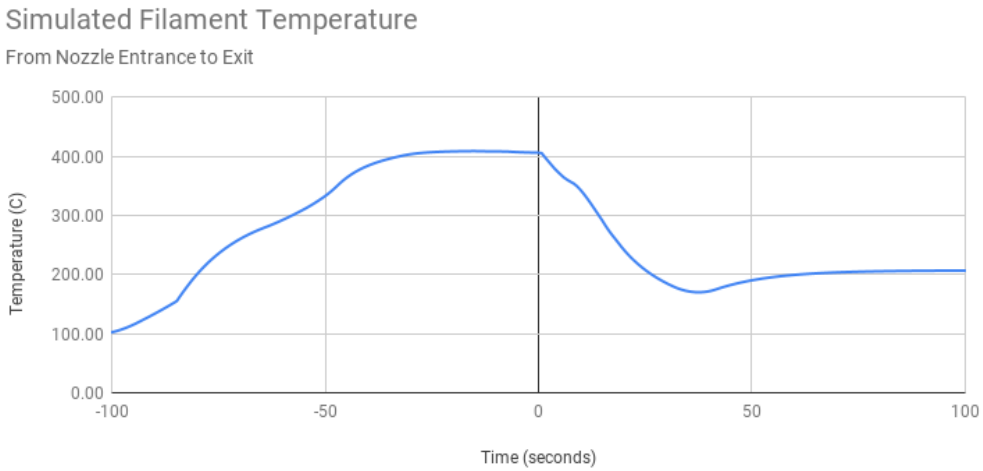

Figure 47. Simulated temperature of CCF PEEK filament as it is passed through the nozzle in the manufacturing process.

A simulation of the filament temperature of the filament as it is passed through the nozzle was performed, as seen in Figure 47. The time spend in melt, cooling rate, and ambient temperature are the parameters that have the maximum influence over the polymer microstructure in FFF. In this simulation, the filament temperature remains above 400°C for approximately 40s before extrusion from the nozzle. After extrusion, the temperature drops to 200°C in approximately 25s, resulting in a cooling rate of roughly 480°C/min. The filament temperature then equilibriates at the bed temperature of 200°C.

To observe the temperature response of the filament directly under the layer in which deposition occurs, a temperature sensor was embedded in the previous layer and laminated into the part in the printing process, results for which are shown in Figure 48. It can be seen that the deposition of a new layer of filament causes the previous layer to heat to over 300°C briefly, though the thermal energy added by the new layer is not sufficient to re-melt the previous layer. The temperature then asymptotes toward the bed temperature over the course of approximately 25s after deposition. These temperature time data can eventually be used to estimate the crystallinity of the AM composite.

5.2.2 Hot isostatic pressing (HIP)

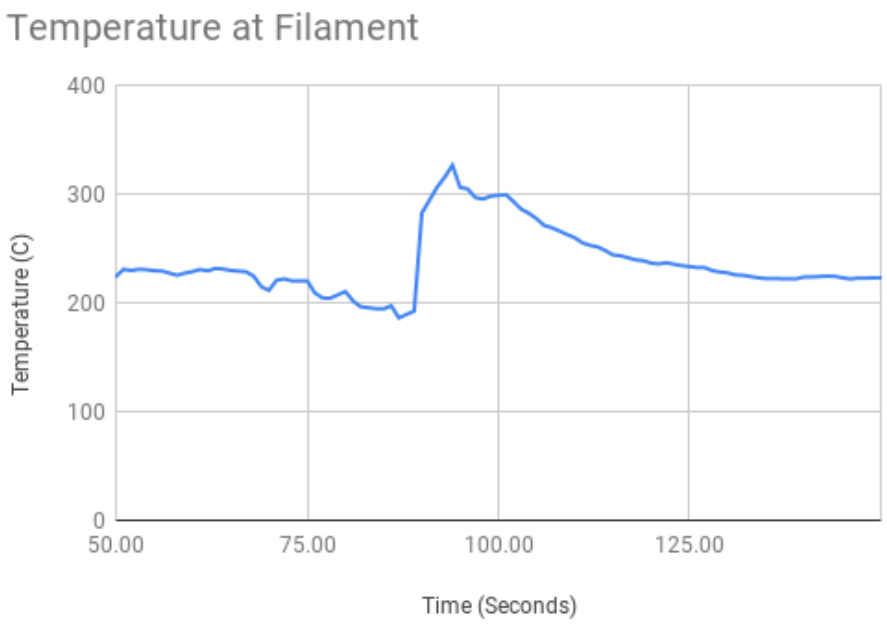

Figure 48. Temperature progression of filament directly under currently deposited layer.

HIP is often utilized to consolidate a part with high void content (porosity) by compressing voids and allowing for atomic or molecular diffusion to occur across the void boundaries. As the rate of diffusion is often proportional to temperature, the use of elevated temperature further enables

this mechanism, along with softening the material to allow for a more complete compression of the internal voids.

HIP was carried out on the AM CCFRPs using an autoclave. Nitrogen gas was used to pressurize the chamber to minimize oxidation of the polymer during treatment. In general, the parameters of interest during HIP treatment is temperature, pressure, and time. To isolate the influence of temperature on the process, the pressure and time were fixed at 200psi and 3hr, respectively, while temperatures of 200°C, 250°C, and 300°C were applied for individual treatments, all of which above the T_g of PEEK, i.e. 143°C. Further, the dependence of the processed composite properties on pressure was investigated by treating an additional sample at 250°C and 3hr, but at atmospheric pressure (~12psia). Lastly, the influence of treatment time on interlaminar shear strength (inter-layer polymer diffusion) was determined by treating a sample at 250°C, 200psi, for 24hr instead of 3hr. As it is expected that the mechanisms responsible for changes in material and part properties are dependent on polymer diffusion, a time of 24hr would represent the maximum change in microstructure that could be accomplished with this processing. A summary of these treatment conditions is shown in Table 6. It should be noted that the HIP (autoclave) process here didn't require bagging and vacuum application as used in conventional composite fabrication, therefore is applicable to treating complex part geometries.

Table 6. Summary of HIP parameters used for post-processing AMCCFRPs.

Sample	Temperat	Pressure	Time
Ref	Untreated	Untreated	Untreated
200C	200°C	200psi	3hr
250C	250°C	200psi	3hr
300C	300°C	200psi	3hr
Atm.	250°C	12psi	3hr
Ext.	250°C	200psi	24hr

5.2.3 Mechanical properties

The influence of post-processing treatment conditions on the mechanical properties of the composite was investigated through flexural, short beam shear (SBS), tensile, and compression testing. All specimens were tested on an MTS Bionix servo-hydraulic frame equipped with a 25kN load cell in accordance with their respective ASTM standards, with any deviations noted for a given test. An example of each sample geometry in their respective test fixture is shown in Figure 49. The flexural and interlaminar shear properties were investigated using a three-point bending test. A minimum of four samples of each geometry were tested due to a limitation in material access. As interlaminar and flexural properties are sensitive to void content and inter-filament bond strength, and are typically low in FFF materials, these properties were chosen to evaluate each configuration of post-processing parameters. SBS tests were performed on all HIP

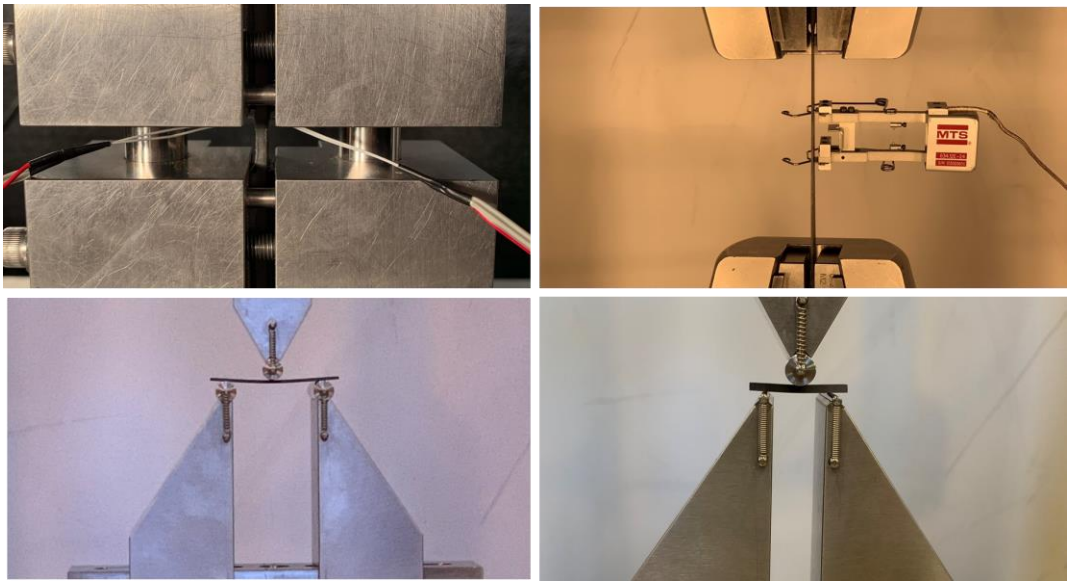

Figure 49. Clockwise from top left: Compression test setup, tensile test setup, short beam shear test setup, flexural test setup.

conditions listed in Table 6, and flexural tests were carried out on all samples except for Ext. Flexural specimens were manufactured and tested in accordance with ASTM D790-17, with a sample size of 1.5X13 X65mm and a fixture span of 48mm (span to thickness ratio of 32). The specimen was loaded under a constant crosshead displacement rate of 1mm/min until complete sample failure. SBS samples were prepared in accordance with ASTM D2344, with sample dimensions of 3 X13 X32mm. It should be noted that the 200C configuration was manufactured at 4 X13 X32mm, which deviates from the other specimen sizes but still falls within the ASTM standard recommendations. In each case, a span-to-thickness ratio of 6 was maintained to prevent crushing of the sample and ensure uniform shear stress distribution and interlaminar shear failure. Four samples of each configuration were tested, with a constant crosshead displacement rate of 1mm/min. In the flexural test, all cylinders in the test fixture were 10mm in diameter. In the SBS test, the loading cylinder had a diameter of 10mm, while the support cylinders had a diameter of 3mm.

Tensile testing was performed in accordance with ASTM D3039M-17. Unidirectional 0° samples with dimensions of 1 X13 X200mm were printed and tabbed on both sides. The G10 fiberglass tabs used had dimensions of 1.6 X13 X60mm, with a 7° taper to prevent stress concentration during the test. A constant crosshead displacement rate of 2mm/min was applied during the test, and an MTS extensometer of gauge length 25.4 mm was used to measure the material strain. The specimen was loaded to failure.

Compression testing was carried out in accordance with ASTM D6641. Unidirectional 0° coupons were printed with dimensions of 3X13X140mm. G10 fiberglass tabs were adhered to each side of the coupon, with dimensions of 1.3X13X63mm, creating a gauge length of 13mm. Two strain gauges, 10mm gauge length, were bonded to each side of the compression coupon. By comparing the values from each strain gauge, buckling of the composite during compression testing can be identified. A constant crosshead displacement rate 1.3 mm/min was applied until failure.

5.2.4 Scanning electron microscopy and optical microscopy

Scanning electron microscopy and optical microscopy were used to observe the composite cross-sections to observe void content, void structure, and homogeneity of fiber packing. Cross-sectional samples with carbon fibers perpendicular to the cut direction were prepared for microscopy. The samples were mounted in an acrylic mold, ground using silicon carbide paper up to a maximum grit of 1200. The sample surfaces were then polished using a 1µm diamond colloidal suspension and a 0.05µm silica colloidal suspension. The prepared cross-sections were coated with a few nanometers of gold before imaging with an FEI Quanta 3D FEG SEM. Optical microscopy was carried out with a metallurgical microscope with objectives between 10 X and 50X magnifications.

5.2.5 Micro-computed tomography (μCT)

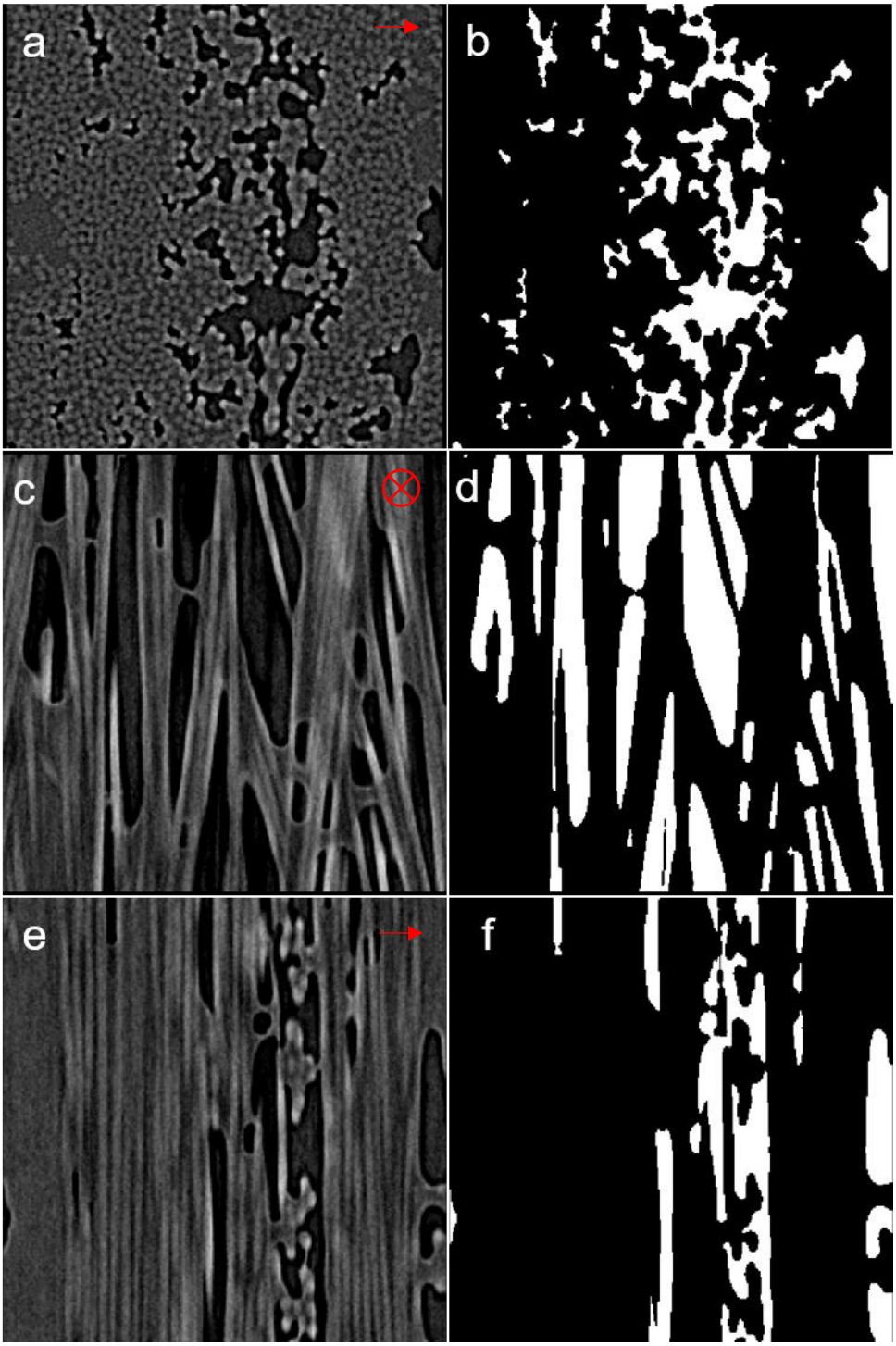

Figure 50. Raw and processed images of an untreated AM CCFRP. Planes in a) and b) are orthogonal to the fiber direction, c) and d) are parallel to the print surface, and e) and f) are perpendicular to the planes in a) and c). Red arrows show printing (z) direction for each image pair.

Micro-computed tomography (μCT) was conducted to characterize the void content, fiber packing, and fiber orientation for each post-processing treatment. Ultrahigh resolution 1μm scans were used for analysis, covering a 1mm diameter of the cross-section and 1mm through the thickness, in which the cross-section is normal to the fiber direction.

Samples were prepared by sectioning an untested flexural coupon into an approximately 1 X1 X10 mm specimens using a high-speed precision saw. One scan was collected per specimen, and two specimens were prepared per treatment. Quantification of the void content was performed with the software Blob3D. The void content was analyzed by processing the images to isolate the void regions of each slice. An example of this image processing is shown in Figure 50, in which the voids in three orthogonal planes are illustrated. While slight noise can be observed, and some regions that can be identified as voids are not captured in the image processing, these are considered relatively small to the total void content. The same image processing conditions were used on all samples, as the same sample size and test conditions were used to capture the μ-CT data for each specimen.

5.2.6 Dynamic mechanical analysis (DMA)

A dynamic mechanical analysis (DMA) Q800 apparatus from TA Instruments was utilized for studying the effect of process parameters on glass transition temperature as well as storage modulus and damping. Specimens were prepared and tested in accordance with ASTM D7028, with dimensions of 56± 4 X12± 1X2.0 ± 0.5 mm. A sinusoidal strain with a frequency of 1Hz and magnitude of 0.03% was applied during the test. The temperature was ramped from 50°C to 320°C at a rate of 5°C/min. TA Universal Analysis software was utilized for analyzing of data, and the T_g was measured as the peak of the damping (tanδ) curve.

5.2.7 Differential scanning calorimetry (DSC)

Differential scanning calorimetry (DSC) was carried out to observe the influence of treatment parameters on the polymer crystallinity of the AM composite. A DSC 250 from TA Instruments was utilized for this characterization. Each scan was performed under a nitrogen gas atmosphere with a flow rate of 50 ml/min. Samples of between 5 and 10mg were prepared using a precision saw, and a total of 6 samples were tested for each HIP configuration. The test was performed from 50°C to 400°C at a heating rate of 10°C/min. The TA Instruments software TRIOS v4.5.1 was utilized for analysis of the heat flow data, and the enthalpy calculation was performed via peak integration. In all cases, no cold crystallization peaks were observed, and therefore the reinforcement weight fraction, W_f, enthalpy of melting, ΔH_m, and enthalpy of fusion of an ideal crystal, $\Delta H_f^\circ = 130\ J/g$ [173], were used to determine crystallinity.

An example of a typically DSC curve is given in Figure 51 for a carbon fiber reinforced PEEK composite filament. This sample has been quenched from melt to illustrate the cold crystallization peak. While the glass transition temperature of a polymer can be found as a slight endothermic transition which moves the DSC curve baseline, in the scope of this dissertation glass transition temperature is instead investigated with dynamic mechanical analysis. The DOC was found by integrating the cold crystallization and melting peaks, as seen at 162°C and 335°C,

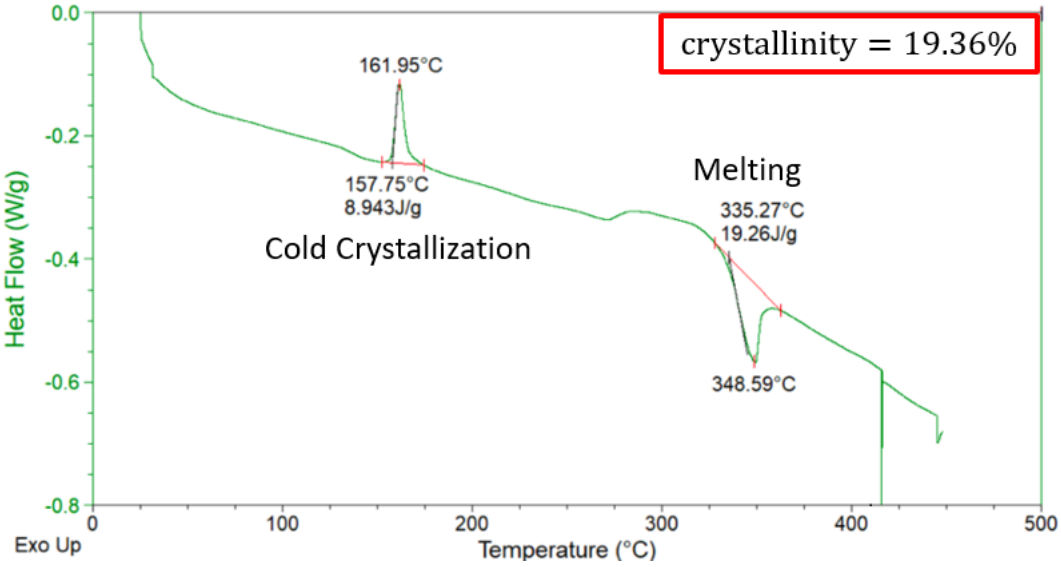

Figure 51. Example of differential scanning calorimetry data taken from a carbon fiber reinforced PEEK composite.

respectively, in Figure 51 to determine the crystallization and melting enthalpies. These enthalpies are then used with Equation (1), in which H_f is the enthalpy of fusion, H_c is the enthalpy of crystallization, H_f^o is the theoretical enthalpy of formation for a 100% crystalline material, and W_f is the weight fraction of the reinforcement.

$$\mathrm{X}_c(\%) = \frac{\Delta H_m - \Delta H_c}{\Delta H_f^o\left(1 - W_f\right)} * 100 \tag{7}$$

5.3 Results and Discussions

The results for the flexural and SBS characterization are illustrated in Figure 52. The percentage change with respect to the reference untreated sample is also shown on top of each bar. The untreated composites display a flexural strength, modulus, and ILSS of 834.3 MPa, 66.3 GPa, and 27.0 MPa, respectively. After a treatment of 200°C and 200psi for 3 hours, these properties increase by 28%, 25%, and 19%, respectively. A further improvement is found by treating under

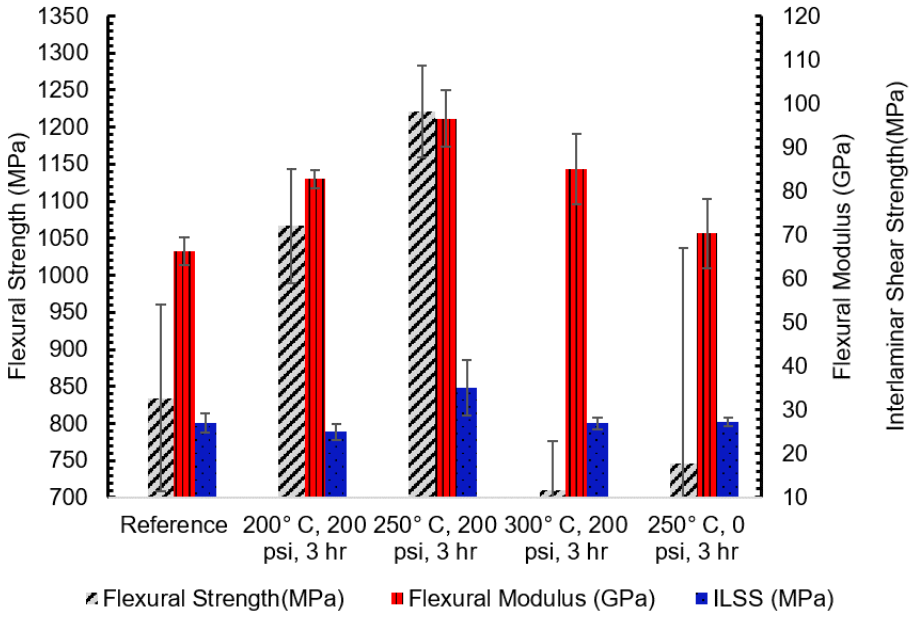

Figure 52. Flexural and short beam shear properties for AM AS4C PEEK composites. Percentage improvement or reduction over the reference sample is shown above each bar. The percentage change for 200C is compared to a reference sample with the same thickness (4mm), while the reference shown here is for 3mm thickness and correlates with all other samples.

250°C, 200psi for 3 hours, where flexural strength, modulus, and ILSS increase by 46%, 46%, and 30% over the reference samples. It was found that further increasing the treatment temperature to 300°C while maintaining the same operating pressure and time resulted in a decrease in flexural strength by 15% and resulted in no change to ILSS. The flexural modulus for this sample was still found to increase by 28%, though this is a lower improvement than was produced by the 250°C treatment. The treatment at 250°C and atmospheric pressure for 3 hours resulted in virtually no change to flexural modulus or ILSS, and while the average flexural strength was found to decrease by 10%, there is significant overlap in standard deviations between the two samples. These results suggest that there is an optimal temperature for effective HIP treatment of composites based on the polymer matrix, and that pressure is essential for obtaining substantial improvements in flexural and interlaminar shear properties.

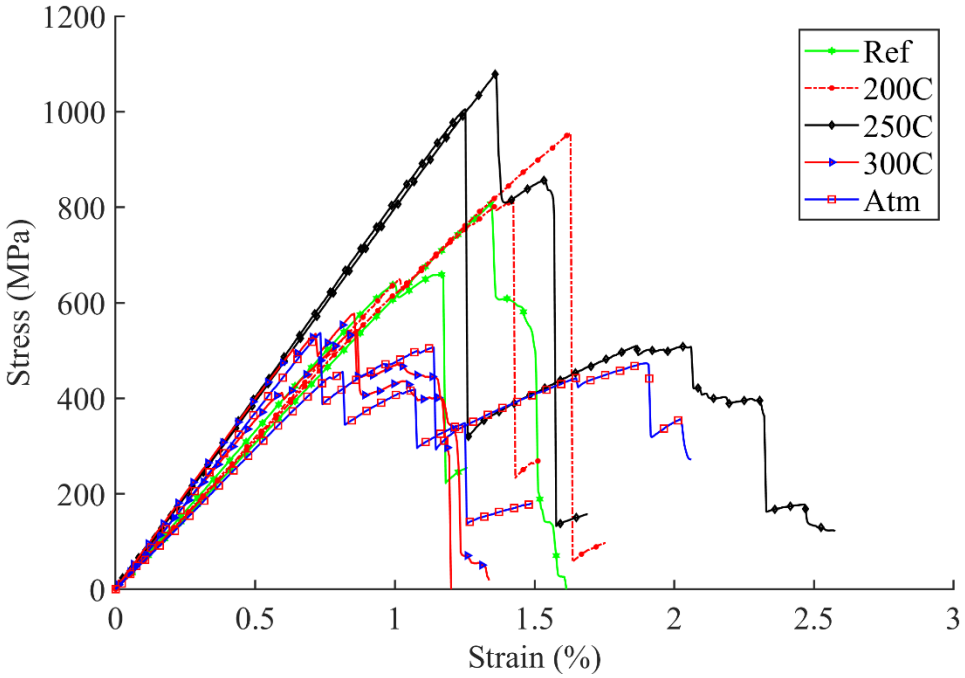

Figure 53. Flexural stress-strain response for HIP treated AM CFRPs.

Representative stress-strain plots for each treatment can be observed in Figure 53. Two curves are shown for each treatment case. Many of the 200C and 250C treated samples resulted in a catastrophic failure, in no evidence of failure was observed before a single event, after which all load carrying capacity was removed. In the untreated sample, slight nonlinearities were sometimes observed before failure, or failure did not take place in a single event. The 300C and Atm samples often displayed a more progressive failure, beginning at low strains but taking place over a larger range of strain rather than at a single event. The 250C treated sample, however, did also display a somewhat progressive failure in certain cases as well.

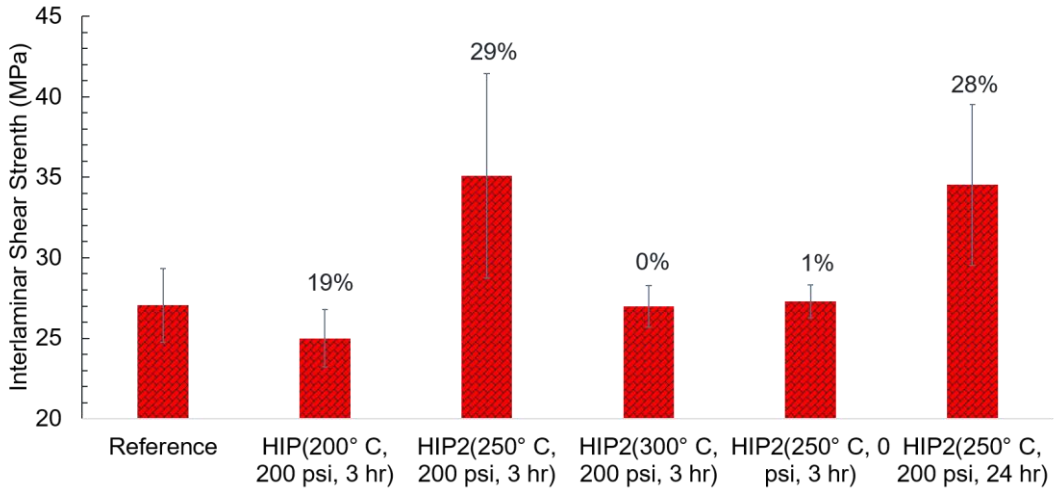

Figure 54. Interlaminar shear strength of HIP treated AM AS4C PEEK composites.

The influence of treatment time on the interlaminar shear strength (ILSS) was also investigated; Figure 54. As the 250°C, 200psi, 3 hour treated sample displayed the largest improvement in properties, the same temperature and pressure were applied to a final SBS sample where the treatment time was increased to 24 hours. It was expected that this would be sufficiently long to allow any mechanisms responsible for improvement adequate time to reach equilibrium. Statistically similar values for ILSS was observed when comparing the 3 hour and 24 hour treatment times, indicating that 3 hours or less is required for this equilibrium to be achieved. This is favorable for commercial adoption, as a relatively short treatment time is required to obtain the maximum improvement in properties. It should be noted that the ILSS values are considered low for the AS4C-PEEK system. In ideal cases, bonding achieved for traditionally fabricated composites in autoclave or hot-press can be as high as 90MPa.

Representative load/deflection plots are shown in Figure 55. In this case only one plot is shown per treatment case for clarity. The failure behavior for Ref, 300C, and Atm samples appear to evolve similarly, with onset at a similar load and deflection and progressing at that load for approximately 1.5mm. Failure begins in the 200C and 250C samples at roughly the same

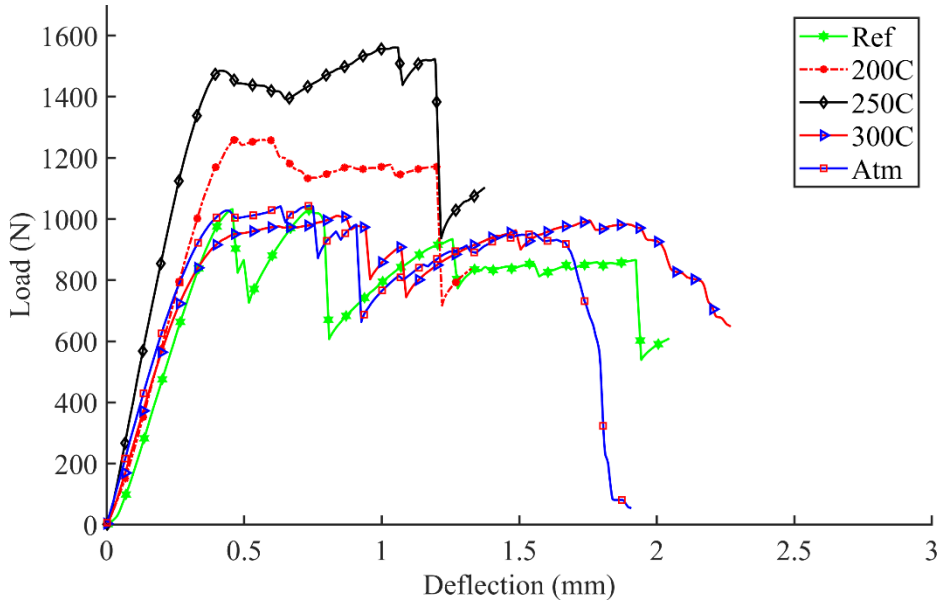

Figure 55. Plot of short beam shear results for HIP treated AM CFRPs.

deflection, but at higher loads. Again, failure progressing in these samples at a relatively constant load until failure, after roughly 1mm of additional deflection.

Pictures of the failed composites surfaces for Ref, 250C, and 300C treated flexural and SBS samples is shown in Figure 56. As expected, the failure mode for all SBS samples was interlaminar shear failure. Crack formation and propagation was observed at multiple layer interfaces for all treatments. In the flexural testing experiments, both compressive failure and interlaminar failure were observed. In general, enforcing compressive failure is preferable in flexural testing, indicating that a decrease in part thickness or increase in span would be

advantageous for future experiments involving flexural testing of AM composites. No substantial trends were observed in changes of part failure between the samples imaged.

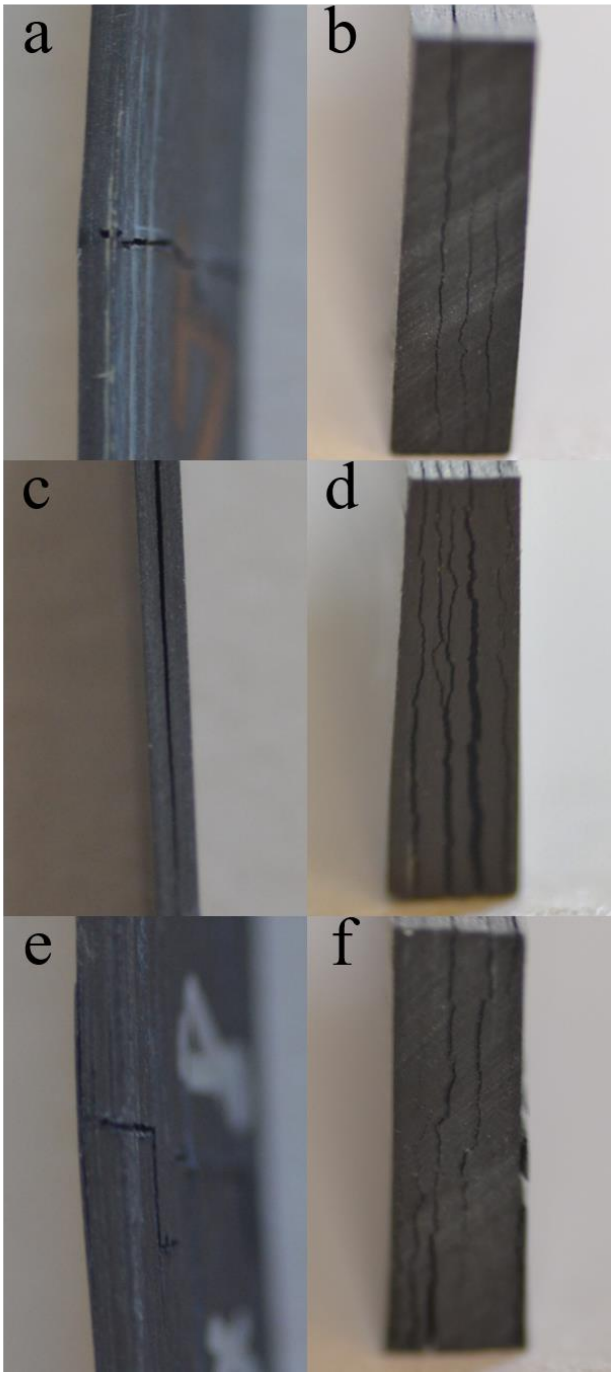

Figure 56. Pictures of failed flexural (left column) and SBS (right column) AM CFRPs for untreated (a and b), 250C treated (c and d), and 300C treated (e and f) samples.

The results for tensile and compression tests are shown in Figure 57. As the 250°C, 200psi, 3-hour treatment resulted in the largest improvement in flexural properties over the untreated material, this was the chosen treatment condition for the tensile and compression coupons. The compressive strength and modulus were found to increase by 18% and 8%, respectively, and tensile strength and modulus increased by 15% and 7%, respectively. It should be noted that the previously highest reported tensile strength and modulus of laboratory developed AM fiber reinforced composites is 464 MPa and 35.7 GPa, respectively, for a carbon fiber reinforced nylon with 18 wt.% fiber reinforcement [21]. The highest reported strength and modulus of commercial continuous fiber reinforced composites is 800MPa and 60Gpa, respectively [144]. The base properties of tensile strength and modulus for unidirectional AM composites is 1134.3 MPa and 85.3 GPa, respectively, which increase to 1311.6 MPa and 91.65 GPa, respectively after post-processing. This corresponds to an improvement of 64% and 53%, respectively, over

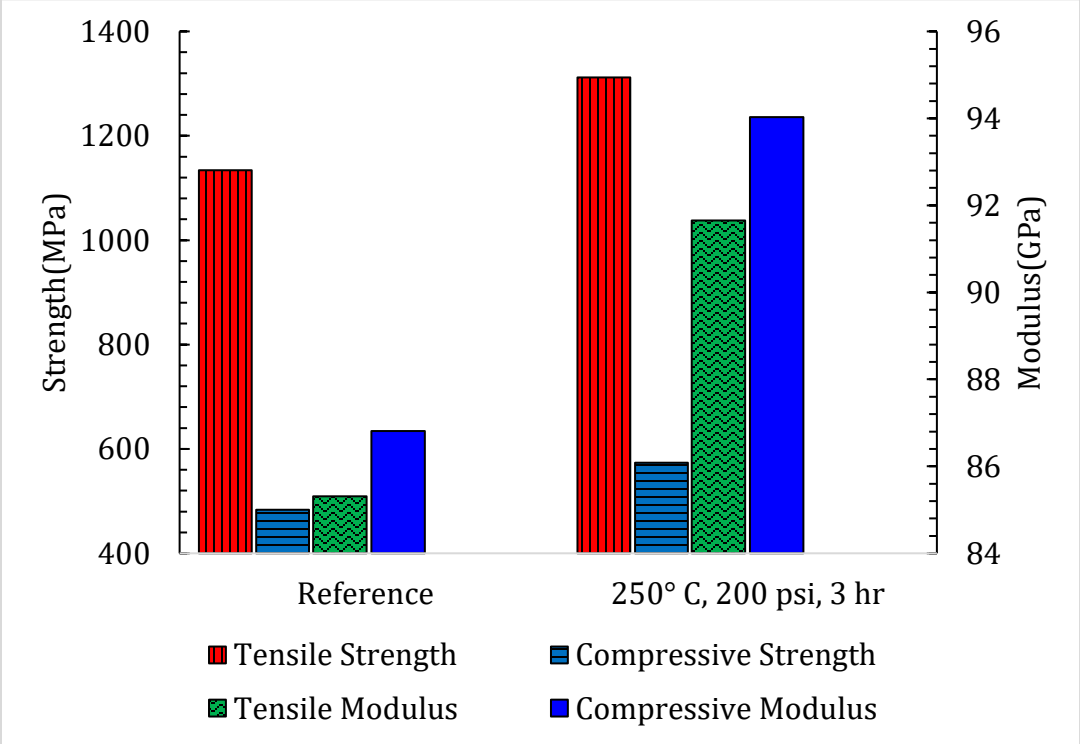

Figure 57. Tensile and compressive properties of AM continuous carbon fiber reinforced PEEK composites.

the tensile strength and modulus of the current state-of-the-art in commercially available continuous fiber reinforced AM composites.

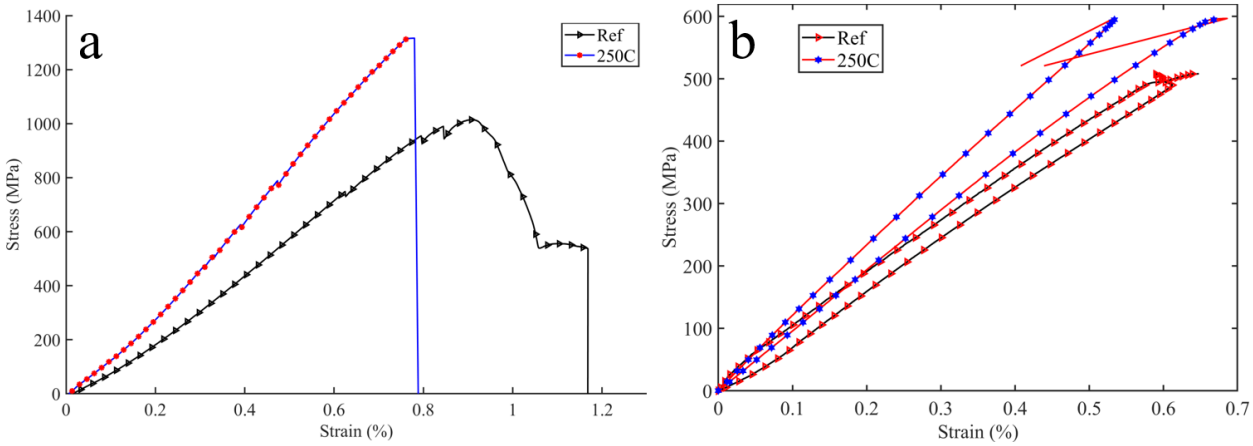

Figure 58. Stress-strain plots of tensile (a) and compressive (b) tests of reference and treated AM CFRPs.

The tensile and compressive stress-strain response can be seen in Figure 58. While composites typically exhibit a brittle failure, the untreated tensile samples did not display a catastrophic failure. Instead, they show a gradual failure, in which the stress gradually drops before the composite breaks completely. This is likely due to the weak interlayer interfaces, which fail to prevent a crack from propagating completely through the sample. Therefore, the weakest layers fail first, but the crack then propagates along the interface and the remaining in-tact layers can continue to carry load. This is consistent with observations of the failed samples, in which significant layer debonding was present. By improving the strength of this interface, the part strength is also increased, and a brittle failure is observed as the crack can propagate through the thickness of the part. No significant changes in compressive failure was observed between untreated and treated composites.

To help understand and contextualize the changes in mechanical properties, the void fraction and morphology was observed using SEM, optical microscopy, and µCT. A single slice of the collected µ-CT cross-sectional data, representing a 1µm thickness of the 1mm specimen tested, is illustrated for the reference, 200°C, 250°C, and 300°C, treatments. In general, the carbon fibers appear homogenously distributed within the matrix, though a few sections can be observed

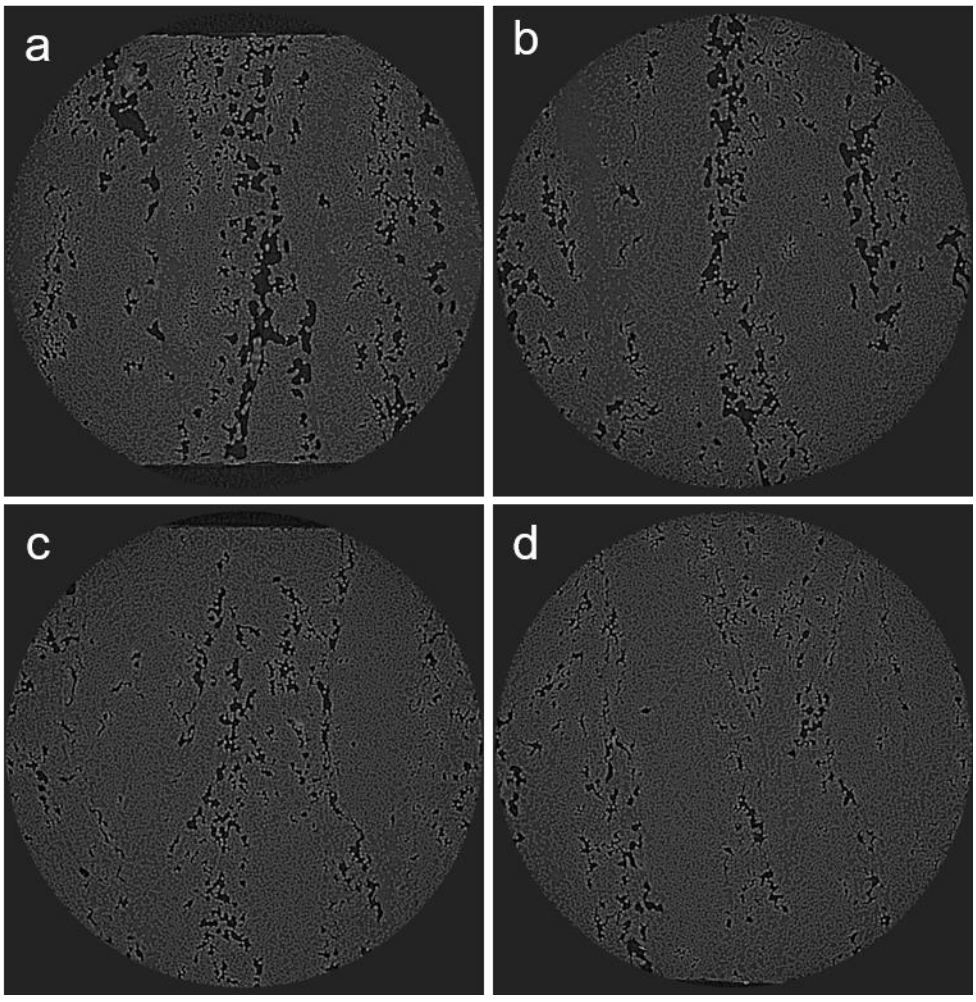

Figure 59. Micro-CT slice of reference and HIP treated AM continuous carbon fiber composite cross-sections. a) Untreated sample. b) 200°C treated sample. c) 250°C treated sample. d) 300°C treated sample.

where matrix rich regions appear. It is clear from these images that the reference sample contains large and often connected networks of voids. The z-direction of the print, corresponding to the layer direction, runs from left to right in all of the CT images shown. As the void networks and

concentration appear in somewhat periodic vertical bands in the images, at distances approximately equal to the layer height set in the print, it is understood that a high concentration of the voids builds up at the layer interfaces during a print. These void networks can be seen to be visibly reduced by the treatment, to a larger extent as the temperature of the treatment is increased.

Table 7. Void content as calculated from micro-CT data. *Sample 1 value is considered an outlier and therefore not included in the average.

	Void Content (vol%)		
Treatment	**Sample 1**	**Sample 2**	**Average**
Ref	**11.47**	**12.11**	**11.79**
200C	**7.49**	**8.53**	**8.01**
250C	**6.67**	**7.10**	**6.89**
300C	**5.14**	**5.33**	**5.24**
Atm	**4.12**	**9.25**	**9.25***

The void morphology within each plane is also elucidated. In addition to the large void content in the plane parallel to the print surface (z-plane), misaligned fibers can also be observed here. Fiber mis-alignments can significantly deteriorate compressive properties in composites and are believed to be a major contributor to the relatively low compressive strengths value measured in our samples. The results of void content calculated from the μ-CT data is shown in Table 7.

With the exception of the Atm. specimen, the void measurement of each sample is within 1% of the average, which indicates a relatively homogeneous distribution of voids within the composite. As expected, by increasing the temperature of the treatment, and keeping the treatment pressure and time constant, the void content of the sample is steadily reduced. Therefore, it can be concluded that the reduction in void content resulting from the HIP treatment

is a key mechanism for the improvement of properties. However, as the void content is lowest for the 300C treatment and the properties of the 300C are diminished over those of the 200C treated specimen, it is clear that other mechanisms are also at play.

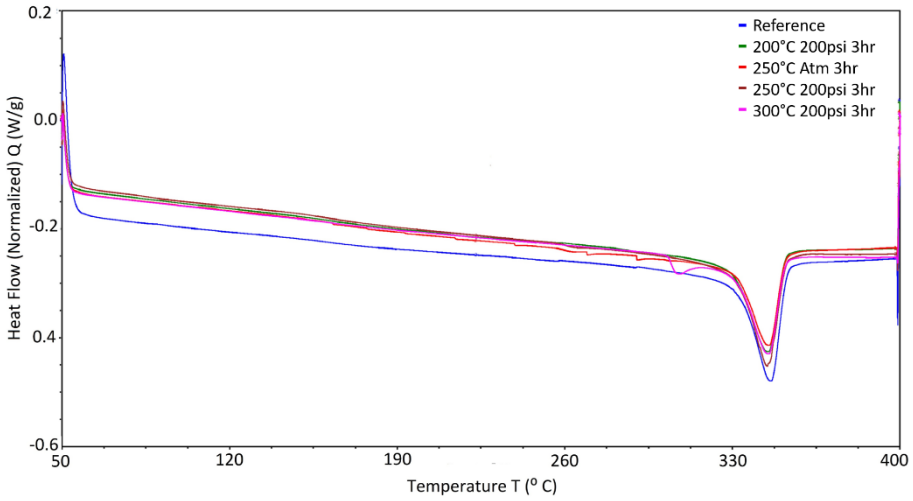

Figure 60. Differential scanning calorimetry results for reference and HIP treated AM PEEK matrix CCFRPs.

The DSC results can be seen in Figure 60. While the cooling rate from melt is relatively high, the 200°C bed temperature used during manufacturing is approximately the temperature of cold crystallization in PEEK, resulting in slight annealing as no cold crystallization peak can be observed in the DSC scans. Therefore, only the enthalpy of melting was used to determine the degree of crystallinity for each treatment. The glass transition peaks are not observed due to the fast heating rate used. Interestingly, the 300°C specimen is the only treatment which exhibited a double melting endotherm. The double melting behavior of PEEK has been reported on previously for annealed or slowly cooled PEEK [174-176], though it is still not fully understood. While explanations for the double-melting behavior of PEEK have been offered related to enthalpic recovery processes, though there is strong evidence that the low melting peak is the result of melting imperfect spherulites that may exist in the lamellar structure. The influence of these imperfect spherulites polymer morphology is further complicated in the case of fiber

reinforced composites and may contribute to the degradation in mechanical performance of the 300°C treated specimen.

A representative image of the DMA results is shown in Figure 61. The T_g for the 250C treated sample shown is 166.86°C. A summary of the average glass transition temperature for the two samples tested per treatment can be seen in Table 8. The storage modulus remains relatively constant until approximately 130°C, after which it begins to fall. The slope of the storage modulus decreases further at approximately 250°C. At 300°C the storage modulus has only been reduced approximately 40%, with a value above 50 GPa. This provides confidence that more complex geometries will only compress slightly to reduce void content but will not deform significantly and therefore will maintain tolerances predictably.

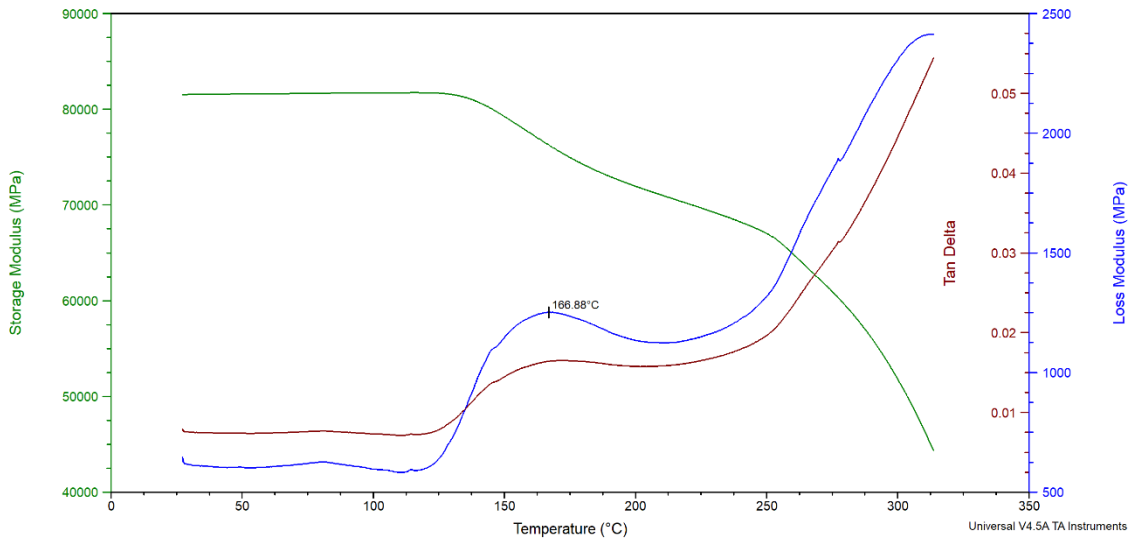

Figure 61. Representative DMA storage modulus, loss modulus, and tan delta curves for AM CCFRP PEEK composites. Pictured scan depicts a 250°C HIP treated sample.

A summary of the structural, thermomechanical, flexural, and interlaminar properties of the tested specimens are shown in Table 8. The reference sample contains a high percentage of internal voids, over 11%, with a relatively low degree of crystallinity at approximately 22%. Treatment using 200°C, 200psi for 3 hours results in a 32% reduction in internal voids, with no

significant change in polymer crystallinity. The unchanged degree of crystallinity (DOC) is to be expected as the samples are processed on a heated bed at 200°C, and therefore a larger temperature is likely needed to induce additional crystallization. Accompanying the decrease in void content is an increase in flexural strength and modulus of 28% and 25%. This improvement is attributed to the lower void content since a similar void content and ILSS (indicative of interlaminar diffusion) to the reference sample is observed. While the treatment temperature is higher than the Tg, it is likely not high enough to enable a notable interlayer polymer diffusion, evident by an unchanged ILSS.

Table 8. Summary of void content, degree of crystallinity, glass transition temperature, flexural strength, flexural modulus, and ILSS for the reference and HIP treated AM CCFRPs.

Treatment	Void content (%)	DOC (%)	T_g (°C)	Flexural Strength (MPa)	Flexural Modulus (GPa)	ILSS (MPa)
Ref	**11.79**	**22.2**	**165.5**	**834.3**	**66.3**	**27.1**
200C	**8.01**	**22.3**	**161.2**	**1066.5**	**82.8**	**25**
250C	**6.89**	**23.35**	**164.4**	**1220.9**	**96.6**	**35.1**
300C	**5.24**	**28.79**	**167.8**	**710.0**	**85.0**	**27.0**
Atm	**9.25**	**25.53**	**156.7**	**745.7**	**70.4**	**27.3**

Increasing the treatment temperature to 250°C further reduced the void content, resulting in a 41% decrease in internal void volume compared with the reference sample. A 5% relative increase in crystallinity was observed over the untreated material. These treatment conditions resulted in the largest improvement in mechanical performance, with an increase in flexural strength, modulus, and ILSS of 46%, 46%, and 30%, respectively, over the reference specimens. Further increasing the treatment temperature to 300°C resulted in an additional reduction in void content to the lowest value measured at 5.24%, and the largest DOC of 28.79%. This treatment,

however, also resulted in a decrease in mechanical performance compared with the 250°C treatment, and even reduction in flexural strength compared with the untreated material.

The relative reduction in mechanical performance, despite having the lowest void content, can be seen as a result of changes in polymer crystallinity. While the strength and stiffness of PEEK increases with crystallinity, the material also becomes more brittle at a higher DOC [172]. Crack formation and propagation resulting from stress concentration at void interfaces occurs more readily in brittle materials. Blunting of sharp crack tips due to plastic deformation of the matrix, resulting in a decrease in the local stress concentration, cannot occur to the same degree as with a ductile material. With a 30% increase in crystallinity over the reference sample, it is expected that the decrease in flexural strength and interlaminar shear strength in particular are caused increase in matrix brittleness and remaining void content. Additionally, the influence of the double melting peak observed in DSC, and resulting microstructure, on the mechanical performance of a composite are not well understood and may contribute to the change in properties as well.

Lastly, the Atm. sample indicates that isostatic pressure is essential for an effective post-processing treatment. The flexural strength, stiffness, and ILSS of the composite change by -11%, +6%, and +1%, respectively. This is likely due to either a possibly larger void content or the increase in polymer crystallinity and associated brittle failure modes. The Ext. sample also showed that with an applied temperature and pressure of 250°C and 200psi, increasing the treatment time from 3 hours to 24 hours resulted in no significant change in ILSS.

Statistical significance of the changes in mechanical properties as a result of treatment was carried out using a paired, two-tailed student t-test. The p-value for each set of data is shown in Table 9. Taking p-values below 0.05 as statistically significant, the cases for which the null

hypothesis cannot be rejected are illustrated with red text. These results agree with previous observations and predictions. While the flexural modulus was improved in the 300C treated sample, the flexural strength and ILSS treatments did not show a change significant enough to reject the null hypothesis. This was true for all properties of the Atm treatment as well, further indicating the necessity of pressure when post-processing composite parts. The compressive modulus also did not show a significant change due to the post-processing treatment at 250C.

Treatment	Flexural Strength	Flexural Modulus	ILSS	Tensile Strength	Tensile Modulus	Compressive Strength	Compressive Modulus
200C	0.0055	0.0050	0.023	n/a	n/a	n/a	n/a
250C	0.0023	0.015	0.0044	0.034	0.023	0.0034	0.091
300C	0.12	0.0045	0.49	n/a	n/a	n/a	n/a
Atm	0.34	0.23	0.44	n/a	n/a	n/a	n/a
Ext	n/a	n/a	0.032	n/a	n/a	n/a	n/a

Table 9. Student t-test results showing p-values for the mechanical property data collected. Taking a p-value of 0.05 as a threshold for significance, the cases in which the null hypothesis is not rejected are highlighted in red.

5.4 Conclusions

The use of hot isostatic pressing (HIP) to treat ultra-high strength additively manufactured continuous carbon fiber reinforced PEEK composites was investigated. It was found that treatment at 250°C, 200psi, for 3 hours produced the highest composite properties. This treatment resulted in an increase in flexural strength, flexural modulus, and ILSS, of 46%, 46%, 30%, respectively. Additionally, the tensile strength, tensile modulus, compressive strength, and compressive modulus were found to increase by 15%, 7%, 18%, and 8%, respectively, under the same treatment conditions compared with untreated material. The improvements in mechanical

properties are attributed to a reduction in the composite void content, from 11.79% to 6.89%, as measured with μ-CT. While increasing the treatment temperature to 300°C with the same treatment pressure and time, did result in a further reduction in void content, the mechanical properties measured were lower than those produced by the 250°C treatment. This is attributed to the change in crystallinity induced by the higher temperature treatment, which likely embrittles the matrix allowing for cracks to form and propagate more easily. This treatment can be applied to AM continuous fiber composites, short fiber composites, or unfilled polymer parts of arbitrary shape, size, and composition, to provide a significant improvement in mechanical properties.

Chapter 6. Influence of Hot Isostatic Pressing on the Fiber-Matrix Interphase in Carbon Fiber PEEK Composites

Nekoda van de Werken[a], Pratik Koirala[b], Jafar Ghorbani[a], and Mehran Tehrani[a,b]

[a] Department of Mechanical Engineering, University of New Mexico, Albuquerque, NM, United States

[b] Walker Department of Mechanical Engineering, University of Texas, Austin, TX, United States

Hot isostatic pressing can be utilized as a post-processing technique to eliminate voids and increase crystallinity in additively manufactured (AM) thermoplastic composites, leading to improved mechanical properties. While the void content and morphology can be characterized with common methods such as micro computed tomography, cross-sectional microscopy, or density, the local matrix properties, specifically adjacent to the fiber, can be more difficult to characterize. In this study, additively manufactured carbon fiber polyetheretherketone (PEEK) composites were treated under 200 psi and 250 or 300 C for three hours. Samples undergo fast cooling, whether fused filament fabrication or automated fiber placement is used, resulting in low PEEK crystallinity. An energy-based nanoindentation approach using cyclic loading and unloading was utilized to observe the development of friction, plastic deformation in the matrix, and elastic deformation of the matrix during indentation. This approach was used to investigate the formation and propagation of cracks at the fiber-matrix interface and compare the interaction between fiber and matrix corresponding to different HIP post-processing conditions. Additional context for interfacial and bulk mechanical properties was supplied by investigating the interphase thickness and local matrix properties through atomic force microscope (AFM) nanomechanical mapping. These characterizations were used to provide an understanding of the process-structure-property relationships in AM carbon fiber-PEEK composites.

6.1 Introduction

Additively manufactured (AM) continuous fiber reinforced composites have only relatively recently been investigated within academic and commercial environments. AM offers unique advantages over conventional composite manufacturing techniques, such as increasing the design freedom of fiber placement, orientation, and overall part geometric complexity. This design freedom can provide weight savings that are critically important in high-value applications. While substantial improvements to additively manufactured (AM) carbon fiber reinforced polymer (CFRP) composite properties have been made in the recent past, many challenges remain in the pursuit of high-performance AM CFRPs [21, 131].

One clear target in the pursuit of material performance improvement is the substantial porosity that is commonly observed in polymer and composite parts manufactured with fused filament fabrication (FFF) [23]. Voids are known to produce degrade a variety of mechanical properties, including interlaminar shear strength, tensile properties, compressive properties, flexural properties, transverse properties, impact performance, and fatigue behavior [171]. As shown previously, the void content can be addressed to a large degree by post-processing composite parts using hot isostatic pressing (HIP). In the case of AM continuous carbon fiber reinforced PEEK composites, HIP was able to provide a reduction in void content from 11.7% to 5.2%, resulting in an increase in the composite flexural strength and stiffness each by 46%.

Semi-crystalline thermoplastics in FFF provide additional challenges compared with conventional composite manufacturing methods by introducing unknown variables, such as the influence of a unique polymer degree of crystallinity (DOC) and crystalline morphology on the composite performance. In conventional composite manufacturing practices, control over the

thermal history of the polymer is rigorously controlled to provide a favorable polymer microstructure. The parameters of thermal history that most influence the polymer microstructure are the time in melt, cooling rate or cooling profile from melt, and thermal annealing conditions. In compression molding, for example, these can all be thoroughly controlled by controlling the polymer flow rate and mold temperature over time [177]. In FFF, however, time in melt is generally very brief and influences manufacturing time significantly, as it is inherently tied to print speed. Additionally, the polymer is cooled from melt to the chamber or bed temperature very quickly due to conductive and convective heat transfer between the new layer and previous layers or substrate, and generally forced air cooling. The loss of precise control over the thermal history of the polymer creates a unique and unknown microstructure, and therefore also creates uncertainty in the composite properties.

The influence of polymer microstructure on both polymer and composite mechanical properties has been studied in semicrystalline thermoplastic composites [160, 161, 178, 179]. In general, an increase in the polymer crystallinity induced by lowering the cooling rate from melt leads to an increase in the strength and stiffness of PEEK, and a decrease in ductility [172]. While crystallinity can be measured with bulk techniques, such as differential scanning calorimetry (DSC), the local crystalline microstructure can also have a significant effect on the composite properties [167]. In an unfilled semicrystalline polymer, nucleation of spherulites occurs within the polymer, known as homogeneous nucleation. When foreign particles or fibers are present, nucleation can occur on the surface of those materials, known as heterogenous nucleation, for which the resulting crystallinity is known as transcrystallinity [180]. The transcrystalline region of the polymer contributes significantly to the interfacial properties of the fiber-matrix system, which subsequently influences the mechanical properties of the composite [167].

The properties of the fiber-matrix interface have been investigated using single fiber push out, single fiber pull out, single fiber compression, single fiber fragmentation, and the microdroplet debond tests [181]. These methods are commonly used to characterize the interfacial shear strength of the composite. By applying a cyclic loading and unloading schedule during nanoindentation single fiber push out, an energy-based approach can be utilized to understand the contribution of elastic deformation, plastic deformation, and friction during each loading cycle [182]. This has been applied to various carbon fiber reinforced semicrystalline composites, including PEEK and polyphenylene sulfide (PPS) [183, 184]. This technique can be used to determine the behavior of crack formation and propagation at the interface.

As the total crystallinity of the composite changes due to annealing, the transcrystallinity is likely to experience restructuring, though the nature of that restructuring is not well understood. The thickness of the interphase region can be investigated using nanomechanical mapping techniques, commonly implemented using atomic force microscopy [185]. The implementation is similar to nanoindentation, though the tip radius is on the order of nanometers rather than micrometers. Force-displacement data, or equivalent, can be collected, and the local material modulus can be extracted. The modulus gradually reduces from that of the fiber to that of the matrix when crossing the interphase, and the physical distance over which that occurs is considered the interphase thickness.

The aim of this study is to utilize etching, single fiber pushout, and nanomechanical mapping to provide additional insight into the process-structure-property relationships present in AM continuous carbon fiber reinforced PEEK composites. As the influence of post processing the composite using hot isostatic pressing (HIP) has been studied, detailed information about the polymer and interphase microstructures can aid in the interpretation of these property changes.

6.2 Materials and methods

6.2.1 Materials

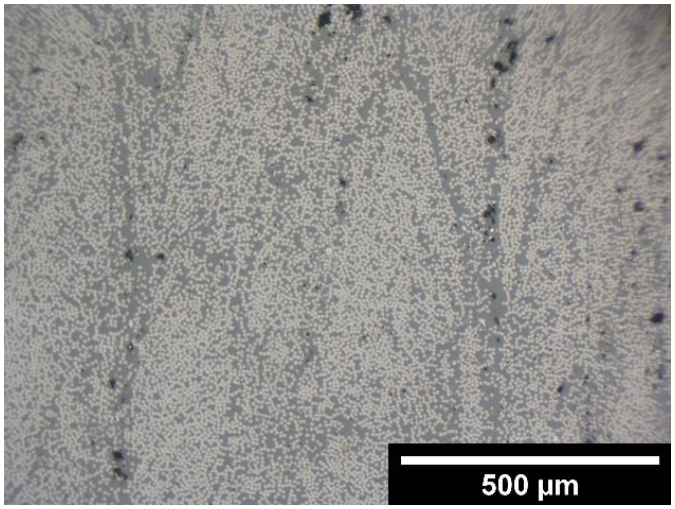

Figure 62. Cross-sectional optical micrograph of continuous carbon fiber reinforced PEEK filament. The fiber distribution, matrix rich regions, and voids can be observed.

The continuous carbon fiber reinforced PEEK composites were manufactured using FFF by Mantis composites. A composite filament was prepared with a diameter of approximately 0.77-0.8mm, with an AS4C carbon fiber volume fraction of 41-43%. A nozzle temperature of 415°C, bed temperature of 200°C, and print speed of 80mm/min were used during part FFF printing. The PEEK used in the matrix was not modified for this manufacturing process, though the molecular weight(s) of the polymer were not provided. A thermal model was used to estimate the time spent in melt and cooling rate in melt, which was found to be approximately 40s and 480°C/min, respectively. The part temperature during the print was maintained at approximately the bed temperature (200°C), which is near the cold crystallization temperature of PEEK and therefore may result in mild annealing of the polymer. The cross-section of the printed composite part can be seen in Figure 62.

6.2.2 Scanning electron microscopy (SEM)

Scanning electron microscopy and optical microscopy were used to observe the composite cross-sections to observe void content, void structure, and homogeneity of fiber packing. Cross-sectional samples with carbon fibers perpendicular to the cut direction were prepared for microscopy. The samples were mounted in an acrylic mold, ground using silicon carbide paper up to a maximum grit of 1200. The sample surfaces were then polished using a 1µm diamond colloidal suspension and a 0.05µm silica colloidal suspension. The prepared cross-sections were coated with a few nanometers of gold before imaging with an FEI Quanta 3D FEG SEM. Optical microscopy was carried out with a metallurgical microscope with objectives between 10X and 50X magnification.

6.2.3 Atomic force microscopy (AFM)

Atomic force microscopy was utilized to image both the etched samples and the HIP treated samples prior to nanomechanical mapping. An Asylum MFP-3D was used to image the sample surface in tapping mode using a Bruker RTESPA-525 tip, with a nominal length, width, spring constant, resonant frequency, and tip radius of 125µm, 40µm, 200N/m, 525kHz, and 8nm, respectively. Scanning electron micrographs of the cantilever and tip can be seen in Figure 63.

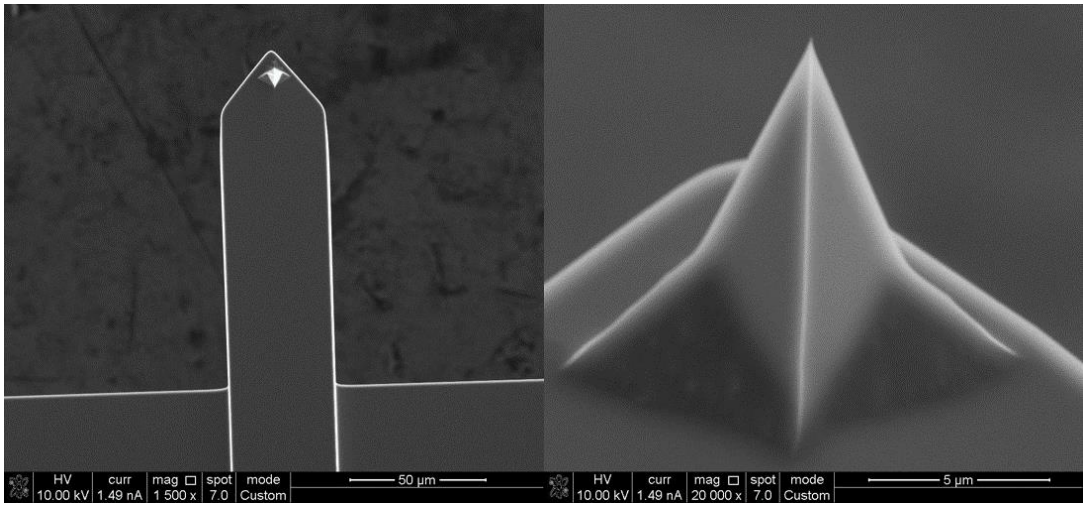

Figure 63. Cantilever and tip used for atomic force microscopy imaging and force mapping.

6.2.4 Polymer etching

Chemical etching is can be utilized to provide contrast between polymer microstructures, making them possible to view with scanning electron microscopy or atomic force microscopy [172, 186, 187]. In general, this contrast is created by exploiting the different rates of dissolution that exist between various microstructures and the etchant. Crystalline structures are typically more thermodynamically stable than amorphous structures, and therefore dissolve more slowly than their disordered counterparts, creating topographical contrast between crystalline and amorphous regions. In polymers, this contrast is typically used to observe the spherulite size, nucleation density, and lamellae structure [187].

A permanganate etchant has been found effective on PEEK, which was selected for this study [186]. Various permanganate solutions have been proposed, using either a sulfuric or phosphoric acid base [186, 187]. Both etchants were investigated on the composites in this study. The solution with sulfuric acid consisted of 1 wt.% potassium permanganate stirred into a 5:2:2 solution of sulfuric acid, orthophosphoric acid, and distilled water. Samples were submerged in

the solutions for 5 minutes, then washed briefly in a 7:2 solution of sulfuric acid, rinsed in 30% hydrogen peroxide, and finally rinsed with distilled water. The solution without sulfuric acid consisted 2 wt.% potassium permanganate dissolved in a 4:1 solution of orthophosphoric acid and water. Samples were etched for either 5 minutes or 50 minutes, followed by rinsing with DI water. Cross-sectional segments of the printing filament were prepared with the microscopy preparation techniques described in Section 6.2.2. Carbon fiber reinforced PEEK filament cross-sections were used in this study, which were slowed cooled from melt at a rate of 1°C/min to ensure a high DOC for ease of viewing.

6.2.5 Nanoindentation

A Nanotest 600 equipped with an optical microscope and nanopositioner motion stage was used for the single fiber push out experiments. A conical tip with nominal diameter of 3μm was used to push out the approximately 7μm diameter fibers, as seen in Figure 64. Each fiber was loaded and unloaded in depth-controlled cycles, increasing by 100nm increments until a total indentation depth of 2500nm. A loading/unloading rate of 0.1mN/s was used for all indentations,

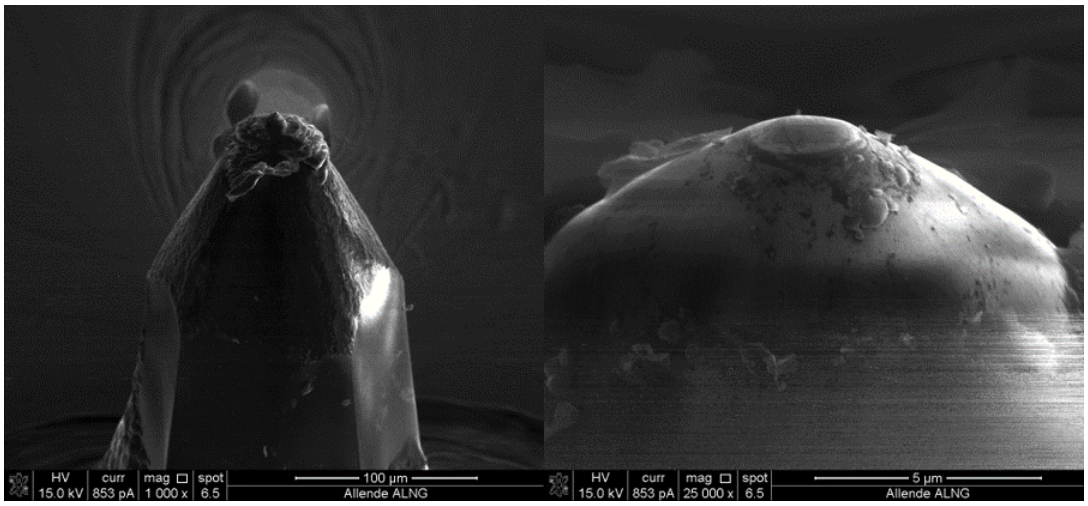

Figure 64. Nanoindenter tip used in single fiber pushout experiment. Tip has a nominal diameter of 3µm.

as the device is inherently force controlled. Displacement control is implemented with closed-loop feedback from the parallel plate capacitor.

Composite cross-section slices were prepared by cutting approximately 500µm segments from the center of untested SBS cross-sections. These sections were ground and polished by hand using lapping paper with finishes of 40µm, 30µm, 12µm, 9µm, 5µm, 3µm, 1µm, and 0.3µm to a final sample thickness of 50µm. The thickness was measured using a digital micrometer centered over the sample. The same grinding and polishing procedures were applied to both sides of the sample, ensuring that sufficient material was removed that no residual damage from the cutting would remain during the push out experiment.

To allow the fibers to push out of the matrix freely, the region of interest defined for indentation must be free-standing. This was accomplished by adhering two glass slides to the aluminum nanoindenter mounting block using cyanoacrylate glue and ensuring a consistent 50µm gap between the slides using a 50µm thickness aluminum foil as a spacer. The sample cross-sections were then adhered to the glass slides over the gap using quartz wax, as shown in Figure 65. Pressure was applied to the surface of the samples while the wax was melted to ensure intimate

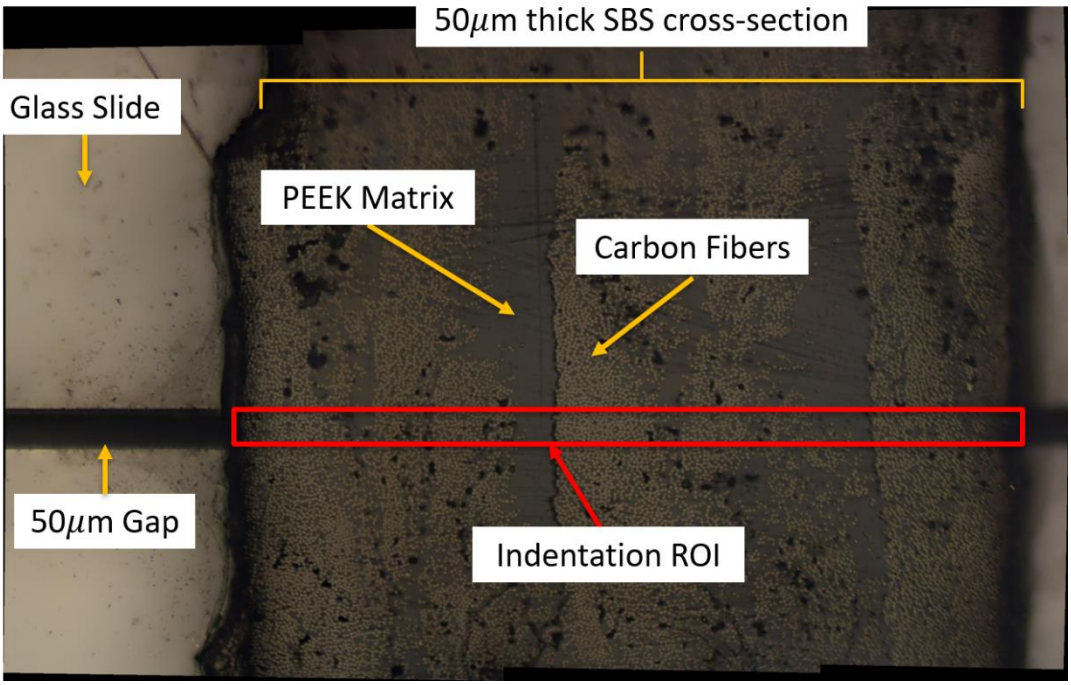

Figure 65. AM continuous carbon fiber reinforced PEEK cross-section mounted to glass slides on nanoindenter mounting stub. Indentation region of interest (ROI) is shown.

contact between the sample and substrate. This was found to prevent excess compliance during indentation, brought on by bending of the thin sample when external force was applied.

The single fiber pushout test requires an accurate placement of the indenter tip at the center of carbon fibers in the region of interest. It was found that after crosshair calibration of the microscope, which links the position of the indenter tip to the center of the microscope objective, a few microns drift still existed when changing between the objective and the indenter positions. Therefore, the nanopositioner stage was used to capture high-resolution scans of the sample surface with the indenter tip. The nanopositioner was used to position the sample in 0.5µm steps on each axis in-plane, and the nanoindenter tip is used to detect the height of the sample surface. The fiber surfaces are always at a slightly different height than the matrix, and therefore the location of the fibers can be accurately imaged, as seen in Figure 66. With a sub-micron resolution, the indentation placement can be repeatably placed at the center of fibers.

Three samples were prepared for single fiber pushout testing: untreated, 250°C, 200psi, 3hr, and 300°C, 200psi, 3hr. The 250°C sample was chosen as the treatment produced the largest improvement in mechanical properties over the untreated sample. The 300°C was chosen because while the void content was measured to be the lowest of all treatment conditions, all of the mechanical properties measured were lower than those of the 250°C treatment. In each case, a minimum of 20 fibers were indented, and a minimum of 10 fibers were used for analysis.

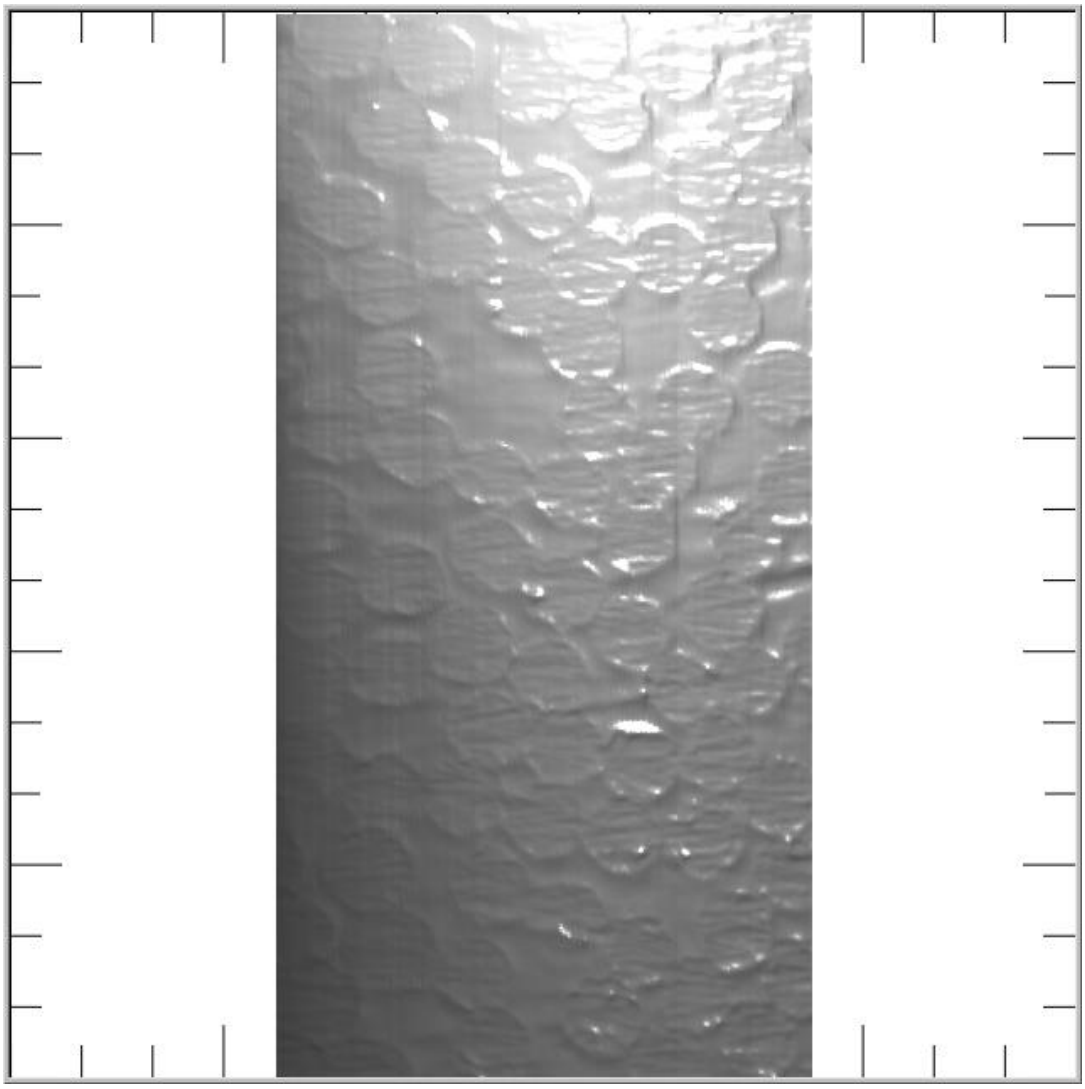

Figure 66. Nanopositioner scan of the AM AS4C PEEK composite surface prior to indentation. Surface illumination is on, with an artificial light source at the top of the image. Scan dimensions are 50 x 100µm, where the 100µm dimension is parallel to the gap between glass slides.

Indentation data which did not show clear signs of fiber debonding, or displayed low initial

modulus, indicating improper initial bonding between fiber and matrix, were not considered in the analysis. Examples of acceptable and rejected pushout behavior can be seen in Figure 67. The top two plots show acceptable indentation data, as the stiffness and failure align with expectations. The top left plot shows a fiber that displayed a more progressive failure, while the top right plot displayed a distinct failure/pushout event. The bottom two plots do not display a large linear region in the low-load regime, and reach a much lower maximum force with no clear sign of failure. This can be cause by either inaccurate indentation placement or indentation of fibers that are either damaged or contain damaged interfaces.

The analysis of the pushout data is performed by numerically integrating each loading, unloading, and reloading curve in a plot. A representative example of the energy analysis is shown in Figure 68, in this case showing the analysis for the top two plots in Figure 67. The

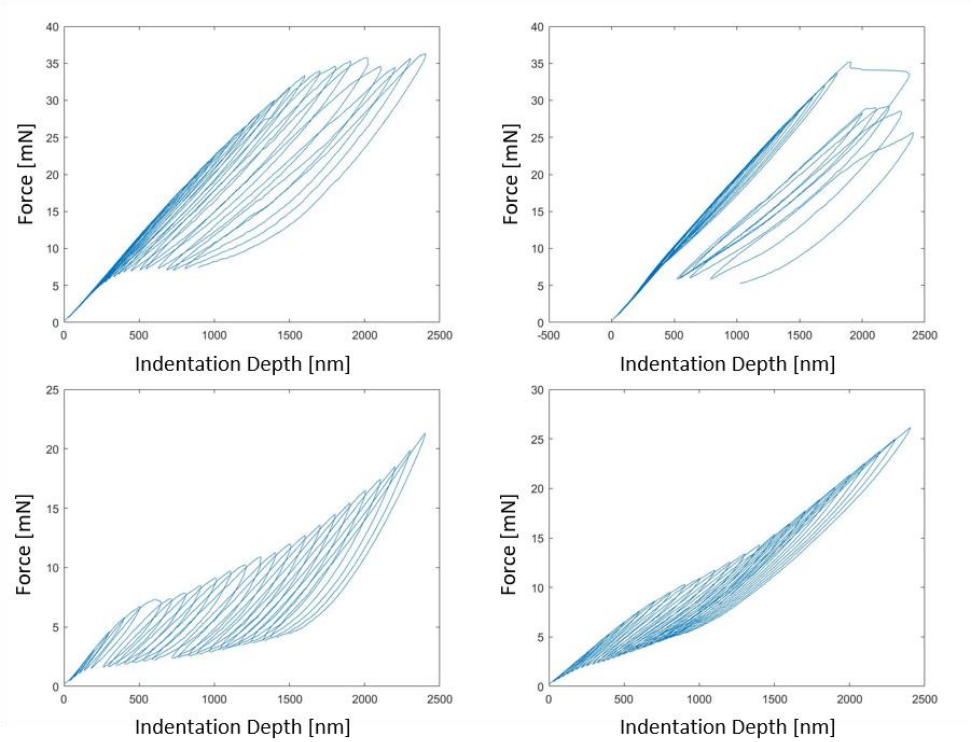

Figure 67. Behavior observed during single fiber pushout experiments. The top two results are considered acceptable data, while the bottom two are rejected for analysis.

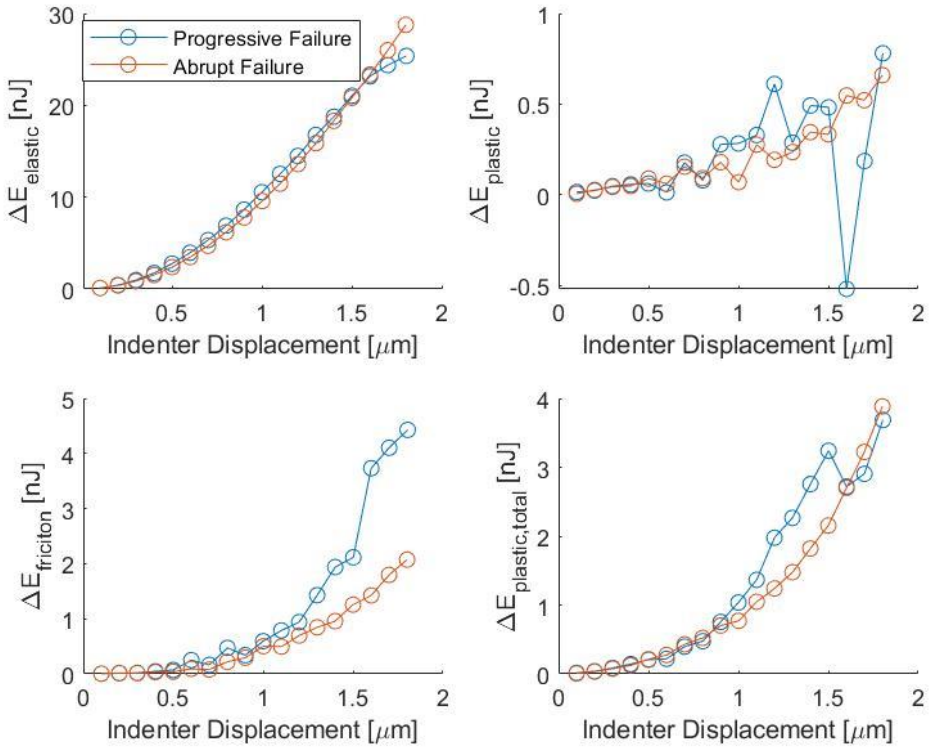

Figure 68. Representative energy analysis of single fiber pushout experiment. Both progressive failure and abrupt failure cases are shown.

reloading curve for a load cycle is defined as the subsequent loading curve up to the same depth as the current loading curve. The elastic energy, $\Delta E_{elastic}$is found as the area under the loading curve. The energy lost due to plastic deformation, $\Delta E_{plastic}$, of the matrix and fiber, in the case of fiber crushing, is found as the difference between the integrals of the unloading and reloading curves. The total contribution of plastic deformation, $\Delta E_{plastic,total}$, is also calculated as the cumulative sum of the $\Delta E_{plastic}$. The energy contribution of friction, $\Delta E_{friction}$, being the sum of indenter-fiber and fiber-matrix friction, is found as the difference between the integrals of the reloading and unloading curves.

6.2.6 Nanomechanical mapping

Nanomechanical mapping was performed using the same AFM and tip as used for AFM imaging. Force maps were generated across the fiber-matrix interface to observe the change is stiffness from the fiber to the matrix allowing for the interphase thickness to be measured. Using a standard indentation approach becomes prohibitively time consuming for high-resolution 2D surface scans, and therefore only linear scans across the interface were captured. These scans were captured across distances of between 500 and 1000nm, with a resolution of 1nm. An example of the fiber-matrix surface and scanning direction, as imaged with AFM, can be seen in Figure 69. A tip deflection of 20nm and stage displacement rate of 20nm/s were chosen as parameters for the experiment, as they provided consistent indentation results with relatively low noise for both the fiber and matrix. As these two materials have significantly different elastic moduli, the cantilever, indenter tip, and experimental parameters must be chosen carefully to provide at least a few nanometers of displacement of the cantilever and fiber or matrix for the duration of the test.

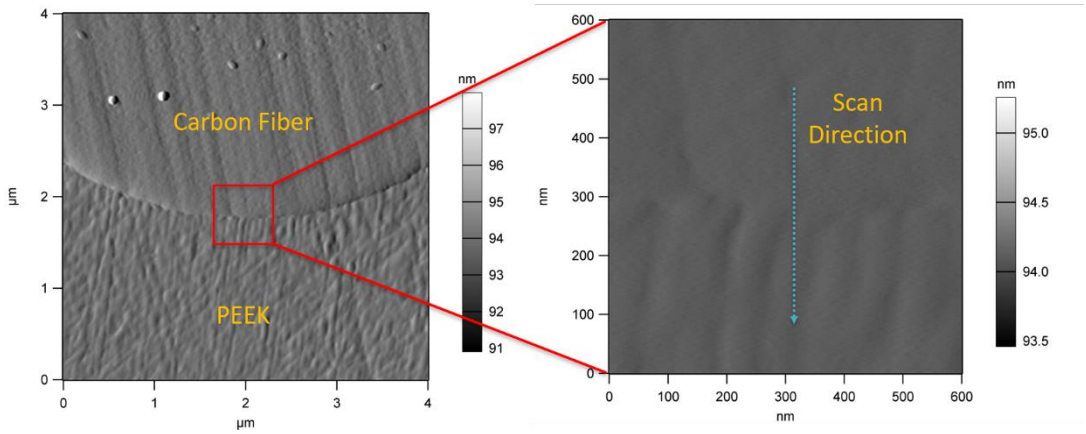

Figure 69. Atomic force micrographs of carbon fiber PEEK interface. Scan direction used during nanomechanical mapping is indicated.

An example of the deflection of the AFM tip with respect to the piezo position is shown in Figure 70. The AFM tip deflection is related to the applied force through the spring constant of the cantilever, and therefore can be used to calculate force when calibrated. For the purposes of this study, only the relative properties are of interest, and therefore force calibration is not required. As the AFM tip approaches the sample, a slight attractive force can be observed as van der Waals forces become significant. The following loading/unloading curve develops linearly, which can be used to determine the relative stiffness of the two materials in the composite. An additional attractive force can be seen at the point of unloading due to the adhesion between the AFM tip and sample surface.

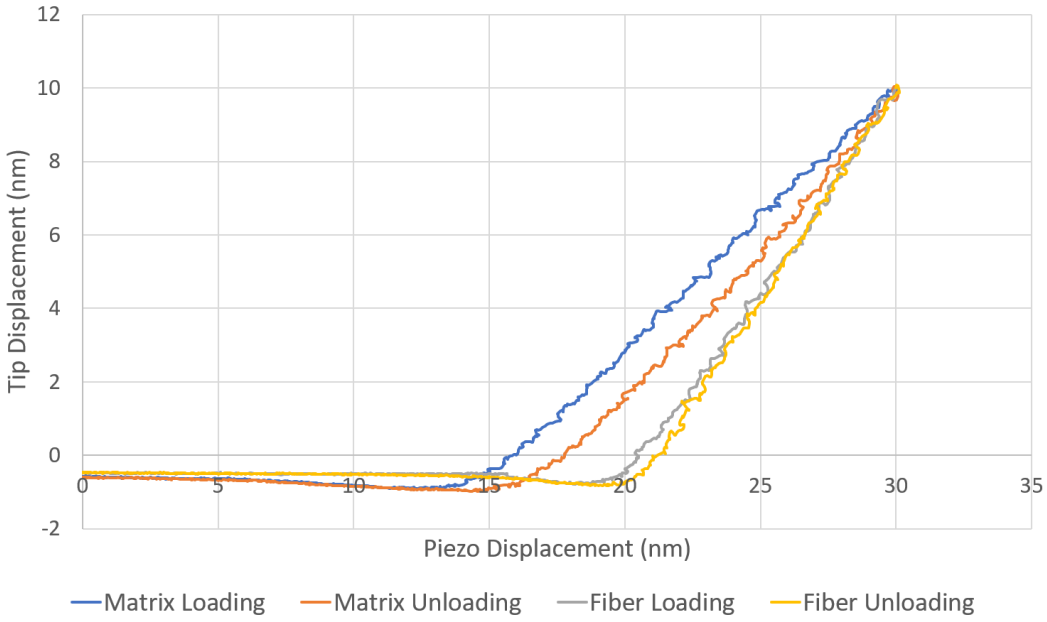

Figure 70. Typical loading and unloading behavior of carbon fiber and PEEK matrix during AFM force mapping.

The force map is calculated using the inverse optical lever detection sensitivity (InvOLS). The InvOLS is found from the inverse of the linear slope of the unloading portion of each force-deflection curve, measured between 10 and 90% of the maximum force in the segment. Therefore, the InvOLS is proportional to the compliance of the material being interrogated. An example of the InvOLS map across the fiber-matrix interface is shown in Figure 71. The relatively compliant PEEK matrix can be observed on the left, which transitions through the interphase region into the relatively stiff carbon fiber surface. While the absolute values of stiffness are not considered in this study, the relative stiffness of the relevant materials and interphase thickness can both be accurately compared.

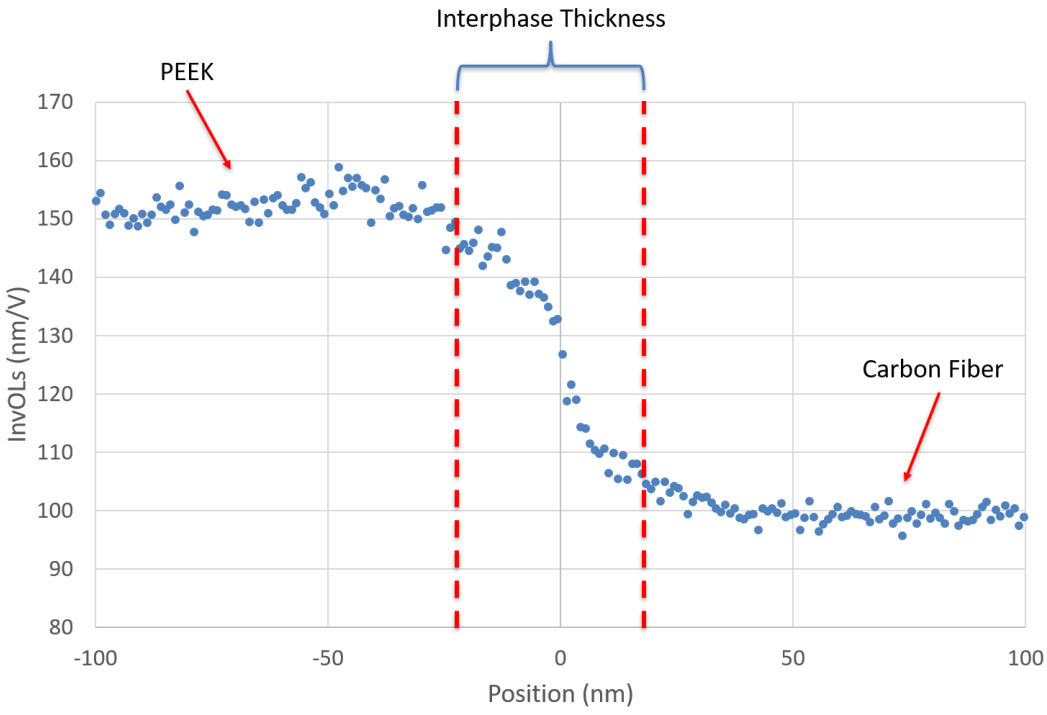

Figure 71. Force map across fiber-matrix interface using atomic force microscopy. Indenter moves from matrix to fiber surface from left to right.

6.3 Results and Discussions

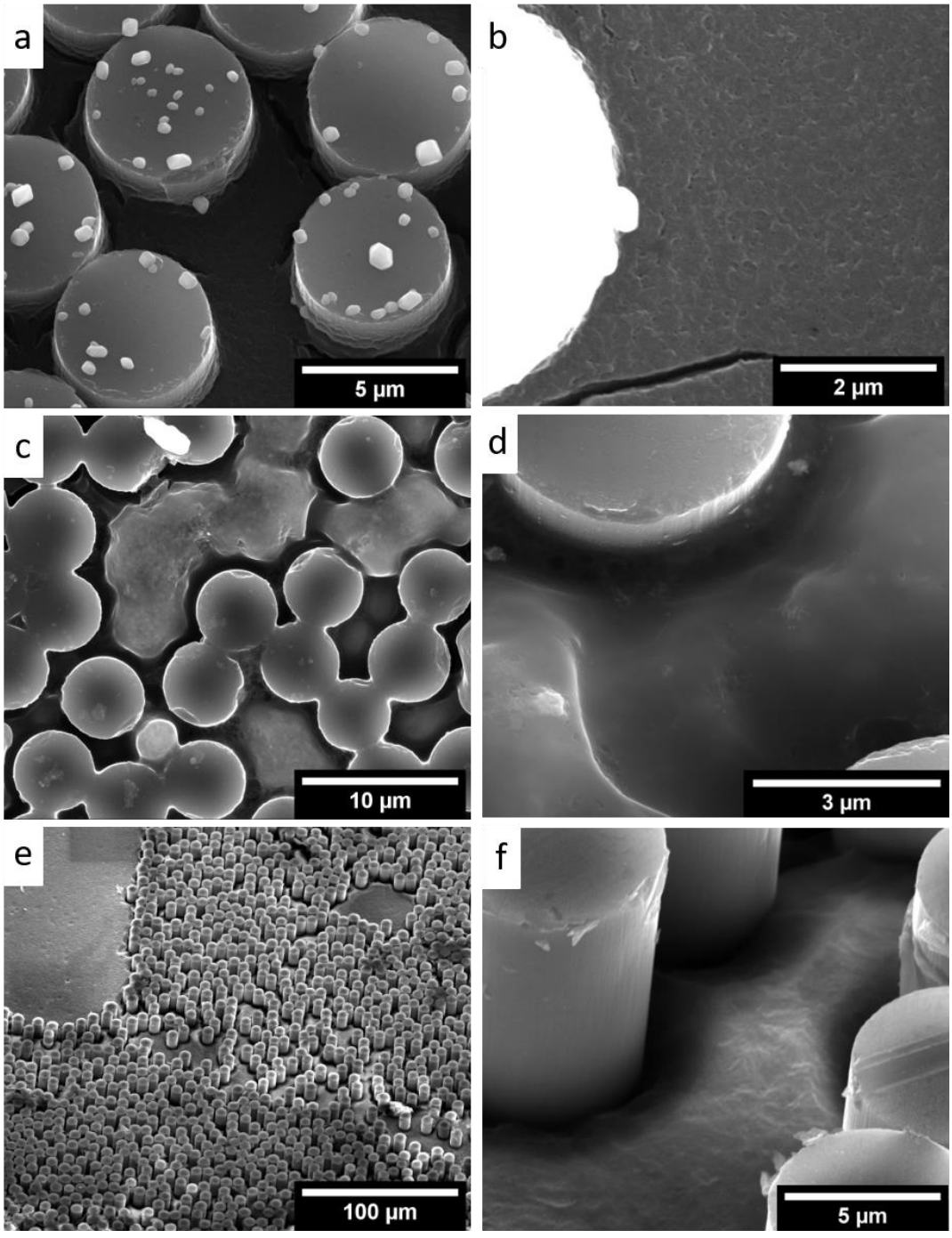

Figure 72. Scanning electron micrographs of the etched carbon fiber reinforced PEEK surfaces. a) and b) were etched for 5 minutes, where the etchant did not contain sulfuric acid. c) and d) were etched for 5 minutes where the etchant contained sulfuric acid. e) and f) were etched for 50 minutes, where the etchant did not contain sulfuric acid.

The scanning electron micrographs of the etched PEEK surfaces can be seen in Figure 72. The top two micrographs show a composite etched with a permanganate etchant, without the inclusion of sulfuric acid, for a duration of five minutes. The absence of etched PEEK on the composite surface is clearly visible as the fibers protrude slightly out of the matrix. The contaminate particles are thought to be contamination during the gold coating process prior to imaging. When the fiber is overexposed, the fine microstructure in the PEEK can be observed. While unique texture is apparent on the polymer surface, this structure does not resemble the spherulitic structure as previously reported. A permanganate including sulfuric acid was used to etch the sample shown in the middle two micrographs, also for a duration of five minutes. In general, this etchant appeared to be much more aggressive at the fiber interfaces, where the maximum amount of material was removed. Again, no fine spherulitic details can be observed in the PEEK matrix. Lastly, the permanganate etchant without sulfuric acid was used to etch the composites for 50 minutes, as seen in the bottom two micrographs. A more substantial amount of the matrix was removed with this treatment, and the surface texture began to resemble that of the spherulites expected, though this detail was not observed consistently across the sample. Again, the polymer at the fiber interfaces appeared to have the largest rates of dissolution. While the crystalline morphology did not become readily obvious with the various etching solutions and durations tested, an interesting observation on local dissolution rates was observed.

Atomic force microscopy was also used to interrogate the matrix microstructure after etching, as seem in Figure 73. This removed the requirement for a conductive surface, as is the case in SEM, and therefore no gold coating was required prior to imaging. This removes the possibility that any fine features are obstructed by the coating, or that any restructuring of the polymer takes

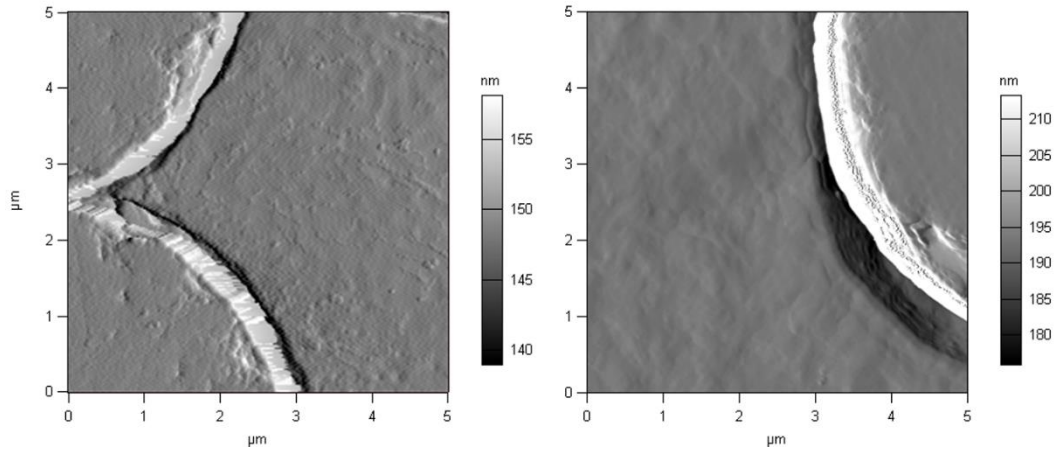

Figure 73. Atomic force micrographs (height) of the surface of etched carbon fiber reinforced PEEK AM composites.

place due to the elevated temperatures during deposition. The sample was etched with the same permanganate etchant without sulfuric acid for five minutes. Again, the matrix does not seem to exhibit topology indicative of spherulites or polymer crystallinity. As in the case of SEM, however, the elevated dissolution rates at the fiber interfaces can be observed. In general, crystalline regions of a polymer have higher thermodynamic stability, and therefore are more resistant to dissolution. The elevated dissolution rates at the fiber interfaces may indicate an amorphous interphase polymer structure.

An example of the elastic, plastic, and frictional energy contributions during each loading and unloading cycle is shown in Figure 74. Each point corresponds to the loading/unloading/reloading indentations at the same depth, which advance in 100nm increments up to a maximum depth of 1 micron. Each line shown in the plot corresponds to an individual fiber on which cyclic indentation was performed. Crack formation is typically considered to occur when the slope of total plastic deformation increases abruptly, which appears to occur around 500nm indentation depths. Overall, there is a relatively small spread in the energy

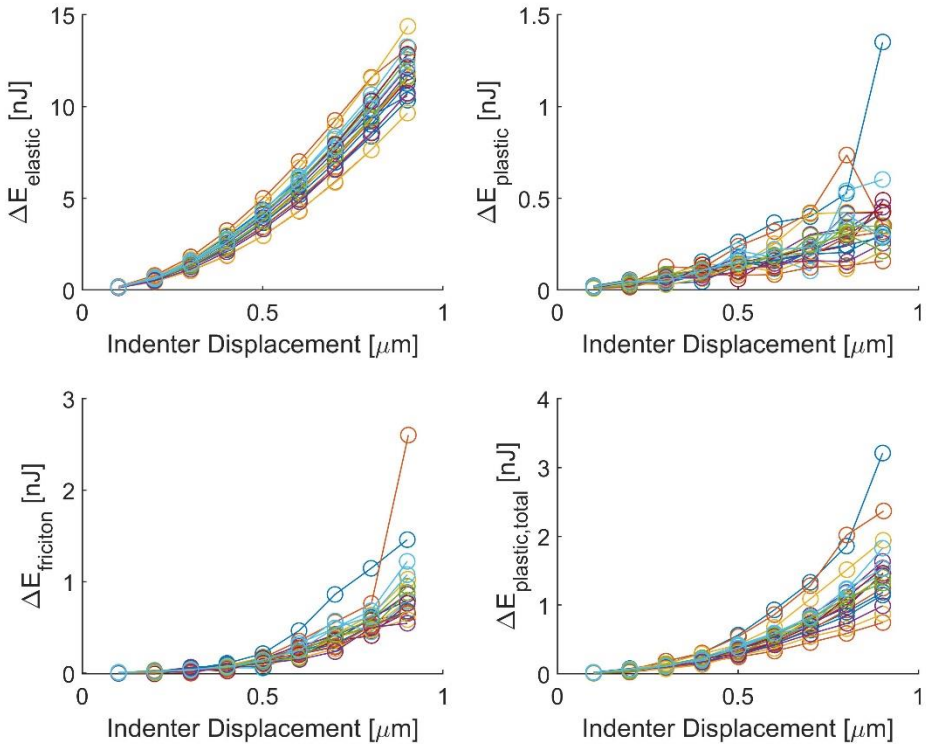

Figure 74. Elastic, plastic, and frictional energy contributions during loading/unloading cycles in single fiber pushout test for Ref (untreated) sample.

contribution values across the fibers tested, providing confidence in the representative nature of this analysis.

The average energy contribution for all fibers tested was calculated at each indentation depth for the three samples tested, as seen in Figure 75. Interestingly, the 250C treated sample displayed the lowest $\Delta E_{elastic}$, indicating the lowest stiffness of the fiber-matrix system. This was followed by the Ref sample, and the 300C HIP samples displayed the largest $\Delta E_{elastic}$ at each indentation depth. The same trend continuous for $\Delta E_{plastic}$ and $\Delta E_{friction}$. The increase in matrix stiffness brought on by the increase in polymer crystallinity through annealing at 300°C likely results in the larger forces observed at lower indentation depths. The higher interfacial stresses can then

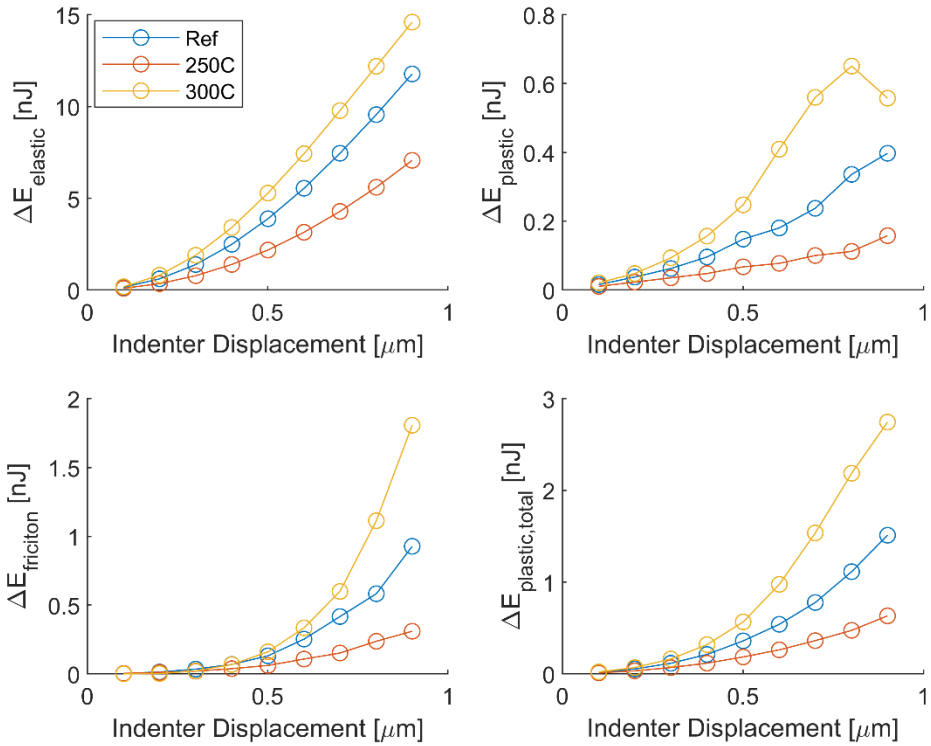

Figure 75. Average elastic, plastic, and frictional energy contributions during loading/unloading cycles in single fiber pushout test for Ref, 200C, and 300C treated sample.

result in elevated quantities of plastic deformation in the matrix and frictional energy at the interface. The 250°C treated sample, however, did not show a significant change in crystallinity over the reference sample. It is possible that the reduction in plastic and frictional energies at each indentation depth is due to a reduction in the residual thermal stresses that likely remain from the additive manufacturing process.

Representative scatter plots for the reference, 250°C, and 300°C treated nanomechanical mapping results can be seen in Figure 76. While the nanomechanical mapping was originally intended to characterize the interphase thickness, a few other interesting pieces of information can be extracted from this characterization. The reference and 250°C displayed virtually identical properties with respect to the fiber properties, matrix properties, and interphase thickness. The

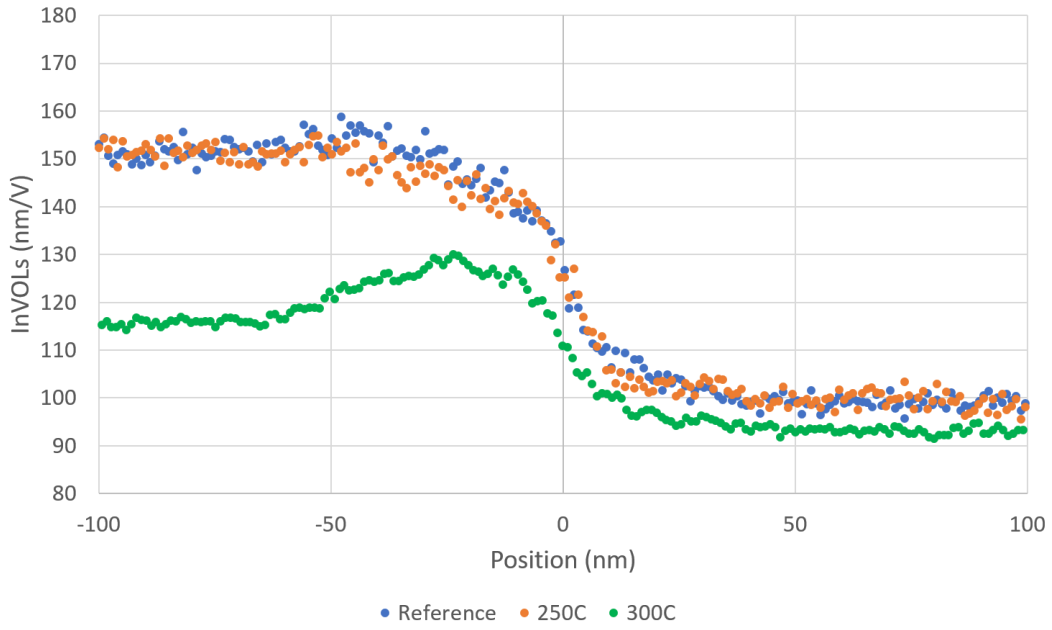

Figure 76. Nanomechanical map of the carbon fiber-PEEK interphase.

300°C HIP sample, however, displays markedly different matrix properties and interphase behavior. The PEEK stiffness appears to be significantly larger than that of the reference and 250°C treated samples. This is likely due to the higher degree of crystallinity in this material. Additionally, the matrix compliance begins to increase slightly near the carbon fiber surface. This may support the findings observed in the etching portion of this study, as an increased compliance in the matrix indicates a more amorphous polymer structure located in close proximity to the fiber surface. This would allow the etchant to remove material at a higher rate directly at the fiber interfaces. Over time this also increases the surface area exposed to the etchant at the fiber interphase, which results in a larger difference between the thickness of polymer removed near or far from the carbon fiber interfaces.

6.4 Conclusions

The investigation into the fiber-matrix interphase properties using etching, single fiber pushout nanoindentation, and nanomechanical mapping of HIP treated AM CFRPs was performed. In the

context of the previous HIP study results, this investigation was able to provide valuable insight into the complex process-structure-property relationships of the system. While replication of PEEK etching to observe spherulite microstructure was not found to be successful, an important distinction between local dissolution rates was observed. In general, etching rates appeared to be greater at the fiber interfaces than in the bulk PEEK at a distance from the fibers. This indicated that the local morphology at fiber interfaces was more amorphous than the 'bulk' polymer.

The energy-based analysis of the single fiber pushout test illuminated interesting variations in the interphase behavior between the specimens tested. The 300°C sample displayed the highest stiffness interface, which likely resulted in additional plastic deformation and frictional losses at a given indentation depth. Again, this can be attributed to the larger DOC of the polymer found in the 300°C treated composite. In contrast, the 250°C treated sample displayed the lowest stiffness, plastic deformation, and frictional losses. While the DOC of the 250°C treated sample was found to be slightly larger than that of the reference sample, it is likely that this effect was mitigated by a corresponding reduction in residual thermal stress at the fiber-matrix interphase.

Lastly, nanomechanical mapping was able to provide additional insight into the process-structure-property relationships in these composites. As expected from the similar DOC measured between reference and 250°C samples, the stiffness of the matrix and carbon fiber, along with the interphase thickness, were all found to be virtually identical. The higher DOC in the 300°C sample appears to increase the stiffness of the polymer, though a relatively amorphous microstructure can be found within approximately 50nm of the fiber interface.

In the context of the previous HIP investigation of AM continuous fiber reinforced PEEK composites, it can be concluded that treatment of the polymer at 250°C is sufficient to allow for a reduction in the composite void content without causing a significant change to the polymer

microstructure. As the Atm treated sample would likely have undergone a similar change in residual thermal stresses and did not experience an improvement in mechanical performance over the reference material, it does not appear that this change in interfacial behavior contributes significantly to the properties of the composite. At treatment temperatures of 300°C, however, the significant changes in the polymer microstructure result in a reduction in properties over the 250°C sample, despite achieving an additional reduction in void content. This is likely due to the increase in brittleness of the matrix, which becomes more susceptible to failure from stress concentration of internal voids. Additionally, the stiff interface observed between the fiber and matrix may also result in interfacial debonding at lower strains.

Chapter 7. Conclusions and Future Work

We investigated some of the key barriers for the adoption of additively manufactured composites in high performance applications. Many aspects of the processing-structure-property relationships in continuous fiber AM composites were investigated, along with some of the tools required to design and model AM composite parts. The body of research covered in this dissertation can serve as a foundation for the transition of AM fiber reinforced composites from laboratory and prototyping purposes into high-performance applications.

In Chapter 3, a method for implementing finite element analysis (FEA) to model the properties of AM parts with curved fiber paths was developed. In general, the model predictions of failure and maximum gauge stress at failure were in close agreement with experimental results. Finally, some simple design guidelines were outlined based on the observations of stress distribution and failure from the models tested. This model demonstrates a viable method to predict the internal state of stress, failure modes and failure locations of continuous fiber AM composites.

Chapter 4 detailed the implementation of topology and fiber placement optimization to improve the specific stiffness of three benchmark designs. The experimental stiffness values were measured and compared with FEA predictions, which in general were in close agreement. The improvement in specific stiffness compared against reference geometries was then made, finding an increase in specific strength from between 37 and 245%. This study demonstrates the significant value of utilizing optimization in design to improve the properties of composite parts, for which AM is inherently well-suited.

In Chapter 5, post-processing of composite parts using hot isostatic pressing (HIP) was utilized to reduce internal void content and allow for restructuring of the polymer matrix. This addresses

one of the most significant limitations of AM composites, where void content can easily fall above 10 vol.%. The void content and mechanical properties were correlated to the post-processing conditions, which found a maximum improvement from treatment at 250°C and 200psi for three hours for AS4C reinforced PEEK AM composites. This treatment was found to improve the in-plane and interlaminar mechanical properties. Interestingly, while treatment at a higher temperature (300°C) resulted in a further reduction in void content, it was found to produce lower improvements than the 250°C treatment. This was attributed to significant change in polymer crystallinity that occurs at 300°C compared with 250°C, which embrittles the matrix resulting in larger stress concentrations from internal porosity.

Lastly, in Chapter 6, nano- and micro-scale structure and properties in HIP treated AM PEEK matrix composites were investigated. The polymer and interphase microstructures were investigated using etching, microscopy, and nanomechanical mapping techniques. The fiber-matrix interphase properties were also investigated using nanoindentation single fiber pushout tests, utilizing an energy-based approach for analysis. No evidence of transcrystallinity was observed, and both etching and nanomechanical mapping indicated an amorphous polymer structure at the fiber-matrix interface. Additionally, while the polymer properties were unchanged between the reference and 250°C treated samples, the 300°C displayed a significant increase in polymer stiffness. This stiffness can be attributed to the corresponding increase in polymer crystallinity, which is known to be inversely proportional to the polymer ductility. While slight changes in the interfacial properties were observed with the single fiber pushout tests, these appear to be less significant to the overall composite properties than the void content and polymer crystallinity.

7.1 Future Research Prospects

As AM CFRPs utilizing continuous fiber reinforcement is still budding technology, there are many opportunities for advancement. A handful of such opportunities are outlined below, though it should be noted that this list is not intended to be comprehensive.

- Although most studies so far have focused on characterizing the tensile properties of AM composites, investigations of non-tensile properties and failure/fracture mechanics are essential for the design of AM parts.
- Further, to improve mechanical properties of AM composites, an understanding of the relationships among the AM process, structure of printed parts, and their mechanical performance is essential.
- Process modeling can facilitate optimization of the AM process and eventually result in printed parts with enhanced performance. In this regard, there is a lack of understanding of polymer rheology and morphology during the printing of short fiber– and continuous fiber–reinforced polymers.
- Another area that may require even more focused attention and research investment is improving the Z-direction properties of FDM parts. FDM parts are inherently weak in the out-of-plane direction, and this deficiency can adversely impact their applications.
- Although the properties of AM polymers are tremendously improved by the addition of carbon fibers, they are still greatly inferior to those of conventionally manufactured composites. AM design freedom can be used to produce parts with optimized geometries and infill patterns. Such parts can potentially compete with and even surpass the performance of conventional composites. To this end, frameworks for the design optimization of AM parts need to be developed.
- As demonstrated by the theoretical predictions, longer fibers (1 mm and longer) and higher volume fractions in forms processable for 3D printing are required to achieve superior mechanical properties and high translation of fiber properties.
- Few thermosetting resins can be 3D printed. Novel chemistries and nanocomposites that can enable high-performance AM parts are needed.

- Various defects are introduced during AM. Understanding how these defects are formed can lead to methods for reducing or eliminating them. This will, in turn, enable better properties and accelerate the certification process for these novel materials.
- While this study covered stiffness-based design optimization, optimizing strength for similar benchmark cases would be a valuable contribution to the field.

REFERENCES

[1] Sujit Das JW, Devin West. Global Carbon Fiber Composites Supply Chain Competitiveness Analysis. In: Schexnayder SM, editor.: Oak Ridge National Laboratory; 2016. p. 1-116.

[2] Park KY, Choi JH, Lee DG. Delamination-Free and High-Efficiency Drilling of Carbon-Fiber-Reinforced Plastics. J Compos Mater. 1995;29(15):1988-2002.

[3] Robertson ID, Yourdkhani M, Centellas PJ, Aw JE, Ivanoff DG, Goli E, et al. Rapid energy-efficient manufacturing of polymers and composites via frontal polymerization. Nature. 2018;557(7704):223-7.

[4] Bikas H, Stavropoulos P, Chryssolouris G. Additive manufacturing methods and modelling approaches: a critical review. The International Journal of Advanced Manufacturing Technology. 2016;83(1-4):389-405.

[5] Ning FD, Cong WL, Qiu JJ, Wei JH, Wang SR. Additive manufacturing of carbon fiber reinforced thermoplastic composites using fused deposition modeling. Compos Part B-Eng. 2015;80:369-78.

[6] Love LJ, Kunc V, Rios O, Duty CE, Elliott AM, Post BK, et al. The importance of carbon fiber to polymer additive manufacturing. J Mater Res. 2014;29(17):1893-8.

[7] CINCINNATI. CIBAAM 3D Printed Projects. 2018.

[8] Compton BG, Post BK, Duty CE, Love L, Kunc V. Thermal analysis of additive manufacturing of large-scale thermoplastic polymer composites. Additive Manufacturing. 2017;17:77-86.

[9] Kempen K, Yasa E, Thijs L, Kruth JP, Van Humbeeck J. Microstructure and mechanical properties of Selective Laser Melted 18Ni-300 steel. Physcs Proc. 2011;12:255-63.

[10] Manfredi D, Calignano F, Krishnan M, Canali R, Ambrosio EP, Atzeni E. From Powders to Dense Metal Parts: Characterization of a Commercial AlSiMg Alloy Processed through Direct Metal Laser Sintering. Materials. 2013;6(3):856-69.

[11] Anubis3D. 2017.

[12] Stratasys, http://www.stratasys.com/. 2017.

[13] Hall W, Palmer S. Student Opportunities in Materials Design and Manufacture: Introducing a New Manufacturing with Composites Course. J Mater Educ. 2015;37(3-4):155-68.

[14] 3DXTECH. 2019.

[15] Corporation D. 2017.

[16] Li P, Xu WY. The diagnosis of manufacturing defects in composite material radome based on antenna's far field data. Mater Res Innov. 2015;19:277-82.

[17] Apium, https://apiumtec.com/en/3d-printer/. 2017.

[18] Dielectric Corporation, http://www.dielectriccorp.com/. 2017.

[19] Parandoush P, Lin D. A review on additive manufacturing of polymer-fiber composites. Compos Struct. 2017;182:36-53.

[20] Wang X, Jiang M, Zhou ZW, Gou JH, Hui D. 3D printing of polymer matrix composites: A review and prospective. Compos Part B-Eng. 2017;110:442-58.

[21] Brenken B, Barocio E, Favaloro A, Kunc V, Pipes RB. Fused filament fabrication of fiber-reinforced polymers: A review. Additive Manufacturing. 2018;21:1-16.

[22] Hofstätter T, Pedersen DB, Tosello G, Hansen HN. State-of-the-art of fiber-reinforced polymers in additive manufacturing technologies. J Reinf Plast Comp. 2017;36(15):1061-73.

[23] Tekinalp HL, Kunc V, Velez-Garcia GM, Duty CE, Love LJ, Naskar AK, et al. Highly oriented carbon fiber-polymer composites via additive manufacturing. Compos Sci Technol. 2014;105:144-50.

[24] Duty C, Ajinjeru C, Kishore V, Compton B, Hmeidat N, Chen X, et al. A Viscoelastic Model for Evaluating Extrusion-Based Print Conditions. Solid Freeform Fabrication Symposium2017.

[25] Kishore V, Chen X, Ajinjeru C, Hassen AA, Lindahl J, Faila J, et al. Additive Manufacturing of High Performance Semi-crystalline Thermoplastics and Their Composites. 27th Annual International Solid Freeform Fabrication Symposium, Austin, TX2016. p. 906-15.

[26] Ajinjeru C, Kishore V, Liu P, Hassen AA, Lindahl J, Kunc V, et al. Rheological evaluation of high temperature polymers to identify successful extrusion parameters. Solid Freeform Fabrication Symposium2017.

[27] Kishore V, Ajinjeru C, Nycz A, Post B, Lindahl J, Kunc V, et al. Infrared preheating to improve interlayer strength of big area additive manufacturing (BAAM) components. Additive Manufacturing. 2017;14:7-12.

[28] Duty C, Failla J, Kim S, Lindahl J, Post B, Love L, et al. REDUCING MECHANICAL ANISOTROPY IN EXTRUSION-BASED PRINTED PARTS.

[29] Werken Nvd, Koirala P, Ghorbani J, Abel M, Tehrani M. Improving Properties of Additively Manufactured Carbon Fiber Composites via Post Pressing. Proceedings of the 34th Annual American Society for Composites Technical Conference2019.

[30] Zhong WH, Li F, Zhang ZG, Song LL, Li ZM. Short fiber reinforced composites for fused deposition modeling. Mat Sci Eng a-Struct. 2001;301(2):125-30.

[31] Shofner ML, Lozano K, Rodriguez-Macias FJ, Barrera EV. Nanofiber-reinforced polymers prepared by fused deposition modeling. J Appl Polym Sci. 2003;89(11):3081-90.

[32] Shofner ML, Rodriguez-Macias FJ, Vaidyanathan R, Barrera EV. Single wall nanotube and vapor grown carbon fiber reinforced polymers processed by extrusion freeform fabrication. Compos Part a-Appl S. 2003;34(12):1207-17.

[33] Zhang W, Cotton C, Sun J, Heider D, Gu B, Sun B, et al. Interfacial bonding strength of short carbon fiber/acrylonitrile-butadiene-styrene composites fabricated by fused deposition modeling. Composites Part B: Engineering. 2018;137:51-9.

[34] Hofstätter T, Gutmann IW, Koch T, Pedersen DB, Tosello G, Heinz G, et al. Distribution and orientation of carbon fibers in polylactic acid parts produced by fused deposition modeling. Proceedings of ASPE summer topical meeting2016.

[35] Huang Y, Young RJ. Interfacial micromechanics in thermoplastic and thermosetting matrix carbon fibre composites. Composites Part A: Applied Science And Manufacturing. 1996;27(10):973-80.

[36] Ning FD, Cong WL, Hu YB, Wang H. Additive manufacturing of carbon fiber-reinforced plastic composites using fused deposition modeling: Effects of process parameters on tensile properties. J Compos Mater. 2017;51(4):451-62.

[37] Jiang D, Smith DE. Anisotropic mechanical properties of oriented carbon fiber filled polymer composites produced with fused filament fabrication. Additive Manufacturing. 2017;18:84-94.

[38] Ferreira RTL, Amatte IC, Dutra TA, Burger D. Experimental characterization and micrography of 3D printed PLA and PLA reinforced with short carbon fibers. Compos Part B-Eng. 2017;124:88-100.

[39] Liao G, Li Z, Cheng Y, Xu D, Zhu D, Jiang S, et al. Properties of oriented carbon fiber/polyamide 12 composite parts fabricated by fused deposition modeling. Mater Design. 2018;139:283-92.

[40] Love LJ, Duty C. Cincinnati Big Area Additive Manufacturing (BAAM). info ornl gov http://info ornl gov/sites/publications/files/Pub54708 pdf. 2015.

[41] Duty CE, Kunc V, Compton B, Post B, Erdman D, Smith R, et al. Structure and mechanical behavior of Big Area Additive Manufacturing (BAAM) materials. Rapid Prototyping Journal. 2017;23(1):181-9.

[42] Fu SY, Lauke B, Mai YW. Science and Engineering of Short Fibre Reinforced Polymer Composites. Science and Engineering of Short Fibre Reinforced Polymer Composites. 2009:1-338.

[43] Kunc V, Kishore V, Chen X, Ajinjeru C, Duty C, Hassen AA. High performance poly (etherketoneketone)(PEKK) composite parts fabricated using Big Area Additive Manufacturing (BAAM) processes. Oak Ridge National Lab.(ORNL), Oak Ridge, TN (United States). Manufacturing Demonstration Facility (MDF); 2016.

[44] Ajinjeru C, Kishore V, Chen X, Lindahl J, Sudbury Z, Arabi A, et al. The Influence of Rheology on Melt Processing Conditions of Amorphous Thermoplastics for Big Area Additive Manufacturing (BAAM). 27th Annual International Solid Freeform Fabrication Symposium, Austin, TX2016. p. 754-62.

[45] Ajinjeru C, Kishore V, Liu P, Lindahl J, Hassen AA, Kunc V, et al. Determination of melt processing conditions for high performance amorphous thermoplastics for large format additive manufacturing. Additive Manufacturing. 2018;21:125-32.

[46] Kishore V, Ajinjeru C, Liu P, Lindahl J, Hassen A, Kunc V, et al. Predicting sharkskin instability in extrusion additive manufacturing of reinforced thermoplastics.

[47] Sudbury Z, Duty C, Kunc V, Kishore V, Ajinjeru C, Failla J, et al. Characterizing Material Transition for Functionally Graded Material Using Big Area Additive Manufacturing. Annu Int Solid Free Fabr Symp2016.

[48] Lewicki JP, Rodriguez JN, Zhu C, Worsley MA, Wu AS, Kanarska Y, et al. 3D-Printing of Meso-structurally Ordered Carbon Fiber/Polymer Composites with Unprecedented Orthotropic Physical Properties. Scientific Reports. 2017;7.

[49] Hoey JM, Lutfurakhmanov A, Schulz DL, Akhatov IS. A Review on Aerosol-Based Direct-Write and Its Applications for Microelectronics. J Nanotechnol. 2012.

[50] Compton BG, Kemp JW, Novikov TV, Pack RC, Nlebedim CI, Duty CE, et al. Direct-write 3D printing of NdFeB bonded magnets. Materials and Manufacturing Processes. 2018;33(1):109-13.

[51] Griffini G, Invernizzi M, Levi M, Natale G, Postiglione G, Turri S. 3D-printable CFR polymer composites with dual-cure sequential IPNs. Polymer. 2016;91:174-9.

[52] Invernizzi M, Natale G, Levi M, Turri S, Griffini G. UV-Assisted 3D Printing of Glass and Carbon Fiber-Reinforced Dual-Cure Polymer Composites. Materials. 2016;9(7).

[53] Bhushan B, Caspers M. An overview of additive manufacturing (3D printing) for microfabrication. Microsystem Technologies. 2017;23(4):1117-24.

[54] Karalekas DE. Study of the mechanical properties of nonwoven fibre mat reinforced photopolymers used in rapid prototyping. Materials & Design. 2003;24(8):665-70.

[55] Goodridge R, Shofner M, Hague R, McClelland M, Schlea M, Johnson R, et al. Processing of a Polyamide-12/carbon nanofibre composite by laser sintering. Polym Test. 2011;30(1):94-100.

[56] Yan CZ, Hao L, Xu L, Shi YS. Preparation, characterisation and processing of carbon fibre/polyamide-12 composites for selective laser sintering. Composites Science and Technology. 2011;71(16):1834-41.

[57] Jansson A, Pejryd L. Characterisation of carbon fibre-reinforced polyamide manufactured by selective laser sintering. Additive Manufacturing. 2016;9:7-13.

[58] Wu J, Chen H, Wu Q, Liu HB, Luo ZJ. Surface modification of carbon fibers and the selective laser sintering of modified carbon fiber/nylon 12 composite powder. Mater Design. 2017;116:253-60.

[59] Salmoria GV, Paggi RA, Lago A, Beal VE. Microstructural and mechanical characterization of PA12/MWCNTs nanocomposite manufactured by selective laser sintering. Polym Test. 2011;30(6):611-5.

[60] Yuan S, Zheng Y, Chua CK, Yan Q, Zhou K. Electrical and thermal conductivities of MWCNT/polymer composites fabricated by selective laser sintering. Composites Part A: Applied Science and Manufacturing. 2018;105:203-13.

[61] Bai J, Goodridge RD, Hague RJ, Song M, Okamoto M. Influence of carbon nanotubes on the rheology and dynamic mechanical properties of polyamide-12 for laser sintering. Polymer Testing. 2014;36:95-100.

[62] Quan ZZ, Larimore Z, Wu A, Yu JY, Qin XH, Mirotznik M, et al. Microstructural design and additive manufacturing and characterization of 3D orthogonal short carbon fiber/acrylonitrile-butadiene-styrene preform and composite. Composites Science and Technology. 2016;126:139-48.

[63] Fu SY, Lauke B. Effects of fiber length and fiber orientation distributions on the tensile strength of short-fiber-reinforced polymers. Composites Science and Technology. 1996;56(10):1179-90.

[64] Werken Nd, S.Reese M, R.Taha M, MehranTehrani. Investigating the effects of fiber surface treatment and alignment on mechanical properties of recycled carbon fiber composites. Composites Part A: Applied Science and Manufacturing. 2019;119:38-47.

[65] Fu SY, Lauke B. The elastic modulus of misaligned short-fiber-reinforced polymers. Composites Science and Technology. 1998;58(3-4):389-400.

[66] Zhong WH, Li F, Zhang ZG, Song LL, Li ZM. Research on rapid-prototyping/part manufacturing (RP&M) for the continuous fiber reinforced composite. Mater Manuf Process. 2001;16(1):17-26.

[67] Hu QX, Duan YC, Zhang HG, Liu DL, Yan BA, Peng FJ. Manufacturing and 3D printing of continuous carbon fiber prepreg filament. J Mater Sci. 2018;53(3):1887-98.

[68] Werken Nvd, Hurley J, Khanbolouki P, Sarvestani AN, Tamijani AY, Tehrani M. Design considerations and modeling of fiber reinforced 3D printed parts. Composites Part B: Engineering. 2019;160:684-92.

[69] Van Der Klift F, Koga Y, Todoroki A, Ueda M, Hirano Y, Matsuzaki R. 3D printing of continuous carbon fibre reinforced thermo-plastic (CFRTP) tensile test specimens. Open Journal of Composite Materials. 2015;6(01):18.

[70] Melenka GW, Cheung BKO, Schofield JS, Dawson MR, Carey JP. Evaluation and prediction of the tensile properties of continuous fiber-reinforced 3D printed structures. Compos Struct. 2016;153:866-75.

[71] Matsuzaki R, Ueda M, Namiki M, Jeong TK, Asahara H, Horiguchi K, et al. Three-dimensional printing of continuous-fiber composites by in-nozzle impregnation. Scientific Reports. 2016;6.

[72] Tian XY, Liu TF, Yang CC, Wang QR, Li DC. Interface and performance of 3D printed continuous carbon fiber reinforced PLA composites. Compos Part a-Appl S. 2016;88:198-205.

[73] Tian XY, Liu TF, Wang QR, Dilmurat A, Li DC, Ziegmann G. Recycling and remanufacturing of 3D printed continuous carbon fiber reinforced PLA composites. J Clean Prod. 2017;142:1609-18.

[74] Li NY, Li YG, Liu ST. Rapid prototyping of continuous carbon fiber reinforced polylactic acid composites by 3D printing. J Mater Process Tech. 2016;238:218-25.

[75] Liu ST, Li YG, Li NY. A novel free-hanging 3D printing method for continuous carbon fiber reinforced thermoplastic lattice truss core structures. Materials & Design. 2018;137:235-44.

[76] Vaneker THJ. Material extrusion of continuous fiber reinforced plastics using commingled yarn. Proc Cirp. 2017;66:317-22.

[77] Tse L, Kapila S, Barton K. CONTOURED 3D PRINTING OF FIBER REINFORCED POLYMERS. 2016.

[78] Mori KI, Maeno T, Nakagawa Y. Dieless forming of carbon fibre reinforced plastic parts using 3D printer. Procedia Engineer. 2014;81:1595-600.

[79] Baumann F, Scholz J, Fleischer J. Investigation of a new approach for additively manufactured continuous fiber-reinforced polymers. 1st Cirp Conference on Composite Materials Parts Manufacturing (Cirp Ccmpm 2017). 2017;66:323-8.

[80] Brooks H, Molony S. Design and evaluation of additively manufactured parts with three dimensional continuous fibre reinforcement. Materials & Design. 2016;90:276-83.

[81] Yao XH, Luan CC, Zhang DM, Lan LJ, Fu JZ. Evaluation of carbon fiber-embedded 3D printed structures for strengthening and structural-health monitoring. Materials & Design. 2017;114:424-32.

[82] Hao WF, Liu Y, Zhou H, Chen HS, Fang DN. Preparation and characterization of 3D printed continuous carbon fiber reinforced thermosetting composites. Polym Test. 2018;65:29-34.

[83] Gregory ED, Juarez PD. In-Situ Thermography of Automated Fiber Placement Parts. Aip Conf Proc. 2018;1949.

[84] Walbran M, Turner K, McDaid AJ. Customized 3D printed ankle-foot orthosis with adaptable carbon fibre composite spring joint. Cogent Eng. 2016;3(1).

[85] Dickson AN, Barry JN, McDonnell KA, Dowling DP. Fabrication of continuous carbon, glass and Kevlar fibre reinforced polymer composites using additive manufacturing. Additive Manufacturing. 2017;16:146-52.

[86] Goh GD, Dikshit V, Nagalingam AP, Goh GL, Agarwala S, Sing SL, et al. Characterization of mechanical properties and fracture mode of additively manufactured carbon fiber and glass fiber reinforced thermoplastics. Mater Design. 2018;137:79-89.

[87] Justo J, Tavara L, Garcia-Guzman L, Paris F. Characterization of 3D printed long fibre reinforced composites. Compos Struct. 2018;185:537-48.

[88] Impossible Objects. 2019.

[89] Lammering R, Gabbert U, Sinapius M, Schuster T, Wierach P. Structural Health Monitoring on the SARISTU Full Scale Door Surround Structure. Stud Neurosci. 2018:463-73.

[90] Liu F, Zhang WX, Xu K, Deng HC, Ding XL. A Planar Mechanism with Variable Topology for Automated Fiber Placement. 2018 International Conference on Reconfigurable Mechanisms and Robots (Remar). 2018.

[91] Sloan J. Arevo Labs launches 3D printing platform for composite parts fabrication. CompositesWorld.

[92] Mantis Composites. 2019.

[93] Shadmehri F, Hoa SV, Fortin-Simpson J, Ghayoor H. Effect of in situ treatment on the quality of flat thermoplastic composite plates made by automated fiber placement (AFP). Adv Manuf-Polym Comp. 2018;4(2):41-7.

[94] Ge XF. Evaluating and optimization of 7-DOF automated fiber placement robotic manipulator performance index based on AdaBoost algorithm. J Comput Methods Sci. 2018;18(3):749-57.

[95] Shah D, Gao JC, Pashkevich A, Caro S, Courtemanche B. Computer-Aided Design and Optimization of a Redundant Robotic System for Automated Fiber Placement Process. Disruptive Innovation in Mechanical Engineering for Industry Competitiveness. 2018;1983.

[96] Hosseini SMA, Baran I, Akkerrnan R. An Experimental Investigation On The Therma Field Of Overlapping Layers In Laser-Assisted Tape Winding Process. Proceedings of 21st International Esaform Conference on Material Forming (Esaform 2018). 2018;1960.

[97] Grossman D. Juno Took 3D-Printed Parts Further Into Space Than Ever. Popular Mechanics. www.popularmechanics.com2016.

[98] 3-D Printed Parts - in Space! Boeing2015.

[99] Werner D. SSL additively expands additive manufacturing from brackets to antenna towers. SpaceNews2018.

[100] Winick E. Additive Manufacturing in the Aerospace Industry. engineering.com2017.

[101] SPACEX LAUNCHES 3D-PRINTED PART TO SPACE, CREATES PRINTED ENGINE CHAMBER. SpaceX.com2014.

[102] VIALVA T. DSTA, AIRBUS, AND BOEING TO USE ADDITIVE MANUFACTURING FOR AIRCRAFT MAINTENANCE. 3dprintingindustry.com2018.

[103] Goh G, Agarwala S, Goh G, Dikshit V, Sing SL, Yeong WY. Additive manufacturing in unmanned aerial vehicles (UAVs): challenges and potential. Aerosp Sci Technol. 2017;63:140-51.

[104] Goh GD, Agarwala S, Goh GL, Dikshit V, Sing SL, Yeong WY. Additive Additive manufacturing in unmanned aerial vehicles (UAVs): Challenges and potential. Aerospace Science and Technology. 2017;63:140-51.

[105] Carl P. Jones EHR, Mary Beth Koelbl, Chris Singer. ADDITIVE MANUFACTURING A LIQUID HYDROGEN ROCKET ENGINE. NASA Technical Reports Server.

[106] COMTEX GNv. Aerojet Rocketdyne Successfully Tests Engine Made Entirely With Additive Manufacturing. MarketWatch.com2014.

[107] Drew J. Skunk Works Sees Big Opportunity For 'Attritable' UAVs. AviationWeek.com2017.

[108] Cooney M. Air Force envisioning swarms of tiny, inexpensive, almost disposable drones. NetworkWorld2014.

[109] Axe D. The U.S. Air Force's Next Killer Drone Is Disposable. WarisBoring.com2017.

[110] Espalin D, Muse DW, MacDonald E, Wicker RB. 3D Printing multifunctionality: structures with electronics. The International Journal of Advanced Manufacturing Technology. 2014;72(5-8):963-78.

[111] MacDonald E, Espalin D, Doyle D, Muñoz J, Ambriz S, Coronel J, et al. Fabricating patch antennas within complex dielectric structures through multi-process 3D printing. Journal of Manufacturing Processes. 2018;34:197-203.

[112] Prater T, Bean Q, Beshears R, Rolin T, Werkheiser N, Ordonez E, et al. Summary report on phase I results from the 3D printing in zero g technology demonstration mission, volume I. 2016.

[113] Buck J. Space Station 3-D Printer Builds Ratchet Wrench To Complete First Phase Of Operations. NASA.gov2017.

[114] Buck J. NASA Announces Opportunities to Advance 'Tipping Point' and Emerging Space Technologies. NASA.gov2015.

[115] Love LJ. Utility of big area additive manufacturing (BAAM) for the rapid manufacture of customized electric vehicles. Oak Ridge National Laboratory (ORNL); Manufacturing Demonstration Facility (MDF); 2015.

[116] M.R. Talagani SD, R. Dutton, C. Godines, H. Baid, F. Abdi, V. Kunc, B. Compton, S. Simunovic, C. Duty, L. Love, B. Post, and C. Blue. Numerical Simulation of Big Area Additive Manufacturing (3D Priting) of a Full Size Car. SAMPE Journal 2015;51(4):27-36.

[117] Nuttall D, Elliott A, Post B, Love L. Advanced Infusion Techniques with 3-D Printed Tooling. Oak Ridge National Lab.(ORNL), Oak Ridge, TN (United States). Manufacturing Demonstration Facility (MDF); 2016.

[118] Hassen AA, Springfield R, Lindahl J, Post B, Love L, Duty C, et al. The durability of large-scale additive manufacturing composite molds. Composites and Advanced Materials Expo (CAMX) Conference2016. p. 26-9.

[119] Li L, Post B, Kunc V, Elliott AM, Paranthaman MP. Additive manufacturing of near-net-shape bonded magnets: Prospects and challenges. Scripta Materialia. 2017;135:100-4.

[120] Li L, Tirado A, Conner BS, Chi M, Elliott AM, Rios O, et al. A novel method combining additive manufacturing and alloy infiltration for NdFeB bonded magnet fabrication. Journal of Magnetism and Magnetic Materials. 2017;438:163-7.

[121] Gray RW, Baird DG, Bohn JH. Thermoplastic composites reinforced with long fiber thermotropic liquid crystalline polymers for fused deposition modeling. Polym Composite. 1998;19(4):383-94.

[122] Pidcock GC, Panhuis MIH. Extrusion Printing of Flexible Electrically Conducting Carbon Nanotube Networks. Adv Funct Mater. 2012;22(22):4790-800.

[123] Leigh SJ, Bradley RJ, Purssell CP, Billson DR, Hutchins DA. A Simple, Low-Cost Conductive Composite Material for 3D Printing of Electronic Sensors. Plos One. 2012;7(11).

[124] Hu Z, Thiyagarajan K, Bhusal A, Letcher T, Fan QH, Liu Q, et al. Design of ultra-lightweight and high-strength cellular structural composites inspired by biomimetics. Compos Part B-Eng. 2017;121:108-21.

[125] Cheng L, Zhang P, Biyikli E, Bai JX, Robbins J, To A. Efficient design optimization of variable-density cellular structures for additive manufacturing: theory and experimental validation. Rapid Prototyping Journal. 2017;23(4):660-77.

[126] Drzal LT, Madhukar M. Fiber Matrix Adhesion and Its Relationship to Composite Mechanical-Properties. J Mater Sci. 1993;28(3):569-610.

[127] Olivier P, Cottu JP, Ferret B. Effects of Cure Cycle Pressure and Voids on Some Mechanical-Properties of Carbon-Epoxy Laminates. Composites. 1995;26(7):509-15.

[128] Werken Nvd, Allred R, Tehrani M. High Performance Recycled Carbon Fiber Polymer Composites. American Society for Composites 32nd Technical Conference2017.

[129] Tehrani M, Safdari M, Boroujeni AY, Razavi Z, Case SW, Dahmen K, et al. Hybrid carbon fiber/carbon nanotube composites for structural damping applications. Nanotechnology. 2013;24(15).

[130] Tehrani M, Boroujeni AY, Hartman TB, Haugh TP, Case SW, Al-Haik MS. Mechanical characterization and impact damage assessment of a woven carbon fiber reinforced carbon nanotube-epoxy composite. Composites Science and Technology. 2013;75:42-8.

[131] Nekoda van de Werken HT, Pouria Khanbolouki, Soydan Ozcan, Andrew Williams, Mehran Tehrani. Additively Manufactured Carbon Fiber-Reinforced Composites: State of the Art and Perspective. Additive Manufacturing, under review. 2019.

[132] van de Werken N, Hurley J, Khanbolouki P, Sarvestani AN, Tamijani AY, Tehrani M. Design considerations and modeling of fiber reinforced 3D printed parts. Composites Part B: Engineering. 2019;160:684-92.

[133] Liu J, Gaynor AT, Chen S, Kang Z, Suresh K, Takezawa A, et al. Current and future trends in topology optimization for additive manufacturing. Structural and Multidisciplinary Optimization. 2018;57(6):2457-83.

[134] Cheng L, Zhang P, Biyikli E, Bai J, Robbins J, To A. Efficient design optimization of variable-density cellular structures for additive manufacturing: theory and experimental validation. Rapid Prototyping J. 2017;23(4):660-77.

[135] Huang X, Zhou S, Xie Y, Li Q. Topology optimization of microstructures of cellular materials and composites for macrostructures. Computational Materials Science. 2013;67:397-407.

[136] Robbins J, Owen S, Clark B, Voth T. An efficient and scalable approach for generating topologically optimized cellular structures for additive manufacturing. Additive Manufacturing. 2016;12:296-304.

[137] Lu L, Yamamoto T, Otomori M, Yamada T, Izui K, Nishiwaki S. Topology optimization of an acoustic metamaterial with negative bulk modulus using local resonance. Finite Elements in Analysis and Design. 2013;72:1-12.

[138] Vogiatzis P, Chen S, Wang X, Li T, Wang L. Topology optimization of multi-material negative Poisson's ratio metamaterials using a reconciled level set method. Comput Aided Design. 2017;83:15-32.

[139] Vanek J, Galicia JAG, Benes B. Clever support: Efficient support structure generation for digital fabrication. Computer graphics forum: Wiley Online Library; 2014. p. 117-25.

[140] Hu K, Jin S, Wang CC. Support slimming for single material based additive manufacturing. Comput Aided Design. 2015;65:1-10.

[141] Zhang X, Le X, Panotopoulou A, Whiting E, Wang CC. Perceptual models of preference in 3D printing direction. ACM Transactions on Graphics (TOG). 2015;34(6):215.

[142] Hexcel. HexTow AS4 Carbon Fiber. www.hexcel.com.

[143] Papapetrou VS, Patel C, Tamijani AY. Stiffness-based optimization framework for the topology and fiber paths of continuous fiber composites. unpublished work. 2019.

[144] Markforged. Composites Material Datasheet. 2019.

[145] Liu K, Tovar A. An efficient 3D topology optimization code written in Matlab. Structural and Multidisciplinary Optimization. 2014;50(6):1175-96.

[146] Dehnavi MY, Khaleghian S, Emami A, Tehrani M, Soltani N. Utilizing digital image correlation to determine stress intensity factors. Polym Test. 2014;37:28-35.

[147] Khaleghian S, Emami A, Tehrani M, Soltani N. Analysis of effective parameters for stress intensity factors in the contact problem between an asymmetric wedge and a half-plane using an experimental method of photoelasticity. Mater Design. 2013;43:447-53.

[148] Blaber J, Adair B, Antoniou A. Ncorr: open-source 2D digital image correlation matlab software. Exp Mech. 2015;55(6):1105-22.

[149] Tamijani AY, Gharibi K, Kobayashi MH, Kolonay RM. Load paths visualization in plane elasticity using load function method. International Journal of Solids and Structures. 2018;135:99-109.

[150] Gharibi K, Tamijani A. Topology Optimization of Lattice Structures using Load Path and Homogenization. Computers and Structures2019.

[151] Bettini P, Alitta G, Sala G, Di Landro L. Fused deposition technique for continuous fiber reinforced thermoplastic. J Mater Eng Perform. 2017;26(2):843-8.

[152] Yang C, Tian X, Liu T, Cao Y, Li D. 3D printing for continuous fiber reinforced thermoplastic composites: mechanism and performance. Rapid Prototyping J. 2017;23(1):209-15.

[153] Frketic J, Dickens T, Ramakrishnan S. Automated manufacturing and processing of fiber-reinforced polymer (FRP) composites: An additive review of contemporary and modern techniques for advanced materials manufacturing. Additive Manufacturing. 2017;14:69-86.

[154] Yassin K, Hojjati M. Processing of thermoplastic matrix composites through automated fiber placement and tape laying methods: A review. J Thermoplast Compos. 2018;31(12):1676-725.

[155] Funk JG, Sykes Jr GF. The Effects of Simulated Space Environmental Parameters on Six Commercially Available Composite Materials. NATIONAL AERONAUTICS AND SPACE ADMINISTRATION HAMPTON VA LANGLEY RESEARCH …; 1989.

[156] Gao S-L, Kim J-K. Cooling rate influences in carbon fibre/PEEK composites. Part 1. Crystallinity and interface adhesion. Composites Part A: Applied science and manufacturing. 2000;31(6):517-30.

[157] Gao SL, Kim JK. Cooling rate influences in carbon fibre/PEEK composites. Part II: interlaminar fracture toughness. Compos Part a-Appl S. 2001;32(6):763-74.

[158] Gao SL, Kim JK. Effect of cooling rate on interphase properties of carbon fibre/PEEK composites. Mater Sci Res Int. 1999;5(3):157-62.

[159] Ostberg GMK, Seferis JC. Annealing Effects on the Crystallinity of Polyetheretherketone (Peek) and Its Carbon-Fiber Composite. J Appl Polym Sci. 1987;33(1):29-39.

[160] Buggy M, Carew A. The Effect of Thermal Aging on Carbon-Fiber-Reinforced Polyetheretherketone (Peek) .1. Static and Dynamic Flexural Properties. J Mater Sci. 1994;29(7):1925-9.

[161] Buggy M, Carew A. The Effect of Thermal Aging on Carbon-Fiber-Reinforced Polyetheretherketone (Peek) .2. Morphological-Changes. J Mater Sci. 1994;29(8):2255-9.

[162] Sarasua JR, Remiro PM, Pouyet J. Effects of thermal history on mechanical behavior of PEEK and its short-fiber composites. Polym Composite. 1996;17(3):468-77.

[163] Hachmi BD, VuKhanh T. Crystallization mechanism in PEEK/carbon fiber composites. J Thermoplast Compos. 1997;10(5):488-501.

[164] El Kadi H, Denault J. Effects of processing conditions on the mechanical behavior of carbon-fiber-reinforced PEEK. J Thermoplast Compos. 2001;14(1):34-53.

[165] Zhang ZY, Zeng HM. Nucleation and Crystal-Growth of Peek on Carbon-Fiber. J Appl Polym Sci. 1993;48(11):1987-95.

[166] Stokes-Griffin CM, Compston P. The effect of processing temperature and placement rate on the short beam strength of carbon fibre-PEEK manufactured using a laser tape placement process. Compos Part a-Appl S. 2015;78:274-83.

[167] Quan H, Li ZM, Yang MB, Huang R. On transcrystallinity in semi-crystalline polymer composites. Composites Science and Technology. 2005;65(7-8):999-1021.

[168] Zhang W, Wu AS, Sun J, Quan Z, Gu B, Sun B, et al. Characterization of residual stress and deformation in additively manufactured ABS polymer and composite specimens. Composites Science and Technology. 2017;150:102-10.

[169] Hart KR, Dunn RM, Sietins JM, Mock CMH, Mackay ME, Wetzel ED. Increased fracture toughness of additively manufactured amorphous thermoplastics via thermal annealing. Polymer. 2018;144:192-204.

[170] Ivey M, Melenka GW, Carey JP, Ayranci C. Characterizing short-fiber-reinforced composites produced using additive manufacturing. Advanced Manufacturing: Polymer & Composites Science. 2017;3(3):81-91.

[171] Mehdikhani M, Gorbatikh L, Verpoest I, Lomov SV. Voids in fiber-reinforced polymer composites: a review on their formation, characteristics, and effects on mechanical performance. Journal of Composite Materials. 2019;53(12):1579-669.

[172] Gao SL, Kim JK. Cooling rate influences in carbon fibre/PEEK composites. Part 1. Crystallinity and interface adhesion. Compos Part a-Appl S. 2000;31(6):517-30.

[173] Blundell D, Osborn B. The morphology of poly (aryl-ether-ether-ketone). Polymer. 1983;24(8):953-8.

[174] Wei C-L, Chen M, Yu F-E. Temperature modulated DSC and DSC studies on the origin of double melting peaks in poly (ether ether ketone). Polymer. 2003;44(26):8185-93.

[175] Lee Y, Porter RS, Lin J. On the double-melting behavior of poly (ether ether ketone). Macromolecules. 1989;22(4):1756-60.

[176] Jin L, Ball J, Bremner T, Sue H-J. Crystallization behavior and morphological characterization of poly (ether ether ketone). Polymer. 2014;55(20):5255-65.

[177] Lee Y, Porter RS. Crystallization of poly (etheretherketone)(PEEK) in carbon fiber composites. Polymer Engineering & Science. 1986;26(9):633-9.

[178] Blundell DJ, Chalmers JM, Mackenzie MW, Gaskin WF. Crystalline Morphology of the Matrix of Peek-Carbon Fiber Aromatic Polymer Composites .1. Assessment of Crystallinity. Sampe Quart. 1985;16(4):22-30.

[179] Blundell DJ, Osborn BN. Crystalline Morphology of the Matrix of Peek-Carbon Fiber Aromatic Polymer Composites .2. Crystallization Behavior. Sampe Quart. 1985;17(1):1-6.

[180] Thomason J, Van Rooyen A. Transcrystallized interphase in thermoplastic composites. J Mater Sci. 1992;27(4):897-907.

[181] Kim J-K, Mai Y-W. Engineered interfaces in fiber reinforced composites: Elsevier; 1998.

[182] Jäger J, Sause M, Burkert F, Moosburger-Will J, Greisel M, Horn S. Influence of plastic deformation on single-fiber push-out tests of carbon fiber reinforced epoxy resin. Composites Part A: Applied Science and Manufacturing. 2015;71:157-67.

[183] Greisel M, Jäger J, Moosburger-Will J, Sause M, Mueller W, Horn S. Influence of residual thermal stress in carbon fiber-reinforced thermoplastic composites on interfacial fracture toughness evaluated by cyclic single-fiber push-out tests. Composites Part A: Applied Science and Manufacturing. 2014;66:117-27.

[184] Moosburger-Will J, Greisel M, Schulz M, Löffler M, Mueller WM, Horn S. Investigation of the fiber-matrix interaction in carbon fiber-reinforced polyether ether ketone by cyclic single fiber push-out and push-back tests. Composite Interfaces. 2019:1-21.

[185] Niu Y-F, Yang Y, Gao S, Yao J-W. Mechanical mapping of the interphase in carbon fiber reinforced poly (ether-ether-ketone) composites using peak force atomic force microscopy: Interphase shrinkage under coupled ultraviolet and hydro-thermal exposure. Polym Test. 2016;55:257-60.

[186] Olley R, Bassett D, Blundell D. Permanganic etching of PEEK. Polymer. 1986;27(3):344-8.

[187] Blundell DJ, Crick RA, Fife B, Peacock J, Keller A, Waddon A. Spherulitic Morphology of the Matrix of Thermoplastic Peek Carbon-Fiber Aromatic Polymer Composites. J Mater Sci. 1989;24(6):2057-64.